HEAT RELEASE EFFECTS ON DECAYING HOMOGENEOUS COMPRESSIBLE TURBULENCE

A Dissertation

by

KURN CHUL LEE

Submitted to the Office of Graduate Studies of
Texas A&M University
in partial fulfillment of the requirements for the degree of

DOCTOR OF PHILOSOPHY

May 2008

Major Subject: Aerospace Engineering

HEAT RELEASE EFFECTS ON DECAYING HOMOGENEOUS COMPRESSIBLE TURBULENCE

A Dissertation

by

KURN CHUL LEE

Submitted to the Office of Graduate Studies of
Texas A&M University
in partial fulfillment of the requirements for the degree of

DOCTOR OF PHILOSOPHY

Approved by:

Chair of Committee,	Sharath S. Girimaji
Committee Members,	Rodney Bowersox
	N. K. Anand
	Prabir Daripa
Head of Department,	Helen Reed

May 2008

Major Subject: Aerospace Engineering

ABSTRACT

Heat Release Effects on Decaying Homogeneous
Compressible Turbulence. (May 2008)
Kurn Chul Lee, B.S., Seoul National University, Korea;
M.S., Seoul National University, Korea
Chair of Advisory Committee: Dr. Sharath S. Girimaji

High Mach-number compressible flows with heat release are inherently more complicated than incompressible flows due to, among other reasons, the activation of the thermal energy mode. Such flow fields can experience significant fluctuations in density, temperature, viscosity, conductivity and specific heat, which affect velocity and pressure fluctuations. Furthermore, the flow field cannot be assumed to be dilatation-free in high Mach numbers and even in low Mach-number flows involving combustion, or in boundary layers on heated walls. The main issue in these high-speed and highly-compressible flows is the effect of thermal gradients and fluctuations on turbulence. The thermal field has various routes through which it affects flow structures of compressible turbulence. First, it has direct influence through pressure, which affects turbulence via pressure-strain correlation. The indirect effects of thermal fields on compressible turbulence are through the changes in flow properties. The high temperature gradients alter the transport coefficient and compressibility of the flow. The objective of this work is to answer the following questions: How do temperature fluctuations change the compressible flow structure and energetics? How does compressibility in the flow affect the non-linear pressure redistribution process? What is the main effect of spatial transport-coefficient variation? We perform direct numerical simulations (DNS) to answer the above questions. The investigations are categorized into four parts: 1) Turbulent energy cascade and kinetic-internal energy interactions under the influence of temperature fluctuations; 2) Return-to-isotropy of anisotropic turbulence under the influence of large temperature fluctuations; 3) The effect of turbulent Mach number and dilatation level on small-scale (velocity-gradient) dynamics; 4) The effect of variable transport-coefficients (viscosity and diffusivity) on cascade and dissipation processes of turbulence. The findings lead to a better understanding of temperature fluctuation effects on non-linear processes in compressible turbulence. This improved understanding is expected to provide direction for improving second-order closure models of compressible turbulence.

To my wife Jungsoo, daughter Jieun, and son Hyunsung

ACKNOWLEDGMENTS

I would like to thank my advisor, Dr. Sharath S. Girimaji for his support and patience. He has been a role model, a leader as well as a teacher. He has inspired me with the physics of turbulence in a much broader way. I also thank my committee members, Dr. Prabir Daripa, Dr. N. K. Anand, and Dr. Rodney Bowersox. Their comments and advices have been essential for this dissertation.

I would also like to thank Dr. Dazhi Yu, Dr. Huidan Yu, and Dr. Johannes Kerimo for their kindness in introducing me to the lattice Boltzmann method and gas kinetic method. I also wish to thank my colleagues: Sawan Suman, Sunil Lakshmipathy, Sunny Jain, Tucker Lavin, Benjamin Riley, Gaurav Kumar, Sriram Arasanipalai, Dasia Reyes, Rebecca Bertsch, and Anand Mishra. I was able to enrich my understanding of engineering problems through encouraging discussions and tough debates with them. I have enjoyed my life in the Aerospace Engineering Department due to much help from faculty and staff, including Dr. Walter Haisler, Dr. Jacques Richard, Ms. Karen Knabe, and Ms. Colleen Leatherman.

All my work cannot stand without my parents' endless love and pray. Lastly, I want to celebrate this moment with my wife Jungsoo, my daugher Jieun, and my son Hyunsung. It wouldn't be possible to make this achievement without their love and patience.

TABLE OF CONTENTS

LIST OF TABLES

LIST OF FIGURES

FIGURE Page

FIGURE Page

CHAPTER I

INTRODUCTION

High-speed compressible flows with heat release are inherently more complicated than incompressible flows due to, among other reasons, the activation of the thermal energy mode. Such flow fields can experience significant fluctuations in density, temperature, viscosity, conductivity, and specific heat, in addition to velocity and pressure fluctuations [1, 2]. Furthermore, the flow field cannot be assumed to be dilatation-free (or solenoidal) at high Mach numbers and even in low Mach-number flows involving combustion, or in boundary layers on heated walls. Thus, compressible turbulence can be expected to have different flow characteristics and perhaps even different energy cascade mechanisms from incompressible turbulence.

A good understanding of high-enthalpy compressible turbulence is crucial for analyzing the flow around re-entry spacecrafts and hypersonic flight vehicles, and inside scramjet engines. One main factor affecting turbulence in these high-enthalpy flows is the presence of strong thermal gradients and fluctuations.

To assess how these factors affect turbulence, one must understand how the processes of energy production, redistribution, cascade and dissipation are modified by heat release. A typical turbulence energy spectrum is shown in Fig. 1. In any turbulent flow, either incompressible or compressible, turbulent energy is produced at the large scales by the action of mean velocity gradients (energy input) and is then redistributed by pressure effects among the various components as it cascades down to small scales due to nonlinear interactions (energy cascade). In the final stage of the turbulence life-cycle, energy is dissipated at the small scales by the action of

---

This dissertation follows the style of *AIAA Journal.*

molecular viscosity (energy dissipation) [3, 4].

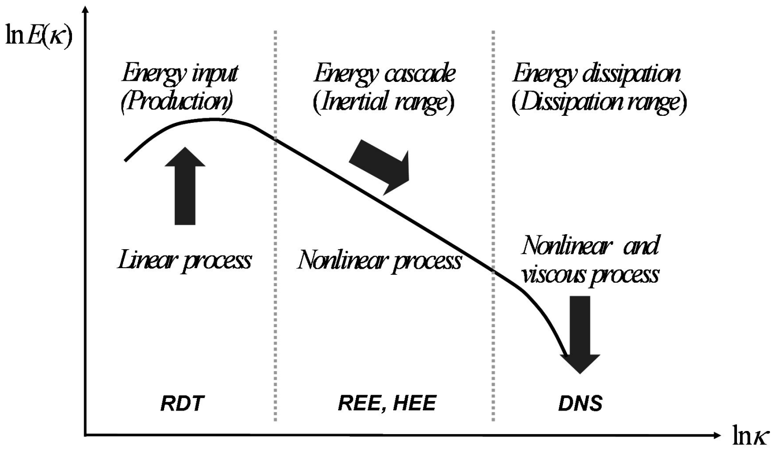

Fig. 1. Typical energy spectrum of turbulence and methodologies for studying turbulence

For a clear and comprehensive understanding of compressible turbulence, it is desirable to study the three key incumbent processes (linear, non-linear and dissipative) in isolation. The linear processes of production and rapid pressure-strain effects can be analyzed using the Rapid Distortion Theory (RDT) [5, 6, 7, 8]. Key non-linear cascade and velocity gradient dynamics can be studied using the Restricted Euler Equation (REE) in incompressible flows [9, 10, 11], and the Homogenized Euler Equation (HEE) in compressible flows [12]. Direct Numerical Simulations (DNS) are ideally suited for examining the non-linear (slow) pressure-strain effects, viscous processes and small-scale structure (Fig. 1).

The general goal of this dissertation is to examine the effects of large temperature fluctuations on non-linear turbulence processes and to investigate the small-scale structure of turbulence as a function of a turbulent Mach number.

The thermal field has various routes through which it affects compressible turbulence. First of all, it asserts direct influence through pressure: the pressure-strain correlation directly affects Reynolds stress. Also, the temperature field exerts indirect effects on compressible turbulence through the changes in transport properties. Fig. 2 depicts flow phenomena over a hypersonic vehicle. Flow experiences high temperature gradients as it passes through the shock and in the enthalpy region around the boundary layers. The high temperature gradients affect the transport coefficient (viscosity, conductivity, diffusivity) and compressibility of the flow. In hypersonic flows, the thermal effects are so severe that they can lead to a thermo-chemical non-equilibrium state in which higher quantum states of vibrational and rotational modes are energized [1]. In this dissertation, we restrict our study to large temperature fluctuations, without specifying the source of underlying heat release.

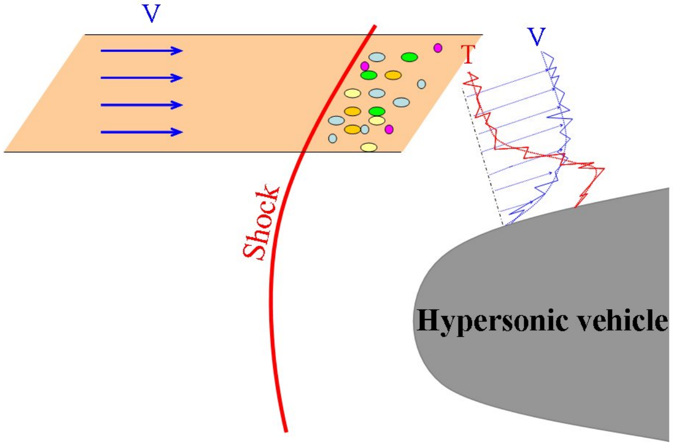

Fig. 2. Flow around hypersonic vehicle

One main difference between incompressible and compressible turbulence arises out of the presence of dilatational fluctuations in the latter. It is generally acknowledged that dilatational turbulence dynamics is distinct from solenoidal turbulence, due to the absence of vorticity in the former. Dilatational fluctuations are inherently wavelike, evolving on the acoustic time scale. Typically, in low Mach-number flows, dilatational fluctuations account for a negligible fraction of the total velocity field.

But in high Mach numbers or in low Mach number flows with heat release, dilatational fluctuations cannot be neglected. Kraichnan [13] argues that at very high Mach numbers, in the non-linear inviscid limit, there must be equipartition of energy between solenoidal and dilatational motions. Indeed, it is seen from compressible RDT that the linear interaction between the solenoidal field and high gradient Mach number shear can result in high levels (20% of the total) of dilatational fluctuations [14, 8]. Based on these considerations, we suggest that dilatational fluctuations are an important and integral part of turbulence in high Mach-number (especially hypersonic) flows. Dilatational fluctuations are expected to affect non-linear cascading, non-linear pressure-strain, and viscous processes. Hence, it is important to understand velocity gradient dynamics and small-scale structure as a function of the dilatation level in compressible turbulence.

A. Literature review

Many efforts have been made to understand compressible turbulence. Kida and Orszag [15, 16, 17] studied energy dynamics in decaying and forced compressible turbulence using DNS. They studied the compressibility effects using the ratio of solenoidal and dilatational components of compressible turbulence. They showed that the coupling between the two components of kinetic energy is weak and that most of the energy introduced to either component is transferred to internal energy without passing through the other component. They also showed that the compressible component of the energy spectrum depends strongly on Mach number. Sarkar *et al.* [18, 19] studied the dilatational term using asymptotic analysis of the compressible Navier-Stokes equation and found that there is an equipartition of compressible energy between potential and dilatational kinetic modes. They also performed DNS of decaying compressible turbulence and found support for their conclusions. Erlebacher and Sarkar [20] analyzed the strain-rate tensor using DNS results of compressible homogeneous shear turbulence, by decomposing the strain-rate tensor into solenoidal and dilatational parts. The structure of the solenoidal strain-rate tensor was found to be similar to that of incompressible turbulence. The dilatational strain-rate tensor was found to have a preferred structure in the regions of strong dilatation, and the alignment of the pressure-gradient vector was found to be strongly affected by compressibility. Crespo *et al.* [21] performed DNS of decaying anisotropic compressible turbulence from a variety of initial fields and found that axisymmetric turbulence with a positive third invariant returns to isotropy slower than the case with a negative third invariant. Pantano and Sarkar [22] performed DNS of turbulent shear flows and found that the gradient Mach number is the key quantity that determines the reduction in pressure-strain correlations in compressible shear flows. They explained that the finite speed of sound in compressible flows introduces a finite time delay in the transmission of pressure signals from one point to an adjacent point and the resultant decorrelation leads to a reduction in the pressure-strain correlation.

Compressible pressure-strain correlation, the main role of which is to redistribute kinetic energy among Reynolds stresses, has been the focus of a series of studies. Sarkar [23] studied the pressure dilatation correlation in homogeneous compressible flows and developed a model for pressure dilatation to account for the compressibility effect. Hamba [24] developed a model for pressure dilatation and pressure-strain terms for homogeneous shear flow. He used normalized pressure variance to consider the compressibility effect on the pressure strain. Adumitroaie *et al.* [25] derived the Favre-Reynolds stress equation and constructed models for unclosed terms: pressure-strain correlation, viscous acceleration, pressure acceleration, dissipation and turbulent transport. They incorporated the compressibility using the turbulent Mach number, mean density gradient, mean pressure gradient, mean dilatation, and mean velocity gradients. Park and Park [26] developed a compressible pressure-strain model using the concept of moving equilibrium in homogeneous shear flow. They also employed the non-dimensional pressure variance for the compressibility function. Marzougui *et al.* [27] extended the incompressible LRR model for the pressure strain correlation to compressible turbulent flow and confirmed that the gradient Mach number is an important parameter to understand compressibility in homogeneous shear flow.

The effects of heat release on compressible turbulence have been studied by Jaberi *et al.* [28]. They found that dilatational motions are affected more than solenoidal motions in the presence of heat release, and the pressure work tends to increase the turbulent kinetic energy. They also showed that the effect of heat release is to weaken the alignment of the vorticity vector with the intermediate eigenvector of the strain-rate tensor, due to the variation in molecular viscosity. Livescu *et al.* [29] studied non-premixed reacting compressible homogeneous turbulent shear flow and showed that heat release has a damping effect on turbulent kinetic energy for the flow with variable transport coefficients. They also found that dilatational kinetic energy production increases during the time when the reaction is important. They also confirmed that the pressure dilatation correlation typically transfers energy from the internal to the kinetic modes. A great deal of research still needs to be done in turbulent flows with heat release to arrive at the level of understanding we have in incompressible turbulence. Especially, non-linear cascading and dissipation processes are very poorly understood in compressible turbulence with large temperature fluctuations.

B. Scope of the dissertation

In this dissertation, we perform four investigations to improve our understanding of high-speed compressible turbulence. DNS of isotropic and anisotropic compressible turbulence are conducted toward this end. Selected features of high-speed compressible turbulence are investigated with different computational setups. The topics studied are:

1) Turbulent energy cascade and kinetic-internal energy interactions under the influence of temperature fluctuations;

2) Return-to-isotropy of anisotropic turbulence under the influence of large temperature fluctuations;

3) The effect of turbulent Mach number and dilatation level on small-scale (velocity-gradient) dynamics;

4) The effect of variable transport-coefficients (viscosity and diffusivity) on cascade and dissipation processes of turbulence.

The main findings are:

1) Chapter IV: In general, pressure dilatation transfers energy back and forth between kinetic and thermal modes. However, on the average, pressure dilatation transfers energy from the thermal to kinetic mode during heat release or in the presence of temperature fluctuations. The temporal velocity gradient is enhanced due to the generation of a rapidly evolving dilatational velocity field in the presence of temperature fluctuations. The alignments among vorticity vector and the gradients of thermodynamic variables are altered by temperature fluctuations. The pressure gradient especially tends to be uncorrelated with the vorticity vector as well as with the density and temperature gradients in the presence of temperature fluctuations.

2) Chapter V: The temperature fluctuations do not change the solenoidal field

return-to-isotropy. It is observed that the solenoidal fluctuations interact very little with the dilatational fluctuations up to a turbulent Mach number of 0.6. Dilatational energy conversion by pressure dilatation is proportional to the mean square of the initial temperature fluctuations. Equipartition between fluctuating internal energy and dilatational kinetic energy is observed in all numerical experiments at equilibrium state. The dilatational kinetic energy is found to scale with the initial mean square pressure fluctuations.

3) Chapter VI: As turbulent Mach number increases, the mean flow statistics differ only slightly from that of incompressible turbulence. However, the level of dilatational fluctuations increases and in the regions of non-zero dilatation, the structure and dynamics of turbulence are profoundly altered. The degree of modification (from incompressible turbulence) depends on the level of dilatation (Ph.D. dissertation of S. Suman, in progress). Thus, for characterization of compressible turbulence, one must consider turbulence statistics as a function of dilatation level, rather than turbulent Mach number.

4) Chapter VII: In this study, we examine - in the presence of strong viscosity gradients - the validity of Taylor's (1935) postulate that turbulent dissipation is determined exclusively by large scale flow parameters and is independent of viscosity. It is indeed found that mechanical and scalar dissipations are completely impervious to the spatial and temporal variations in transport properties. This has important consequences for closure modeling of dissipation in high enthalpy flows.

C. Dissertation outline

Chapter II describes the Favre-averaged second-moment transport equation, energy equation, enstrophy and dilatation transport equations, and the role of viscosity and

Reynolds stress. The numerical methods, such as lattice Boltzmann method (LBM) and gas kinetic method (GKM), are presented in Chapter III. Four relevant investigations of heat release effects are discussed in Chapter IV through Chapter VII and we summarized our study in Chapter VIII.

CHAPTER II

SECOND-MOMENT TRANSPORT EQUATION

We start with compressible Navier-Stokes equations given by

$$\frac{D\rho}{Dt} = -\rho\frac{\partial u_j}{\partial x_j}\,, \tag{2.1}$$

$$\rho\frac{Du_i}{Dt} = -\frac{\partial p}{\partial x_i} + \frac{\partial \tau_{ij}}{\partial x_j}\,, \tag{2.2}$$

$$\rho\frac{De}{Dt} = -\frac{\partial q_j}{\partial x_j} - p\frac{\partial u_j}{\partial x_j} + \tau_{ij}\frac{\partial u_j}{\partial x_i}\,, \tag{2.3}$$

where $\frac{D}{Dt} = \frac{\partial}{\partial t} + u_j\frac{\partial}{\partial x_j}$; ρ is the density of given fluid; p is instantaneous pressure; u_i is instantaneous velocity; q_j is heat flux; e is the internal energy per unit mass; κ is thermal conductivity; and τ_{ij} is the viscous stress tensor defined as

$$\tau_{ij}(u) = 2\mu S_{ij} + \left(\mu_B - \frac{2}{3}\mu\right) S_{kk}\delta_{ij}\,. \tag{2.4}$$

Here, μ is dynamic shear viscosity; μ_B is dynamic bulk viscosity; δ_{ij} is the Kronecker delta; S_{ij} is the strain rate tensor defined as

$$S_{ij}(u) = \frac{1}{2}\left(\frac{\partial u_i}{\partial x_j} + \frac{\partial u_j}{\partial x_i}\right)\;; \tag{2.5}$$

and S_{kk} is the dilatation (velocity divergence), which appears in compressible flows. Two more equations are needed to close the above compressible Navier-Stokes equations (2.1)-(2.3): thermal and caloric equations of state. In this study, for the thermal equation of state, we use the ideal gas law $p = \rho RT$, where R is the gas constant and T is the temperature. For the caloric equation of state, we use $e = c_v T$, where c_v is the specific heat at constant volume (caloric equation of state for an ideal gas).

With an interest in the fluctuating velocity field, *i.e.* turbulence, we introduce the Favre decomposition for flow quantities:

$$g = \tilde{g} + g'' \,, \tag{2.6}$$

where

$$\tilde{g} = \frac{\overline{\rho g}}{\bar{\rho}} \,, \tag{2.7}$$

$$\widetilde{g''} = \frac{\overline{\rho g''}}{\bar{\rho}} = 0 \,, \tag{2.8}$$

and Reynolds decomposition:

$$g = \bar{g} + g' \,, \tag{2.9}$$

where

$$\overline{g'} = 0 \,. \tag{2.10}$$

Ensemble averages (Reynolds average) and density weighted average (Favre average) are described with bar and tilde respectively, and prime and double prime denotes the fluctuation from Reynolds average and Favre average respectively.

We use Favre decomposition for the instantaneous velocity and internal energy field, and Reynolds decomposition for the other flow variables such that

$$u_i = \tilde{u_i} + u_i'' \,, \tag{2.11}$$

$$\tau_{ij} = \tau_{ij}(\tilde{u}) + \tau_{ij}(u'') \,, \tag{2.12}$$

$$e = \tilde{e} + e'' \,, \tag{2.13}$$

$$p = \bar{p} + p' \,, \tag{2.14}$$

$$\rho = \bar{\rho} + \rho' \,, \tag{2.15}$$

$$q_i = \overline{q_i} + q_i' \,. \tag{2.16}$$

Here, the fluctuations of shear and bulk viscosities are considered unimportant and the viscosity fluctuations and their correlations with other flow quantities are neglected. By using the above decompositions in the compressible Navier-Stokes equations (2.1), (2.2), and (2.3) and ensemble-averaging the resulting equations, we obtain the Favre-averaged Navier-Stokes equation (FANS):

$$\begin{aligned}
\frac{\partial \bar{\rho}}{\partial t} + \frac{\partial \bar{\rho}\tilde{u}_j}{\partial x_j} &= 0\,, && (2.17)\\
\frac{\partial \bar{\rho}\tilde{u}_i}{\partial t} + \frac{\partial \bar{\rho}\tilde{u}_i\tilde{u}_j}{\partial x_j} &= -\frac{\partial \bar{\rho}\widetilde{u_i''u_j''}}{\partial x_j} - \frac{\partial \bar{p}}{\partial x_i} + \frac{\partial \bar{\tau}_{ij}}{\partial x_j}\,, && (2.18)\\
\frac{\partial \bar{\rho}\tilde{e}}{\partial t} + \frac{\partial \bar{\rho}\tilde{u}_j\tilde{e}}{\partial x_j} &= -\frac{\partial \bar{\rho}\widetilde{u_j''e''}}{\partial x_j} - \frac{\partial \bar{q}_j}{\partial x_j} - \overline{p\frac{\partial u_j}{\partial x_j}} + \overline{\tau_{ij}\frac{\partial u_j}{\partial x_i}}\,. && (2.19)
\end{aligned}$$

For most engineering simulations of compressible flows, the above equations are used, in which there are important unclosed terms. In Eq.(2.18) and (2.19), $\widetilde{u_i''u_j''}$ and $\widetilde{u_j''e''}$ are called Favre-averaged Reynolds stress and turbulent heat flux respectively. In this study, we are interested in the physics of the Favre-averaged Reynolds stress. How does the Reynolds stress behave in compressible flow? We study the evolution equation of the Reynolds stress to investigate the crucial turbulence processes of pressure-strain redistribution and dissipation.

A. Favre-Reynolds stress equation

The Favre-Reynolds stress transport equation can be written as [25]:

$$\frac{\partial(\bar{\rho}\widetilde{u_i''u_j''})}{\partial t} = T_{ij} + P_{ij} + R_{ij} - \varepsilon_{ij}\,, \tag{2.20}$$

where

$$\begin{aligned}
T_{ij} &= -\frac{\partial}{\partial x_k}\Big[\bar{\rho}\widetilde{u_i''u_j''}\tilde{u}_k + \bar{\rho}\widetilde{u_i''u_j''u_k''} + \overline{u_i''p}\delta_{jk} + \overline{u_j''p}\delta_{ik}\\
&\qquad - \overline{u_i''\tau_{jk}(u)} - \overline{u_j''\tau_{ik}(u)}\Big]\,, && (2.21)
\end{aligned}$$

$$\begin{aligned} P_{ij} &= -\bar{\rho}\widetilde{u_i''u_k''}\frac{\partial \tilde{u}_j}{\partial x_k} - \bar{\rho}\widetilde{u_j''u_k''}\frac{\partial \tilde{u}_i}{\partial x_k}\,, && (2.22) \\ R_{ij} &= \overline{p\left(\frac{\partial u_i''}{\partial x_j} + \frac{\partial u_j''}{\partial x_i}\right)}\,, && (2.23) \\ \varepsilon_{ij} &= \overline{\tau_{jk}(u)\frac{\partial u_i''}{\partial x_k}} + \overline{\tau_{ik}(u)\frac{\partial u_j''}{\partial x_k}}\,. && (2.24) \end{aligned}$$

In (2.20)-(2.24), T_{ij} is the turbulent transport term which will disappear in homogeneous flows, and P_{ij} is the turbulence production term which is responsible for turbulent energy production given mean velocity gradient $\frac{\partial \tilde{u}_i}{\partial x_j}$. The pressure-strain correlation tensor, R_{ij}, is responsible for energy redistribution among Reynolds stress components and its trace enables reversible energy exchange between kinetic and internal modes. The dissipation tensor, ε_{ij}, irreversibly transfers energy from kinetic to internal modes. This work focuses on the physics of energy redistribution and dissipation processes in compressible flows with substantial heat release.

In decaying homogeneous flows, the Reynolds stress transport equation (2.20) can be simplified as

$$\frac{\partial(\bar{\rho}\widetilde{u_i''u_j''})}{\partial t} = 2\langle ps_{ij}\rangle - 2\langle\varepsilon_{ij}\rangle, \tag{2.25}$$

where

$$\begin{aligned} 2\langle ps_{ij}\rangle &= \overline{p'\left(\frac{\partial u_i''}{\partial x_j} + \frac{\partial u_j''}{\partial x_i}\right)}\,, \\ 2\langle\varepsilon_{ij}\rangle &= \overline{\tau_{jk}(u'')\frac{\partial u_i''}{\partial x_k}} + \overline{\tau_{ik}(u'')\frac{\partial u_j''}{\partial x_k}}\,. \end{aligned}$$

The first term on the right-hand side is the pressure-strain correlation tensor and the second term is the dissipation tensor. Here, s_{ij} is the strain rate tensor of fluctuating velocity field defined as

$$s_{ij} = \frac{1}{2}\left(\frac{\partial u_i''}{\partial x_j} + \frac{\partial u_j''}{\partial x_i}\right)\,. \tag{2.26}$$

B. Energy equations

In decaying homogeneous flows, the turbulent kinetic energy evolution equation can be obtained by contracting the indexes of Eq.(2.25):

$$\frac{\partial}{\partial t}(k) = \langle pd \rangle - \varepsilon \,, \tag{2.27}$$

where

$$\begin{aligned} k &= \frac{1}{2}\widetilde{u_i''u_i''}\,, \\ \langle pd \rangle &= \langle p s_{ii} \rangle\,, \\ \varepsilon &= \langle \varepsilon_{ii} \rangle\,. \end{aligned}$$

In the above equation, k, $\langle pd \rangle$ and ε denote turbulent kinetic energy, pressure dilatation and dissipation rate respectively. The corresponding thermal energy equation is given by

$$\frac{\partial}{\partial t}(e) = -\langle pd \rangle + \varepsilon \,. \tag{2.28}$$

Pressure dilatation can have either a positive or negative value indicating reversible energy transfer, while dissipation irreversibly transfers energy from kinetic to thermal modes. From Eqs.(2.27) and (2.28), we can confirm that total energy is conserved in decaying homogeneous turbulence [30].

In Eq.(2.27), the kinetic energy dissipation rate, ε, is given by

$$\begin{aligned} \varepsilon &= \overline{\tau_{ij}(u'')\frac{\partial u_i''}{\partial x_j}} && (2.29) \\ &= 2\mu\overline{s_{ij}s_{ij}} + \left(\mu_B - \frac{2}{3}\mu\right)\overline{s_{kk}^2} && (2.30) \end{aligned}$$

The second term on the right hand side of Eq.(2.30) represents the additional contribution to the dissipation rate in compressible flows. In compressible flows, the term $2\mu\overline{s_{ij}s_{ij}}$ also includes dilatational contribution. To identify the solenoidal and dilatational portions of dissipation for general compressible flow, we decompose the dissipation rate. The strain rate magnitude $s_{ij}s_{ij}$ in Eq.(2.30) can be decomposed as

$$s_{ij}s_{ij} = \omega_{ij}\omega_{ij} + \frac{\partial u_i''}{\partial x_j}\frac{\partial u_j''}{\partial x_i} \, , \tag{2.31}$$

and

$$\frac{\partial u_i''}{\partial x_j}\frac{\partial u_j''}{\partial x_i} = \frac{\partial^2}{\partial x_i \partial x_j}\left(u_i''u_j''\right) - 2\frac{\partial}{\partial x_j}\left(u_j''\frac{\partial u_i''}{\partial x_i}\right) + \frac{\partial u_i''}{\partial x_i}\frac{\partial u_j''}{\partial x_j} \, , \tag{2.32}$$

where ω_{ij} is the rotation rate tensor defined as

$$\omega_{ij} = \frac{1}{2}\left(\frac{\partial u_i''}{\partial x_j} - \frac{\partial u_j''}{\partial x_i}\right) \, . \tag{2.33}$$

Then, we obtain

$$s_{ij}s_{ij} = \omega_{ij}\omega_{ij} + \frac{\partial^2}{\partial x_i \partial x_j}\left(u_i''u_j''\right) - 2\frac{\partial}{\partial x_j}\left(u_j''\frac{\partial u_i''}{\partial x_i}\right) + \frac{\partial u_i''}{\partial x_i}\frac{\partial u_j''}{\partial x_j} \, , \tag{2.34}$$

The first term on the right hand side of Eq.(2.34) represents the vortical motion of turbulence; the second and third terms represent the inhomogeneous contributions to the strain rate; and the last term represents the dilatational motion of turbulence. Thus, strain rate magnitude, $s_{ij}s_{ij}$, consists of the rotation, inhomogeneous, and dilatation terms. In homogeneous flows, the inhomogeneous terms vanish and only the rotation and dilatation terms remain. Thus, the kinetic energy dissipation rate reduces to

$$\varepsilon = \varepsilon_s + \varepsilon_c \tag{2.35}$$

where

$$\varepsilon_s = 2\mu\overline{\omega_{ij}\omega_{ij}} \, , \tag{2.36}$$

$$\varepsilon_c = \left(\mu_B + \frac{4}{3}\mu\right)\overline{s_{kk}^2} \, , \tag{2.37}$$

in homogeneous flows. ε_s is the solenoidal dissipation corresponding to the incompressible portion of dissipation and ε_c is the dilatational dissipation corresponding to the compressible portion of dissipation. The transport equations for these two quantities are described in the following section.

C. Enstrophy and dilatation transport equations

Both the dilatation field and the enstrophy field are generated in compressible flows. The manner in which these fields are generated and transported is an important issue in the study of compressible turbulence. First, we start with the vorticity transport equation, which is useful in understanding the mechanism of vorticity generation in compressible flows. The vorticity transport equation is derived by taking a curl of the compressible Navier-Stokes equation (2.2):

$$\frac{D\Omega_i}{Dt} = S_{ik}\Omega_k - \Omega_i S_{kk} + \epsilon_{ijk}\frac{1}{\rho^2}\frac{\partial \rho}{\partial x_j}\frac{\partial p}{\partial x_k} + \epsilon_{ijk}\frac{\partial}{\partial x_j}\left(\frac{1}{\rho}\frac{\partial \tau_{km}}{\partial x_m}\right) , \qquad (2.38)$$

where Ω_i is the vorticity vector defined as

$$\Omega_i = \frac{\partial u_j}{\partial x_k} - \frac{\partial u_k}{\partial x_j} . \qquad (2.39)$$

Thus, one can see that vorticity is generated through four processes: vorticity stretching by strain S_{ik}, vorticity generation by dilatation S_{kk}, baroclinic generation through the interaction of pressure and density gradients, and viscous generation/destruction by the viscous term [31]. The baroclinic term $\epsilon_{ijk}\frac{1}{\rho^2}\frac{\partial \rho}{\partial x_j}\frac{\partial p}{\partial x_k}$ accounts for the change in vorticity due to the interaction between gradients of density and temperature. The baroclinic term generates a strong vorticity field when the density gradient tends to be perpendicular to the temperature gradient. When the density gradient is parallel to the temperature gradient, vorticity is not generated by the baroclinic term. For example, when there is a temperature field and no flow, the flow field will be driven purely by the temperature field. The density gradient will then be aligned well with pressure and temperature gradients. Thus, vorticity is not generated by the baroclinic term. In other extreme cases, such as high turbulent Mach number flows, the flow field has its own pressure and density distribution. Thus, the flow field may generate a significant amount of vorticity through the baroclinic term when we impose an arbitrary temperature field.

The enstrophy transport equation can be obtained by multiplying Ω_i in Eq.(2.38):

$$\begin{aligned} \frac{D}{Dt}\left(\frac{1}{2}\Omega_i\Omega_i\right) &= \Omega_i\Omega_k S_{ik} - \Omega_i\Omega_i S_{kk} + \epsilon_{ijk}\frac{1}{\rho^2}\Omega_i\frac{\partial \rho}{\partial x_j}\frac{\partial p}{\partial x_k} \\ &+ \epsilon_{ijk}\frac{\partial}{\partial x_j}\left(\Omega_i\frac{1}{\rho}\frac{\partial \tau_{km}}{\partial x_m}\right) - \epsilon_{ijk}\frac{1}{\rho}\frac{\partial \Omega_i}{\partial x_j}\frac{\partial \tau_{km}}{\partial x_m}\,. \end{aligned} \tag{2.40}$$

Similar to the vorticity generation mechanism, the enstrophy is influenced by strain-rate S_{ik}, dilatation S_{kk}, interaction of pressure and density gradients, and the viscous term.

Dilatation contributes to the kinetic energy dissipation rate in compressible flows. The transport equation of dilatation is derived directly by taking divergence of the compressible Navier-Stokes equation (2.2):

$$\frac{D}{Dt}S_{kk} = -\frac{\partial u_i}{\partial x_j}\frac{\partial u_j}{\partial x_i} - \frac{1}{\rho}\frac{\partial^2 p}{\partial x_k \partial x_k} + \frac{1}{\rho^2}\frac{\partial \rho}{\partial x_k}\frac{\partial p}{\partial x_k} + \frac{\partial}{\partial x_k}\left(\frac{1}{\rho}\frac{\partial \tau_{kj}}{\partial x_j}\right)\,. \tag{2.41}$$

Using the relation (2.32), we obtain

$$\begin{aligned} \frac{D}{Dt}S_{kk} &= -S_{kk}^2 - \frac{\partial^2}{\partial x_i \partial x_j}(u_i u_j) + 2\frac{\partial}{\partial x_j}\left(u_j\frac{\partial u_i}{\partial x_i}\right) \\ &+ \frac{1}{\rho^2}\frac{\partial \rho}{\partial x_k}\frac{\partial p}{\partial x_k} - \frac{1}{\rho}\frac{\partial^2 p}{\partial x_k \partial x_k} + \frac{\partial}{\partial x_k}\left(\frac{1}{\rho}\frac{\partial \tau_{kj}}{\partial x_j}\right)\,. \end{aligned} \tag{2.42}$$

Andreopoulos *et al.* [31] argue that the enstrophy is a source for dilatational motion: dilatation is caused by the straining motion ($S_{ij}S_{ij}$) as well as the rotational energy of the spinning motion ($\Omega_k\Omega_k$) since $\frac{\partial u_i}{\partial x_j}\frac{\partial u_j}{\partial x_i} = S_{ij}S_{ij} - \frac{1}{4}\Omega_k\Omega_k$. However, as seen in Eq.(2.32), the straining motion cancels out rotational motion and the inhomogeneous and dilatation terms remain as seen in Eq.(2.42) (first three terms on the right hand side). Thus, rotational motion is not a source for producing dilatational motion. Rather, pressure and density gradients are expected to generate the dilatational motion as in the fourth term on the right hand side of Eq.(2.42). Whenever the pressure gradient is aligned well with the density gradient, one can expect highly dilatational motion in the flows, *i.e.* highly compressible flow. It can be inferred from Eq.(2.40) that the dilatation acts as a medium in enstrophy generation, which corresponds to solenoidal dissipation. The dilatation also has a direct influence in dilatational dissipation in compressible flows (Eq.(2.42)).

D. Molecular viscosity

In compressible flows, the constitutive equation for stress tensor involves bulk viscosity as well as shear viscosity. To identify the physical significance of bulk viscosity, we introduce the concepts of mechanical pressure and thermodynamic pressure. The mechanical pressure $\bar{p}$ is defined as an average of the total normal stress on three mutually perpendicular surfaces:

$$\bar{p} = -\frac{1}{3}\sigma_{ii}\,, \tag{2.43}$$

where

$$\sigma_{ij} = -p\delta_{ij} + \tau_{ij}\,. \tag{2.44}$$

Here, σ_{ij} is the stress tensor representing the effects of all surface forces; p is the thermodynamic pressure (or equilibrium pressure); and τ_{ij} is the viscous stress tensor defined in Eq.(2.4).

Kinetic theory describes mechanical pressure as a measure of the molecular translational kinetic energy of a fluid particle (molecule), whereas thermodynamic pressure is a measure of the total molecular kinetic energy of a fluid particle. Thermodynamic pressure depends on two state variables, *i.e.* $p = p(\rho, e)$, in which the internal energy e involves all modes of molecular energy of a given fluid particle: translational, rotational, and vibrational. Using equations (2.43), (2.44), and (2.4), one finds that the difference between the thermodynamic pressure and the mechanical pressure is proportional to the divergence of the velocity vector as follows:

$$p - \bar{p} = \frac{1}{3}\tau_{ii} = \mu_B \frac{\partial u_i}{\partial x_i}\,. \tag{2.45}$$

The proportionality factor μ_B is referred to as bulk viscosity. Different modes of molecular energy have different relaxation times, so energy may be transferred from one mode to another. Bulk viscosity is a measure of this transfer of energy from the translational mode to the rotational and vibrational modes [32].

For monatomic gas, the only mode of molecular energy is the translational mode, so the mechanical and thermodynamic pressure are the same. Thus, the bulk viscosity is zero. For polyatomic gases and for liquids, the departure from $\mu_B = 0$ is frequently small and the bulk viscosity is considered to be zero. However, for a flow through a strong shock, the vibrational modes of energy are excited at the expense of the translational modes, so the bulk viscosity is non-trivial. In case the bulk viscosity plays an important role (*i.e.* thermodynamic nonequilibrium state), one cannot use the ideal-gas state equations $p = \rho RT$ and $e = c_v T$, which are used in thermodynamic equilibrium flow simulations. These equations do not account for the relaxation effects associated with the redistribution of molecular energy among translational, rotational, and vibrational modes of a fluid particle. Bulk viscosity is expected to be significant when the relaxation phenomenon becomes observable [33].

E. Reynolds stress vs. viscous stress

To enhance our understanding of turbulence, the role of Reynolds stress is compared to that of viscous stress in Fig. 3. κ is the wave number of the motion, which is the inverse of the length scale, and $E(\kappa)$ is the energy level at the wave number. L is the characteristic length scale for a flow of interest, η is the small dissipation scale of flow ($i.e.$ Kolmogorov scale), and λ is the scale of molecular motion ($i.e.$ molecular mean free path). To directly solve the Navier-Stokes equation (NS), a constitutive equation is needed for the viscous stress tensor, whereas a description of Reynolds stress is required to solve Reynolds (or Favre) Averaged Navier-Stokes equation (RANS or FANS). In principle, one can also trace all the molecules in molecular dynamics simulations (MD) to obtain the viscous stress tensor. However, such a computation is practically impossible for engineering problems due to the heavy computational load.

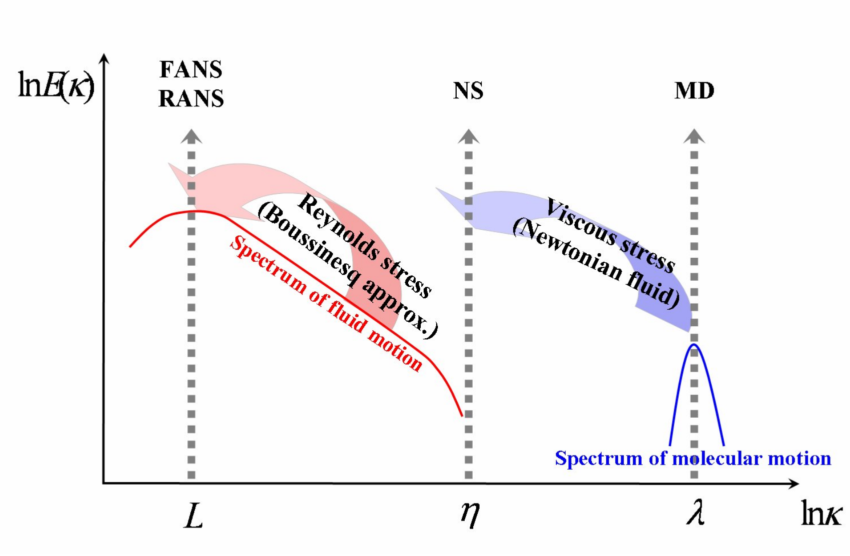

Fig. 3. Typical energy spectrum of fluid motion and molecular motion (RANS: Reynolds Averaged Navier Stokes equation; FANS: Favre Averaged Navier Stokes equation; NS: Navier Stokes equation; and MD: Molecular Dynamics)

Clearly, most of the energy of molecular motion is distributed in the scale of molecular motion λ which is much smaller than L. Due to the large disparity in molecular and continuum scales of interest, the action of molecular motion can be described with simple viscous stress. In Newtonian fluid, the viscous stress tensor is given by equations (2.44) and (2.4). In averaged Navier-Stokes equation, a similar closure can be used for Reynolds stress. Indeed, the popular Boussinesq approximation is similar to Eq.(2.4). This closure is expected to account for the effects of a wide spectrum of turbulent fluctuations. The overall effectiveness of the Boussinesq Reynolds stress closure is inferior to that of molecular viscous stress due to the proximity of scale L and turbulent fluctuations. Therefore, a more complete understanding of the action of turbulent fluctuations is needed.

CHAPTER III

COMPUTATIONAL METHOD

Direct numerical simulations are used to investigate the energy redistribution, dissipation processes and small scale structure of compressible turbulence. Although the investigation is performed in the context of Navier-Stokes equation and continuum flow description, we use a computational method based on the kinetic Boltzmann equation.

A. Kinetic Boltzmann equation with BGK collision operator

In mesoscopic description, flow variables are expressed using a single particle (molecule) velocity distribution function. The velocity distribution function can be obtained by solving the Boltzmann equation with BGK (Bhatnagar-Gross-Krook) collision model [34, 35, 36]:

$$\left(\partial_t + \vec{u} \cdot \nabla\right) f = \frac{1}{\tau}(g - f) \tag{3.1}$$

where $f \equiv f(\vec{x}, \vec{u}, t)$ is the single particle velocity distribution function; $\vec{u}$ is the microscopic particle velocity (in this chapter instantaneous flow velocity is not described by $\vec{u}$ but by $\vec{U}$); τ is the relaxation time due to particle collision; and g is the Maxwellian distribution function in an equilibrium state:

$$g = \frac{\rho}{(2\pi RT)^{D/2}}\, exp\left(-\frac{(\vec{u} - \vec{U})^2}{2RT}\right) , \tag{3.2}$$

where R is the gas constant; D is the dimension of the space; and ρ, $\vec{U}$, and T are the macroscopic density, velocity, and temperature, respectively. The macroscopic flow variables, ρ, $\vec{U}$, and T are calculated from the moments of distribution function f:

$$\rho \;\; = \;\; \int f d\vec{u}\,, \tag{3.3}$$

$$\begin{aligned} \rho\vec{U} &= \int \vec{u} f d\vec{u}\,, && (3.4)\\ \rho e &= \frac{1}{2}\int (\vec{u}-\vec{U})^2 f d\vec{u}\,. && (3.5) \end{aligned}$$

where the energy e can be written in terms of temperature T:

$$e = \frac{D_0}{2} RT\,, \tag{3.6}$$

In the above equation, D_0 is the number of degrees of freedom of a fluid particle motion.

B. Numerical schemes

Lattice Boltzmann method (LBM) and gas kinetic method (GKM) are used to solve the Boltzmann BGK equation (3.1). LBM is the finite difference scheme and applicable only to weakly compressible flows, whereas GKM is the finite volume scheme and applicable to fully compressible flows.

1. Lattice Boltzmann method (LBM)

In LBM, the solution f is obtained in a finite discrete velocity space. One well-known discrete velocity space in three dimensions is the 19-velocity model shown in Fig. 4. The incremental change in f is given by [36]

$$f_\alpha(\vec{x}_i + \vec{e}_\alpha \delta t, t+\delta t) - f_\alpha(\vec{x}_i, t) = -\frac{1}{\tau_n}\left(f_\alpha(\vec{x}_i,t) - g_\alpha(\vec{x}_i,t)\right)\,, \tag{3.7}$$

where $\tau_n \equiv \tau/\delta t$ is the dimensionless relaxation time in the unit of δt, and the equilibrium distribution function has the following form in discrete velocity space, using low Mach number approximation:

$$g_\alpha = \rho w_\alpha \left[1 + 3\frac{\vec{e}_\alpha\cdot\vec{U}}{c^2} + \frac{9}{2}\frac{(\vec{e}_\alpha\cdot\vec{U})^2}{c^4} - \frac{3}{2}\frac{\vec{U}\cdot\vec{U}}{c^2}\right]\,. \tag{3.8}$$

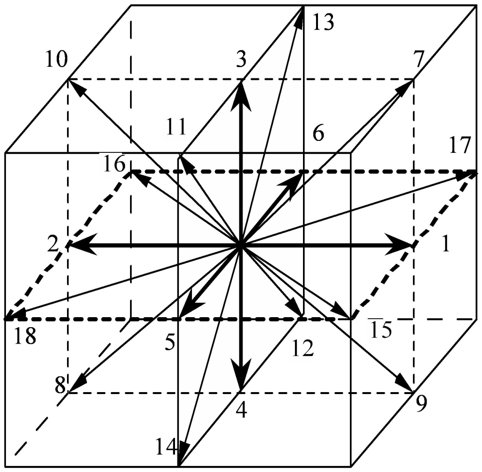

Fig. 4. Three-dimensional 19 discrete velocity (3D19Q) lattice

Here, c is defined as $c = \delta x/\delta t = \sqrt{3RT}$, and w_α and e_α are given by

$$w_\alpha = \begin{cases} \frac{1}{3}\,; & \alpha = 0\,, \\ \frac{1}{18}\,; & \alpha = 1, 2, \cdots, 6\,, \\ \frac{1}{36}\,; & \alpha = 7, 8, \cdots, 18\,. \end{cases}$$

$$\vec{e}_\alpha = \begin{cases} (0,0,0)\,; & \alpha = 0\,, \\ (\pm 1, 0, 0)c, (0, \pm 1, 0)c, (0, 0, \pm 1)c\,; & \alpha = 1, 2, \cdots, 6\,, \\ (\pm 1, \pm 1, 0)c, (0, \pm 1, \pm 1)c, (\pm 1, 0, \pm 1)c\,; & \alpha = 7, 8, \cdots, 18\,. \end{cases}$$

Invoking the Chapman-Enskog expansion [34], the Navier-Stokes equation can be recovered from the discrete equation and the shear viscosity is obtained as

$$\nu = \frac{\tau_n - 0.5}{3} c_s^2 \delta t\,. \tag{3.9}$$

The equation of state is given by

$$p = \rho c_s^2 = \frac{\rho}{3}\,, \tag{3.10}$$

where $c_s = \sqrt{RT}$ is the sound speed of isothermal fluid. The macroscopic flow variables, ρ and $\vec{U}$, are obtained as

$$\rho = \sum_\alpha f_\alpha \,, \tag{3.11}$$

$$\rho\vec{U} = \sum_\alpha \vec{e}_\alpha f_\alpha \,. \tag{3.12}$$

Details of LBM can be found in [36, 37, 38].

Even though LBM offers a variety of advantages for simulating fluid motion, it is valid only for isothermal flows. To accommodate the non-isothermal flow, a hybrid thermal lattice Boltzmann method (HTLBM) [39] is employed. HTLBM explicitly solves the macroscopic energy equation for temperature and LBM for mass and momentum, so that one can incorporate temperature variation in the flow. However, this method is limited to weakly compressible flows due to the inherent nature of LBM. Multi-relaxation time lattice Boltzmann method can also be adopted to increase stability and accuracy of LBM schemes [40]. Details of HTLBM can be found in [39, 40].

2. Gas kinetic method (GKM)

For general compressible flows, GKM approach is used to solve Eq.(3.1). Xu [41, 42] developed and verified GKM for various high Mach-number flows and shock problems, and Kerimo and Girimaji [43] demonstrate GKM possesses the required degree of accuracy and robustness for DNS of turbulence. In the GKM scheme, the solution for the velocity distribution function f in Eq.(3.1) is written as follows:

$$f(t+\Delta t, \vec{x}, \vec{u}) = \frac{1}{\tau}\int_t^{t+\Delta t} g(t', \vec{x}', \vec{u}) e^{-(t+\Delta t-t')/\tau} dt' + e^{-\Delta t/\tau} f_0(\vec{x} - \vec{u}\Delta t, \vec{u}) \,, \tag{3.13}$$

where $f_0(\vec{x}, \vec{u})$ is an initial distribution function at time t, and $\vec{x} - \vec{x}' = \vec{u}(t+\Delta t-t')$ is the particle trajectory. In the absence of discontinuities or shocks, the above solution is simplified to

$$f(t,\vec{x},\vec{u}) = \frac{1}{\tau}\int_{-\infty}^{t} g(t',\vec{x}',\vec{u})e^{-(t-t')/\tau}dt' \,, \tag{3.14}$$

where g is the only unknown. In order to construct g across a cell interface, Taylor series expansion is used around $\vec{x}_0$ at the beginning of each time step ($t = 0$). The equation is then

$$\begin{aligned} g(t,\vec{x},\vec{u}) &= g_0 + (\vec{x}-\vec{x}_0)\cdot\nabla g + t\frac{\partial g}{\partial t} & (3.15)\\ &= g_0\left[1 + a(x-x_0) + b(y-y_0) + c(z-z_0) + At\right] \,, & (3.16)\end{aligned}$$

where $g_0 = g(0,\vec{x}_0,\vec{u})$ is the Maxwellian equilibrium function at $t = 0$. Inserting this expression into the analytical solution (3.14), the velocity distribution function at cell interfaces becomes

$$f(t,\vec{x}_0,\vec{u}) = g_0\left[1 - \tau(au + bv + cw) + (t-\tau)A\right] \,. \tag{3.17}$$

The unknown coefficients a, b, and c can be determined from the macroscopic flow variables Q at the beginning of each time step using

$$Q \equiv [\rho\ \rho U\ \rho V\ \rho W\ E]^T = \int \psi f dudvdwd\xi \,, \tag{3.18}$$

where

$$\begin{aligned} \psi &= \left[1,\, u,\, v,\, w,\, \frac{1}{2}(u^2+v^2+w^2+\xi^2)\right]^T \,, & (3.19)\\ E &= \frac{1}{2}\rho\left(U^2+V^2+W^2+\frac{K+3}{2\lambda}\right) \,. & (3.20)\end{aligned}$$

The coefficient A in Eq.(3.17) can be obtained from the compatibility condition, which states that the collision does not change the conservation of mass, momentum, and energy:

$$\int (g-f)\,\psi dudvdwd\xi = 0 \,. \tag{3.21}$$

On each cell interface, the fluxes are represented by

$$\vec{F} = \int \vec{u}\psi f dudvdwd\xi \,. \tag{3.22}$$

Then, the macroscopic variables Q are updated as

$$Q(t+\Delta t) = Q(t) + \frac{1}{\Delta_c}\int_0^{\Delta t}\int \vec{F}\cdot d\vec{A}\,dt\,, \tag{3.23}$$

where Δt is the time step; Δ_c is the volume of the cell; and $\vec{A}$ is the area of cell interface. Details of GKM can be found in [41, 42, 43].

The Navier-Stokes equation can be recovered from the GKM solution (3.17) through the Chapman-Enskog expansion. This brings about the relationship between shear viscosity μ and the collision time τ of fluid particles as follows [34]:

$$\mu = \tau p\,, \tag{3.24}$$

where p is the thermodynamic pressure and τ is the collision (or relaxation) time of a fluid particle. Bulk viscosity is related to collision time and pressure as follows:

$$\mu_B = \frac{2}{3}\frac{K}{K+3}\tau p\,, \tag{3.25}$$

where bulk viscosity is also proportional to the collision time and thermodynamic pressure. In Eq.(3.25), K is the internal degree of freedom of fluid particles and is described as

$$K = \frac{5-3\gamma}{\gamma-1}\,, \tag{3.26}$$

where γ is the specific heat ratio. For example, monatomic gas has the specific heat ratio of $\frac{5}{3}$, which makes the internal degree of freedom $K = 0$. Thus, from Eq.(3.25), bulk viscosity μ_B is zero for monatomic gas as already seen from the concepts of mechanical and thermodynamic pressures in Chapter II. For diatomic gas, the specific heat ratio γ is $\frac{7}{5}$ and the internal degree of freedom K is 2. Then, the bulk viscosity μ_B is given as

$$\mu_B = \frac{4}{15}\tau p\,. \tag{3.27}$$

Thus, in diatomic gas flows, the magnitude of bulk viscosity is 27% of shear viscosity as seen in Eqs.(3.24) and (3.27).

CHAPTER IV

LATTICE BOLTZMANN DNS OF DECAYING COMPRESSIBLE ISOTROPIC TURBULENCE WITH TEMPERATURE FLUCTUATIONS

In this chapter, the heat release effect on low turbulent Mach-number compressible isotropic turbulence is investigated. Direct numerical simulation (DNS) of low Mach number decaying isotropic turbulence with randomly distributed initial temperature field is performed using the hybrid thermal lattice Boltzmann method (HTLBM). The objectives of the study are to (i) investigate the interaction between kinetic and thermal energy modes, and (ii) perform a preliminary examination of the small-scale flow structure. The results indicate that pressure plays a crucial role in the energy exchange between kinetic and thermal modes. Unlike dissipation, which generates one-way energy transfer from kinetic to thermal modes, pressure can lead to a two-way energy exchange. On average, pressure work transfers energy from thermal to kinetic modes in our computations. The analysis of velocity-gradient structure shows that, as in isothermal flow, the vorticity vector aligns with the intermediate eigenvector of the strain-rate tensor. However, the alignments among vorticity vector, pressure gradient, density gradient, and temperature gradient are significantly altered by temperature fluctuations. Our results demonstrate that HTLBM is a reliable tool for low turbulent Mach-number flows with temperature fluctuations.

A. Introduction

Compressible turbulence is inherently more complicated than its incompressible counterpart due to, among other reasons, the activation of the thermal energy mode. The

---

This chapter is a reprint of an article published in the INTERNATIONAL JOURNAL OF COMPUTATIONAL FLUID DYNAMICS, 20, 401-413, July 2006.

nonlinear interaction between kinetic and thermal energy modes is known to occur over a wide range of time and length scales [28]. It is also known that heat release and resulting temperature fluctuations may cause important changes in the structure of fluctuating velocity gradients [20]. The orientation of vorticity with respect to strain rate has important implications for cascade dynamics, scalar mixing, and other small-scale turbulence process [4, 44].

There have been several previous numerical studies of compressible turbulence to date. Kida and Orszag [15, 16, 17] studied the energy dynamics in decaying and forced compressible turbulence using direct numerical simulation (DNS) data. They decomposed the velocity field into compressible (dilatational) and rotational (solenoidal) components, and studied the compressibility effects using the ratio of these two components. They showed that the coupling between the two components of kinetic energy is weak and that most of the energy introduced to either component is transferred to the internal energy without passing through the other component. They also showed that the rotational component of energy spectrum obeys the same Kolmogorov similarity law as for incompressible turbulence, but the compressible component of the spectrum depends strongly on the Mach number. They argued that the compressible-to-rotational energy ratio converges to some universal value as the turbulence decays, while the Reynolds number and the Mach number decrease in time. Erlebacher and Sarkar [20] analyzed the strain-rate tensor using DNS results of compressible homogeneous shear turbulence. They decomposed the strain-rate tensor into solenoidal and dilatational parts. The structure of the solenoidal strain-rate tensor was found to be similar to that of incompressible turbulence. The dilatational strain-rate tensor was found to have a preferred structure in the regions of strong dilatation, and the alignment of pressure-gradient vector was found to be strongly affected by the compressibility.

The effect of heat release on compressible isotropic turbulence was considered by Jaberi *et al.*[28] at low turbulent Mach number. They showed that dilatational motions are affected more than solenoidal motions in the presence of heat release, and the pressure work tends to increase the turbulent kinetic energy. They also showed that the effect of heat release is to weaken the alignment of the vorticity vector with the intermediate eigenvector of the strain-rate tensor, due to the variation in molecular viscosity. Most of the compressible turbulence simulations to date [15, 16, 17, 20, 28] have been performed with the Navier-Stokes equations.

Over the last decade, the lattice Boltzmann method (LBM) has emerged as a powerful technique for simulating various fluid-flow phenomena, especially in complex geometry. Advantages and challenges of LBM for performing DNS and LES (Large Eddy Simulation) of turbulence are discussed in detail in [45, 46]. Some of the potential advantages of LBM over Navier-Stokes platform for performing turbulence simulations are: (1) LBM computational stencil involves only nearest neighbor interactions with simple grid connectivity and lower communication penalty than Navier-Stokes solvers. This leads to improved scaling properties over Navier-Stokes for parallel computations. (2) Due to the availability of additional flow information, Boltzmann-equation based approaches may be amenable to more accurate turbulence closure modeling. (3) In principle, Boltzmann-equation based approaches can be applied to flows over a wider range of Knudsen numbers.

It has now been clearly demonstrated in isothermal homogeneous turbulence that LBM can reproduce the NS (Navier-Stokes) DNS results and experimental data. Yu *et al.*[45, 46] demonstrated that LBM can accurately capture the decay exponents in isotropic turbulence. Yu and Girimaji [47, 48] performed LBM DNS of homogeneous shear turbulence. They demonstrated that LBM DNS accurately reproduces the anisotropy and kinetic energy evolution data of NS DNS and experimental investigations. More recently, Yu and Girimaji [49] have performed LBM LES of non-circular jets and their results compare favorably with experimental data. Thus, LBM can now be considered a reliable tool for performing DNS and, to a limited degree, LES of isothermal turbulence.

One of the earliest applications of LBM to non-isothermal flows can be found in [50]. Lallemand and Luo [39] popularized the hybrid thermal lattice Boltzmann method (HTLBM) which eliminates the unphysical coupling between the energy and shear modes of LBM and improves numerical stability. They used the multiple-relaxation-time lattice Boltzmann method (MRT-LBM) for mass and momentum conservations and the macroscopic equation for energy conservation. They applied the method to Rayleigh-Bénard convective flows in a cubic cavity with two opposite walls at different temperatures and showed that the results agree well with the pseudo spectral results. More recently, Chang and Alexander [51] applied HTLBM to a two-phase Rayleigh-Bénard convection problem. They used the single-relaxation-time lattice Boltzmann method (SRT-LBM) for mass and momentum conservation and the macroscopic equation for energy conservation. They showed that HTLBM can simulate complicated free surfaces and interface deformation. At this stage, HTLBM is ready for extension to non-isothermal turbulent flows.

In this chapter, we perform DNS of low Mach number isotropic turbulence decaying under the influence of randomly distributed initial temperature field using HTLBM. The objective of our investigation is two-fold. On the turbulence analysis side, we would like to investigate (i) the interactions between kinetic and thermal energy modes: i.e. the role of pressure work, solenoidal dissipation, and dilatational dissipation, and (ii) the effect of temperature fluctuations on the small-scale flow structure: i.e. the orientation of vorticity vector, pressure gradient, density gradient, and temperature gradient with respect to strain-rate eigen-direction. On the numerical side, we will attempt to establish the viability of HTLBM for DNS of turbulence with temperature fluctuations.

This chapter is organized as follows. In section B, the HTLBM theory is described briefly and its numerical implementation is discussed in detail. The implications of kinetic and internal energy equations are examined for the flow considered. In section C, we first verify that DNS simulation conserves total energy accurately. Then, we study in detail the interplay between turbulent kinetic energy and internal energy. This is followed by investigations of the structure of the strain-rate tensor, vorticity vector, and gradient vectors of thermodynamic variables. The summary and conclusions of this study are given in section D.

B. Hybrid thermal LBM implementation and energy equations

1. Hybrid thermal LBM

In HTLBM, the mass and momentum conservations are solved with MRT-LBM [40]:

$$|f(\vec{x}+\vec{e}_\alpha\delta t, t+\delta t)\rangle - |f(\vec{x},t)\rangle = -M^{-1}\hat{S}\left\{|m(\vec{x},t)\rangle - \left|m^{(eq)}(\vec{x},t)\right\rangle\right\}, \qquad (4.1)$$

where $|f\rangle$ is the velocity distribution function vector; $\hat{S}$ is a diagonal matrix and denotes the relaxation rates; $|m\rangle$ and $|m^{(eq)}\rangle$are respectively the current moment vector and the equilibrium moment vector; $\vec{x}$ is the position vector; $\vec{e}_\alpha$ is the discrete velocity in α velocity space coordinate direction; and M is the linear mapping matrix which transforms the velocity distribution function vector to the moment vector. The equation of state is implied in the LBM equation: $p = \rho c_s^2$, where p is the pressure and c_s is the speed of sound. The density and velocity fields are calculated using following relations:

$$\rho = \sum_{\alpha=0}^{N} f_\alpha \quad \text{and} \quad \vec{u} = \frac{\sum_{\alpha=0}^{N} \vec{e}_\alpha f_\alpha}{\rho},$$

where N denotes the velocity space dimension.

The energy conservation equation is solved in the macroscopic form:

$$\partial_t(\rho\tilde{e}) + \nabla\cdot(\rho\tilde{e}\vec{u}) = \kappa\nabla^2 T - p\nabla\cdot\vec{u} + \mu\left[\nabla\vec{u} + (\nabla\vec{u})^T\right]\nabla\vec{u} + \lambda(\nabla\cdot\vec{u})^2, \qquad (4.2)$$

where $\tilde{e}$ is the internal energy per unit mass ($\tilde{e} = c_v T$); μ is the shear viscosity; λ is the bulk viscosity (definition of bulk viscosity in this chapter is different from that of Chapter II: $\lambda = \mu_B - \frac{2}{3}\mu$); T is the temperature; and κ is the thermal conductivity of the fluid. We adopt this complete energy equation contrary to Lallemand and Luo [39], who neglect viscous work and solve the following simpler equation:

$$\partial_t(\rho\tilde{e}) + \nabla\cdot(\rho\tilde{e}\vec{u}) = \kappa\nabla^2 T - p\nabla\cdot\vec{u}.$$

As the MRT-LBM used for the mass and momentum equations is first-order in time, equation (4.2) is also solved with a first order finite-difference discretization:

$$\begin{aligned}\rho\tilde{e}(\vec{x}, t+\delta t) = \rho\tilde{e}(\vec{x}, t) \quad &+ \quad \delta t\left\{-\nabla\cdot(\rho\tilde{e}\vec{u}) + \kappa\nabla^2 T - p\nabla\cdot\vec{u}\right\}\\ &+ \quad \delta t\left\{\mu\left[\nabla\vec{u} + (\nabla\vec{u})^T\right]\nabla\vec{u} + \lambda(\nabla\cdot\vec{u})^2\right\}. \qquad (4.3)\end{aligned}$$

In the above equation, the spatial derivatives on the right-hand side are calculated using a higher order finite-difference operator whose stencil has the same number of points as the discrete velocity set in MRT-LBM model [39].

MRT-LBM equation (4.1) and the macroscopic energy equation (4.3) are coupled through the energy mode in MRT-LBM model:

$$m_e^{(eq)} = m_e^{(eq)}(\rho,\ \vec{u},\ \gamma,\ T).$$

In the absence of the viscous work terms in equation (4.3), our HTLBM model is identical to that of [39]. As the Lallemand and Luo algorithm[39] is reasonably well tested and validated, we do not perform any further validation studies. Inclusion of the viscous work terms, however, makes an internal consistency check possible. In this chapter, we will examine if the HTLBM model conserves energy during the energy exchange between kinetic and thermal modes. We will seek to demonstrate total energy conservation and this will serve as a validation of the novel feature added in the present work. Further details of HTLBM can be found in [39].

2. Numerical implementation

All simulations are performed in a periodic cube with 128^3 resolution. The initial incompressible isotropic random velocity and temperature fields are generated using the same procedure as [46] but with different initial wave-number contents. The objective is to produce initial incompressible velocity and temperature fields of different length scales. The initial pressure field is found by solving a Poisson equation. After setting the initial incompressible conditions for velocity and pressure, the temperature field is added, and the velocity and temperature fields are allowed to evolve. The presence of temperature fluctuations gives rise to compressibility effects. If there are no temperature fluctuations initially, the turbulence field will experience incompressible decay. The parameters of different simulations are summarized in Table I. The initial velocity fields are the same for all three cases.

The three-dimensional 19-velocity (D3Q19) MRT-LBM model[40]) is used in our computations. The shear and bulk viscosities are controlled with $s_9(= s_{13})$ and s_1 in relaxation matrix ($\hat{S}$), which are set to be 1.923 and 1.19, respectively. This leads to the initial Taylor-scale Reynolds number of 45. The other relaxation rate components are given in [40].

The values used for the specific heat ratio and the thermal diffusivity are 1.2 and 0.0111, respectively. This corresponds to the Prandtl number of 0.6, which is close to that of air. The initial turbulent Mach number is 0.25, which is within the allowable maximum Mach number of 0.33 for the MRT-LBM model [40].

Table I. Simulation cases

Simulation cases	Isothermal	Case I	Case II
Computational domain	128^3	128^3	128^3
Initial velocity field wave-number	1∼8	1∼8	1∼8
Initial temperature field wave-number	0(T=constant)	1∼4	5∼8
Initial Taylor-scale Reynolds number	45	45	45
Prandtl number	0.6	0.6	0.6

3. Energy equations

The turbulent kinetic energy, internal energy, and total energy are defined as

$$k \equiv \tfrac{1}{2}\overline{\rho u_i u_i}, \quad e \equiv \overline{\rho \tilde{e}}, \quad \text{and} \quad E = k + e,$$

where over-bar indicates spatial average and repeated indices imply summation. The turbulent kinetic energy equation can be easily obtained from the momentum equation. After neglecting the transport terms due to the homogeneity of flow field, the turbulent kinetic energy equation can be written as

$$\frac{\partial k}{\partial t} = PW - SD - DD. \tag{4.4}$$

In the above equation, pressure work (PW), solenoidal dissipation (SD), and dilatational dissipation (DD) are given by

$$PW \equiv \overline{pS_{kk}}; \quad SD \equiv 2\mu\overline{\Big(S_{ij} - \frac{1}{3}S_{kk}\delta_{ij}\Big)\Big(S_{ij} - \frac{1}{3}S_{kk}\delta_{ij}\Big)}; \quad DD \equiv \Big(\lambda + \frac{2}{3}\mu\Big)\overline{S_{kk}^2},$$

where S_{ij} is the strain-rate tensor defined as $S_{ij} \equiv (\partial_j u_i + \partial_i u_j)/2$.

The internal energy equation can be written, subject to the homogeneity assumption, as

$$\frac{\partial e}{\partial t} = -PW + SD + DD. \tag{4.5}$$

As the solenoidal and dilatational dissipation are non-negative, they transfer energy exclusively from the kinetic to thermal modes. The pressure work, on the other hand, can be of either sign, enabling two-way energy transfer.

From equations (4.4) and (4.5), the evolution equation for the total energy can be formed:

$$\frac{\partial E}{\partial t} = 0. \tag{4.6}$$

Thus, the total energy is conserved in our computational domain. Our focus in this study is on the interplay between the kinetic and thermal energy modes, especially on the role of pressure work.

C. Results and discussions

1. Energy conservation

First, we seek to establish that the total energy is conserved in our numerical scheme. The temporal evolution of the kinetic, internal, and total energy is plotted in Fig. 5. The time scale is non-dimensionalized by the initial eddy turn-over time. The kinetic, internal, and total energy at time t are denoted respectively by $k(t)$, $e(t)$, and $E(t)$. The initial values of the kinetic and internal energy are k_0 and e_0. In the isothermal case, kinetic energy decreases and internal energy increases monotonically in time

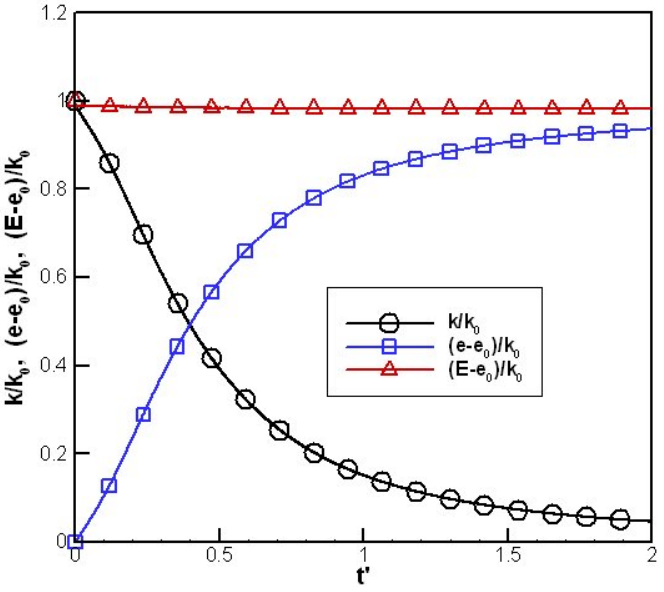

(a) Isothermal case

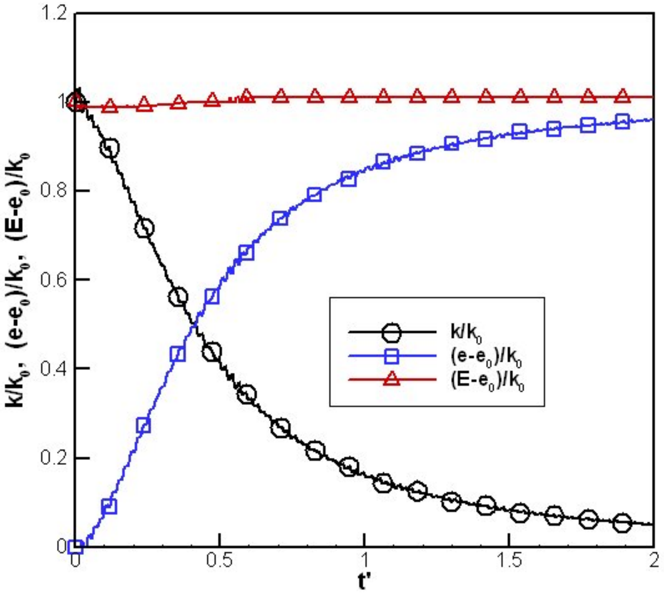

(b) Case I

Fig. 5. Kinetic, internal, and total energy

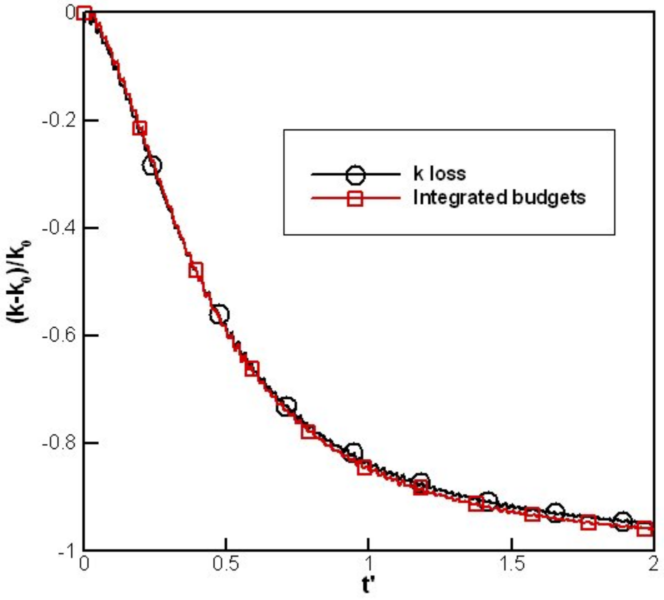

(a) Kinetic energy budget

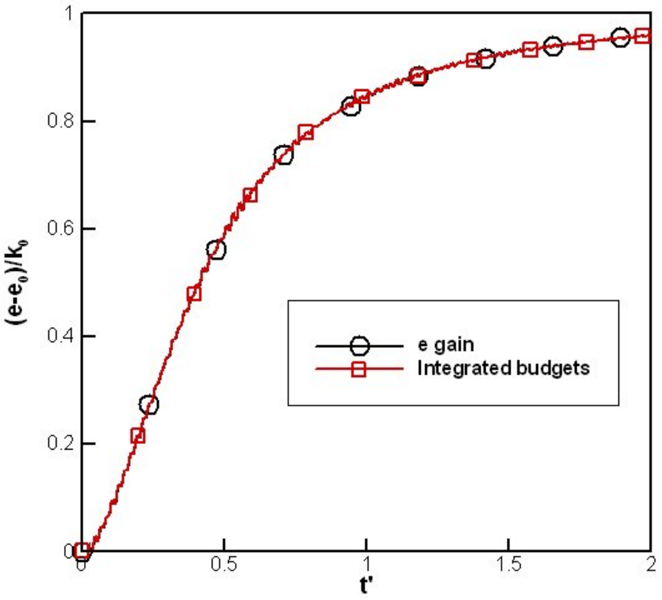

(b) Internal energy budge

Fig. 6. Budgets for the kinetic and internal energy (Case I)

keeping the total energy constant. In the non-isothermal case (Case I), the overall behavior is similar to that of the isothermal case but the details are different. The kinetic energy and internal energy curves display small amplitude but high frequency variations. These variations are not due to any numerical instability as each cycle of variation is over 40 time steps long. They are caused by rapid back-and-forth exchange of energy between the kinetic and thermal modes due to the action of pressure work. It is important to note that the total energy curve is entirely smooth and exhibits very little change from the initial value. Case II also exhibits similar behavior. It is therefore clear that total energy is conserved in all cases.

To further demonstrate the accuracy of energy conservation, we now present two different computations of the evolution of the kinetic and internal energy difference $\{k(t) - k_0\}$ and $\{e(t) - e_0\}$ for Case I (Fig. 6). The line with open circles directly corresponds to the energy difference from the values of $k(t)$ and $e(t)$ as computed from the code. In the second method of calculation, we integrate the right hand side of the energy budget equations (4.4) and (4.5) as follows:

$$k(t) - k_0 = \int_0^t (PW - SD - DD)\, d\tau,$$

$$e(t) - e_0 = \int_0^t (-PW + SD + DD)\, d\tau.$$

The line with open squares corresponds to the value of the energy difference obtained from these integrations. The agreement between the two computations shows that our simulations are of high numerical fidelity. Similar agreement is also obtained for the isothermal case and Case II. It must be noted that we use the explicit Euler method in the above time integration of each energy equation, as LBM is first order accurate scheme in time.

2. Energy exchanges between kinetic and thermal modes

The energy exchange between kinetic and thermal modes is now investigated. The temporal evolution of the kinetic and internal energy is plotted for three different cases in Fig. 7. In the isothermal case, kinetic energy is transferred into internal energy monotonically and smoothly. In non-isothermal cases (Case I and Case II), the kinetic energy variation has small amplitude and high frequency oscillations superposed on a gradual and smooth decay. Overall level of kinetic energy decreases over a long period of time at approximately the same rate as that of the isothermal case. The smooth decay is due to the solenoidal dissipation, whereas the rapid but small undulations are due to the pressure work. The frequency of kinetic energy variation is higher in Case II, in which the length-scale of initial temperature field is smaller.

To further examine these phenomena, we investigate each term in the turbulent kinetic energy equation (4.4): pressure work (PW), solenoidal dissipation (SD), and dilatational dissipation (DD). In the isothermal case, the solenoidal dissipation accounts for all of the kinetic energy decrease, and the pressure work and dilatational dissipation are negligible as expected (Fig. 8(a)). In the non-isothermal cases (Case I and Case II), the temperature fluctuations do not have as much effect on the solenoidal dissipation as on the pressure work (Fig. 8(b),(c)). Clearly, the pressure work plays a crucial role in the energy transfer between the kinetic and thermal modes. The amplitude of the pressure work variation is smaller in Case II than in Case I, as the temperature field decays faster due to the smaller initial length scale and the flow field approaches the isothermal state more rapidly. For the same reason, the pressure work in Case II decreases faster than in Case I. The frequency of the pressure work variation is higher in Case II than in Case I. The pressure work time-scale is much smaller than the turbulence time-scale. From our study, it appears that the length

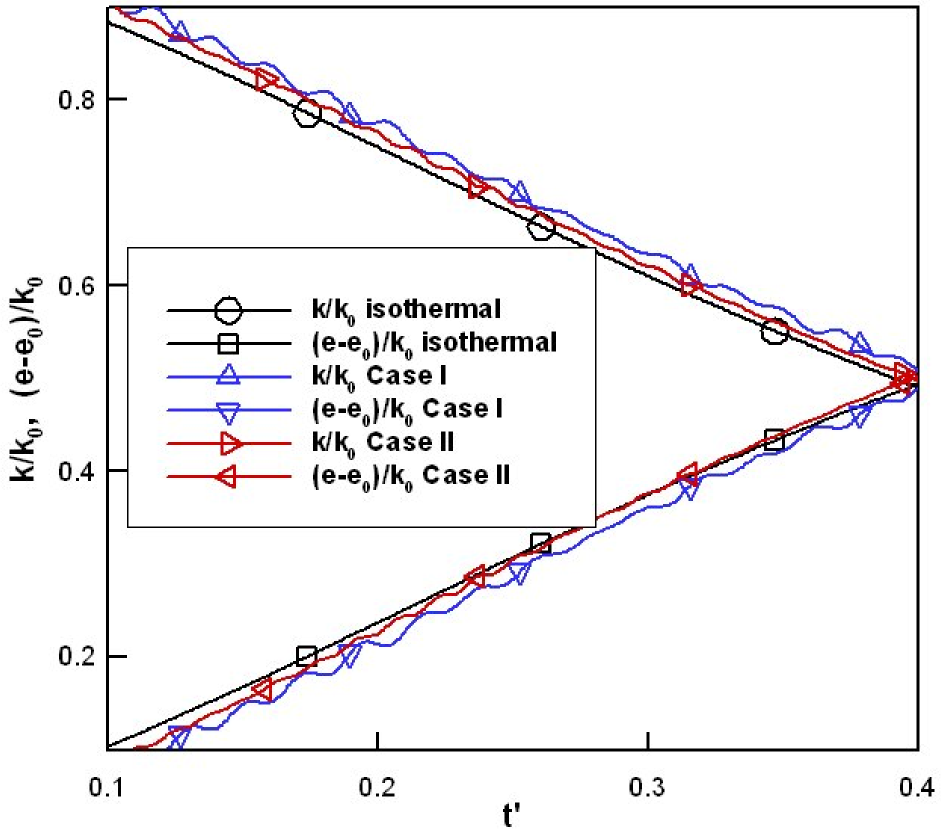

Fig. 7. Temporal variation of kinetic and internal energy

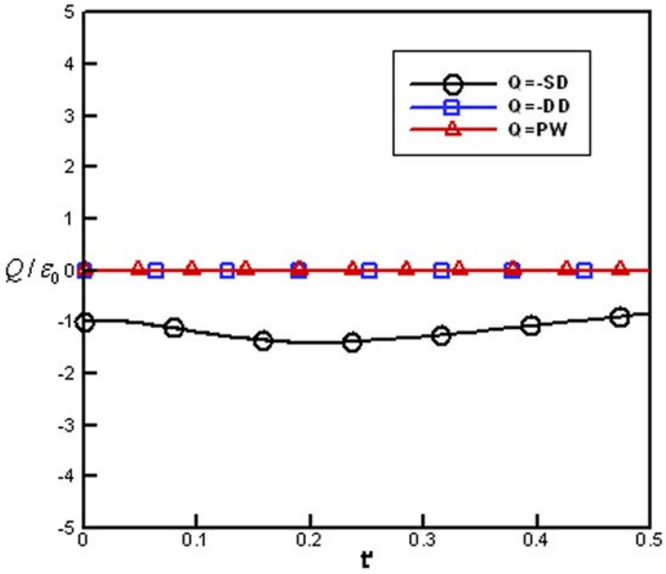

(a) Isothermal

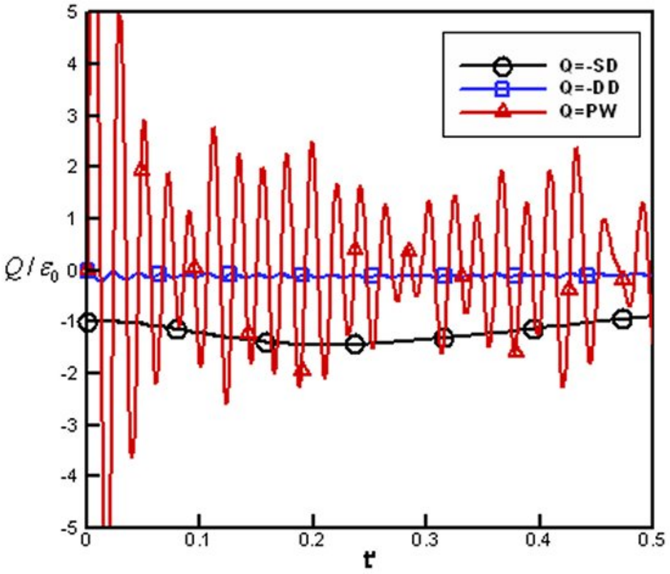

(b) Case I

Fig. 8. Temporal variation of the kinetic energy budgets

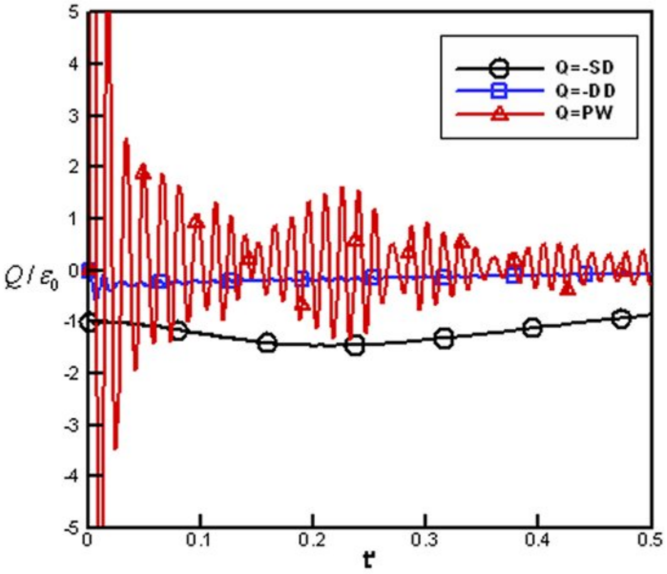

(c) Case II

Fig. 8. Continued

scale of temperature fluctuations influences the time scale of pressure work. The dilatational dissipation also varies at nearly the same time scale as the pressure work, but the amplitude is much smaller. It should be reiterated here that each pressure work cycle is temporally well-resolved with over 40 time steps.

The temporal evolution of the kinetic energy and the pressure work are compared in Fig. 9. It appears that the phase difference between them is 90 degrees, which is the same value as observed in the forced compressible turbulence by Kida and Orszag [16]. It is therefore clear that the high frequency of the kinetic energy variation is driven by the pressure work. The relation between the kinetic energy and the pressure work is investigated further in wave-number space for Case I (Fig. 10(a),(b)). The kinetic energy and pressure work at a specific wave number are given by

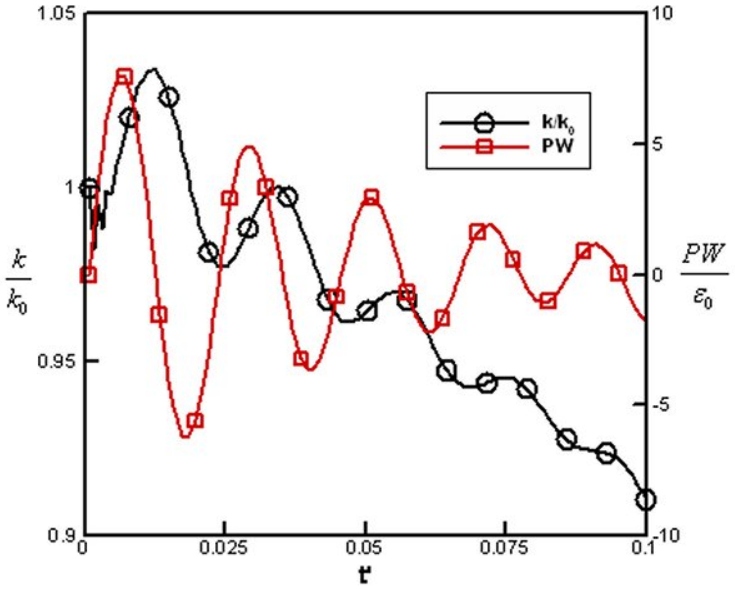

Fig. 9. Temporal variation of the pressure work and the kinetic energy (Case I)

$$\hat{E}(\kappa) = \frac{1}{2}\hat{w}_i(\kappa)\hat{w}_i^*(\kappa);$$

$$P\hat{W}(\kappa) = Re\{j\kappa_i\hat{u}_i(\kappa)\hat{p}^*(\kappa)\},$$

where $w_i = \sqrt{\rho}u_i$ and over-hat and superscript respectively denote Fourier transform and complex conjugate. It is clear from Fig. 10(b) that pressure work activity is confined to the large scales. It appears that the length scale of the pressure work activity is the same as that of the temperature fluctuations. It is also important to note that contribution from the pressure work to the kinetic energy at a given wave number can be positive or negative. When integrated over time, the net contribution by pressure work to the kinetic energy at a given wave number is quite small.

The net kinetic energy, transferred by pressure work at large scales, cascades to the smaller scales as seen in Fig. 10(a). In small scales, the kinetic energy ultimately

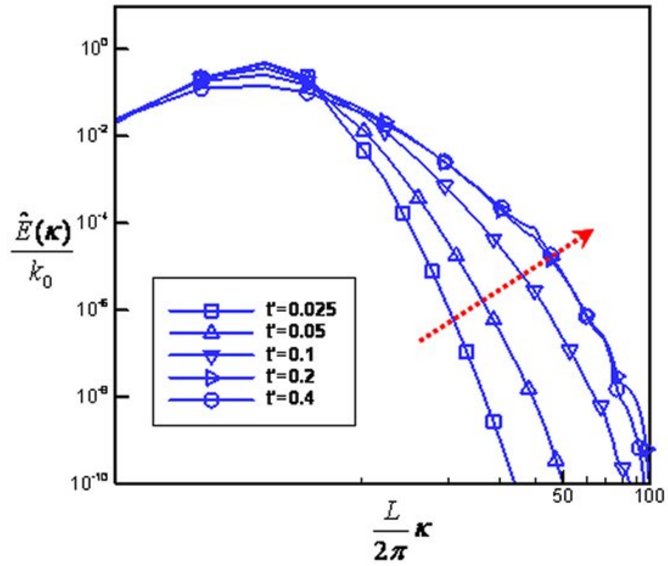

(a) Kinetic energ

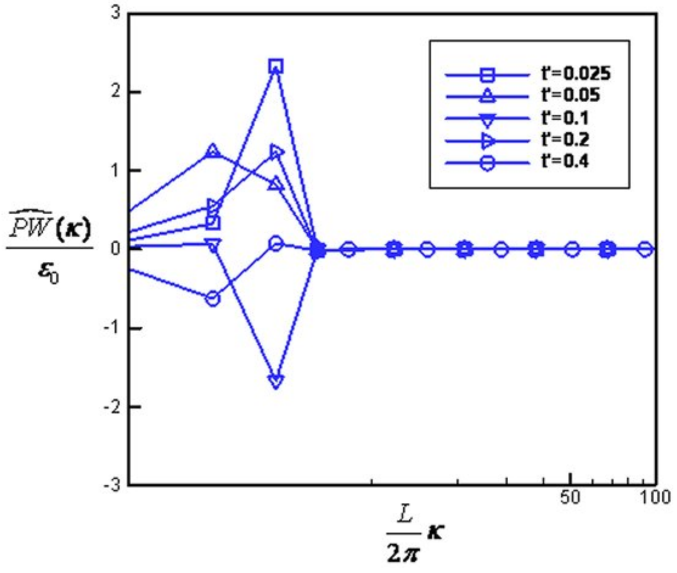

(b) Pressure work

Fig. 10. Kinetic energy, pressure work, solenoidal and dilatational dissipation in wave-number space (Case I)

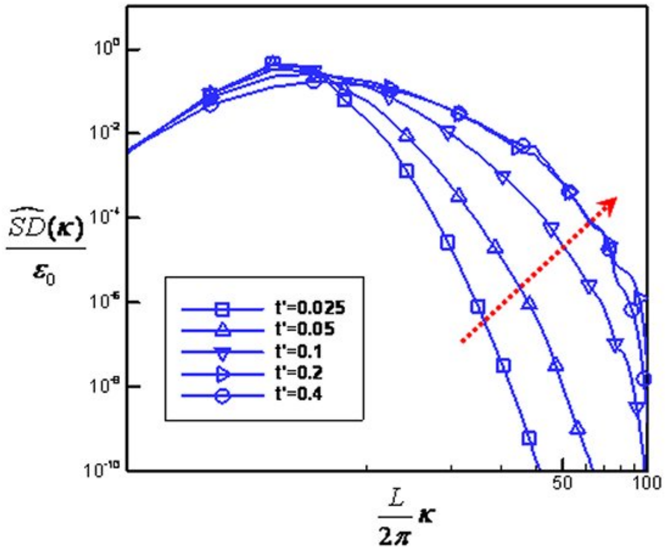

(c) Solenoidal dissipation

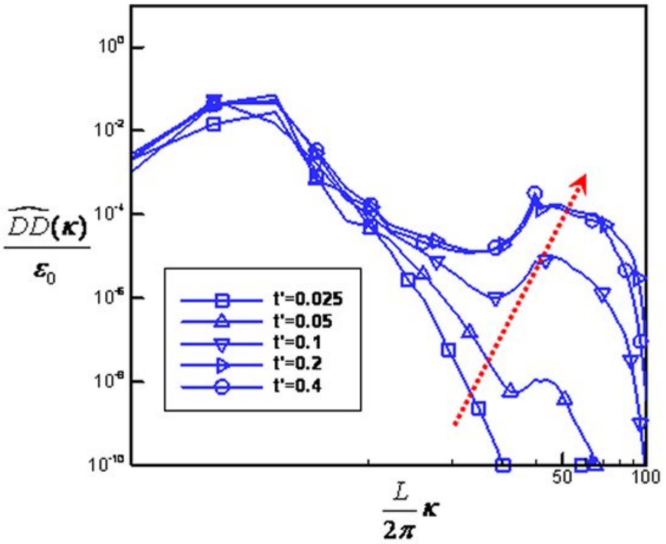

(d) Dilatational dissipation

Fig. 10. Continued

dissipates into thermal energy through solenoidal and dilatational dissipation. To better understand the two types of dissipation, we study the solenoidal and dilatational parts in wave-number space for Case I (Fig. 10(c),(d)). The solenoidal and dilatational dissipation are given by

$$\hat{SD}(\kappa) = Re\{\mu\kappa^2\hat{u}_i(\kappa)\hat{u}_i^*(\kappa) + \frac{1}{3}\mu\kappa_i\kappa_j\hat{u}_i(\kappa)\hat{u}_j^*(\kappa)\};$$

$$\hat{DD}(\kappa) = Re\{(\lambda + \frac{2}{3}\mu)\kappa_i\kappa_j\hat{u}_i(\kappa)\hat{u}_j^*(\kappa)\}.$$

Contrary to the pressure work, the solenoidal and dilatational dissipation are active over a wide range of wave numbers as turbulence decays. Especially interesting is the fact that the dilatational dissipation is much smaller in the intermediate scales than in the small scales. The saddle-shape of the dilatational dissipation spectrum is distinctly different from that of the solenoidal dissipation spectrum. After about one eddy turn-over time, it is found that nearly 15% of the large-scale dilatational fluctuations are converted to solenoidal fluctuations. Most of the large-scale dilatational fluctuations (85%) cascade down to small-scale without conversion and are ultimately expended as dilatational dissipation. In the forced isotropic turbulence simulations of Kida and Orszag (1990b), only 1% of large-scale dilatational fluctuations was converted to solenoidal form. However, about 1 to 6% of large-scale solenoidal fluctuations was converted to dilatational form. Overall, it appears that the conversion of fluctuations from one form to another is a strong function of the length scale of the initial fields and Mach number.

To confirm the long-time effect of the pressure work and dilatational dissipation, the evolution of the integral of each term in the kinetic energy budget equation (4.4) is studied for three cases in Fig. 11. In the isothermal case, the pressure work and dilatational dissipation are negligible. In the non-isothermal cases, the overall effect

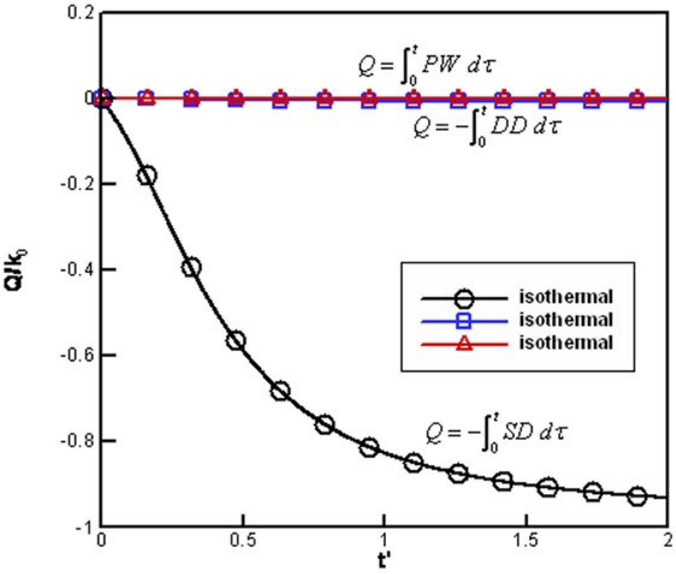

(a) Isothermal

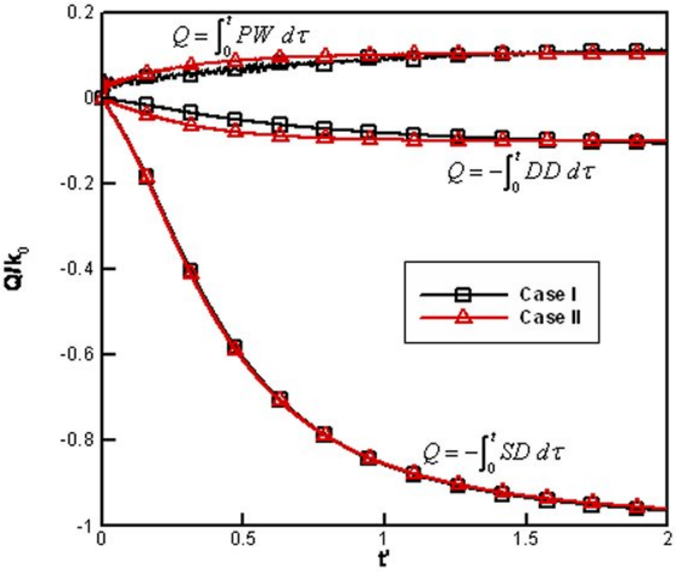

(b) Case I & Case II

Fig. 11. Temporal variation of accumulated kinetic energy budgets

of the pressure work is to transfer energy from the thermal to kinetic modes at large scales, while that of the dilatational dissipation is to transfer energy from the kinetic to thermal modes at small scales. The velocity field with small-scale temperature fluctuations (Case II) experiences this effect at earlier times, even though the energy budgets become equivalent after two eddy turn-over times (Fig. 11(b)). Thus, in our simulations, the effect of temperature fluctuations on turbulence exists only during the early period due to the initial imbalance in the pressure field.

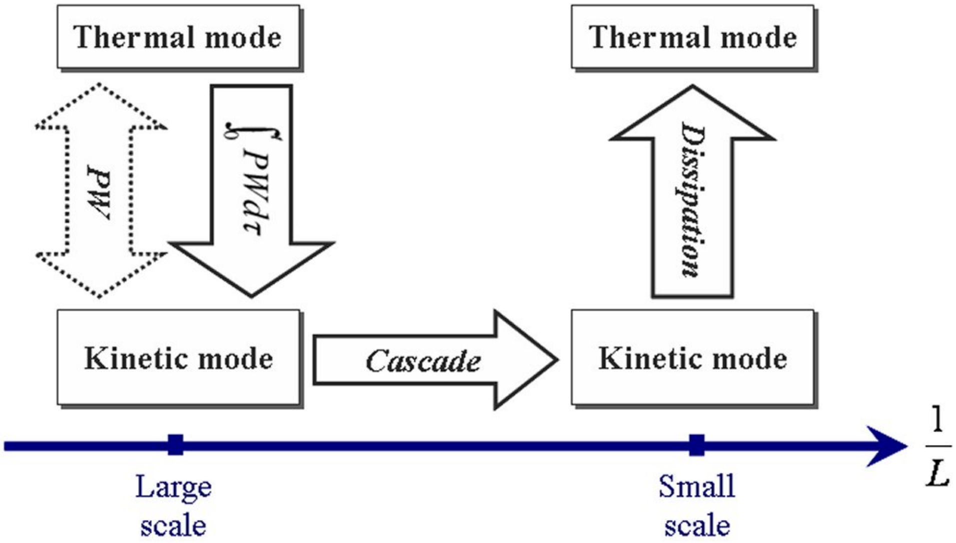

Fig. 12. Schematic of the interaction between kinetic and thermal modes

A schematic of the interaction between the kinetic and thermal modes is summarized in Fig. 12, in which an arrow denotes the direction of energy transfer: (1) Pressure work transfers energy back and forth between the kinetic and thermal modes in the presence of temperature fluctuations (Fig. 8(b), (c)). The thermal energy is initially transferred into the kinetic energy by the action of pressure work and most of the dilatational fluctuations are transferred back to the thermal energy. The energy-exchange cycles take place on a much shorter time scale than that of turbulence and at the same length scale as the temperature fluctuations. (2) Over each transfer cycle, there is a small net flow of energy from the thermal to kinetic modes. This net transfer from the thermal to kinetic modes adds up to significant accumulation over the duration of the simulation (Fig. 11(b)). Thus, the pressure work transfers energy from the thermal to kinetic modes in the same length scale as that of the temperature fluctuations. (3) This transferred kinetic energy is deposited as a dilatational velocity field (Fig. 10(b)). (4) The large-scale dilatational fluctuations then cascade to small scales (Fig. 10(a)). During the cascade process, most of the dilatational fluctuations remain in that form, whereas a small fraction (15%) is transformed into solenoidal fluctuations. (5) Eventually, the solenoidal and dilatational dissipation transfer the dilatational fluctuations to thermal energy at small scales (Fig. 10(c), (d)). As the process proceeds from step 1 through 5, the initial large-scale thermal energy fluctuations are ultimately uniformly distributed over the flow domain by turbulence.

The temporal variation of dissipation rate is plotted in Fig. 13. The dissipation rate is also influenced by temperature fluctuations, even though the effect is small. The dissipation rate is increased initially by the temperature fluctuations and shows almost the same value as in the isothermal case after one eddy turn-over time. The dissipation rate is higher initially in Case II than in Case I. Thus, the kinetic energy is transferred to the internal energy more rapidly in the small-scale temperature field (Case II) than in the large-scale one (Case I). The Reynolds number oscillates in the presence of temperature fluctuations as can be seen in Fig. 14. The Reynolds number is slightly higher in Case I than in Case II at early times. Overall, the Reynolds number decreases at the same rate in all three cases.

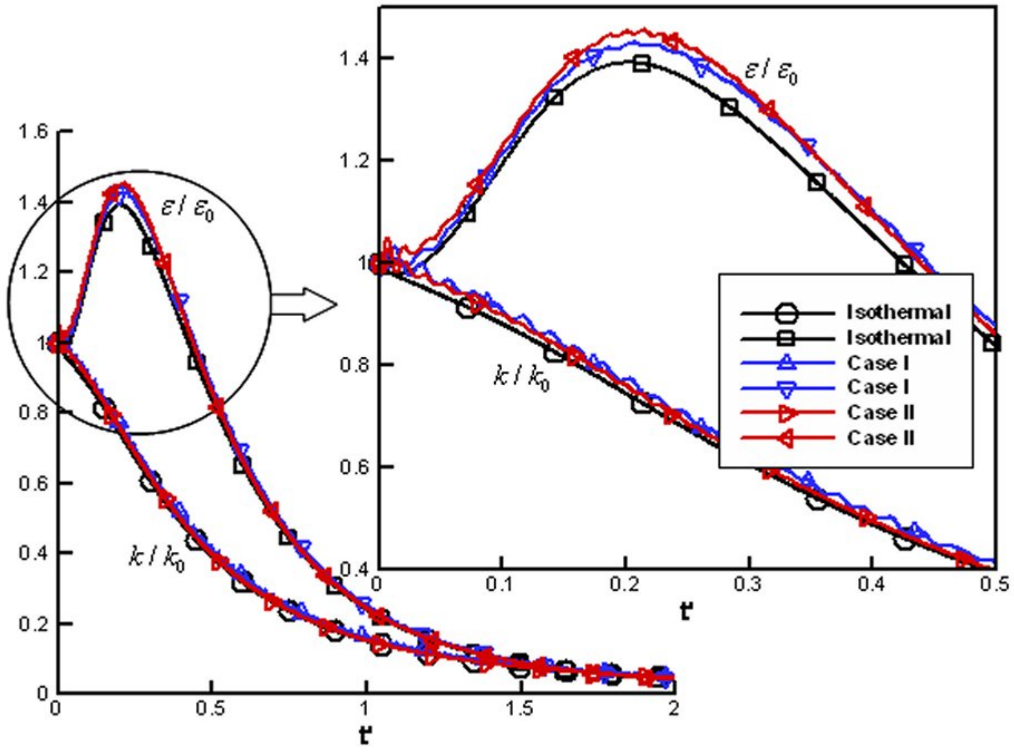

Fig. 13. Temporal variation of the kinetic energy and the dissipation rate

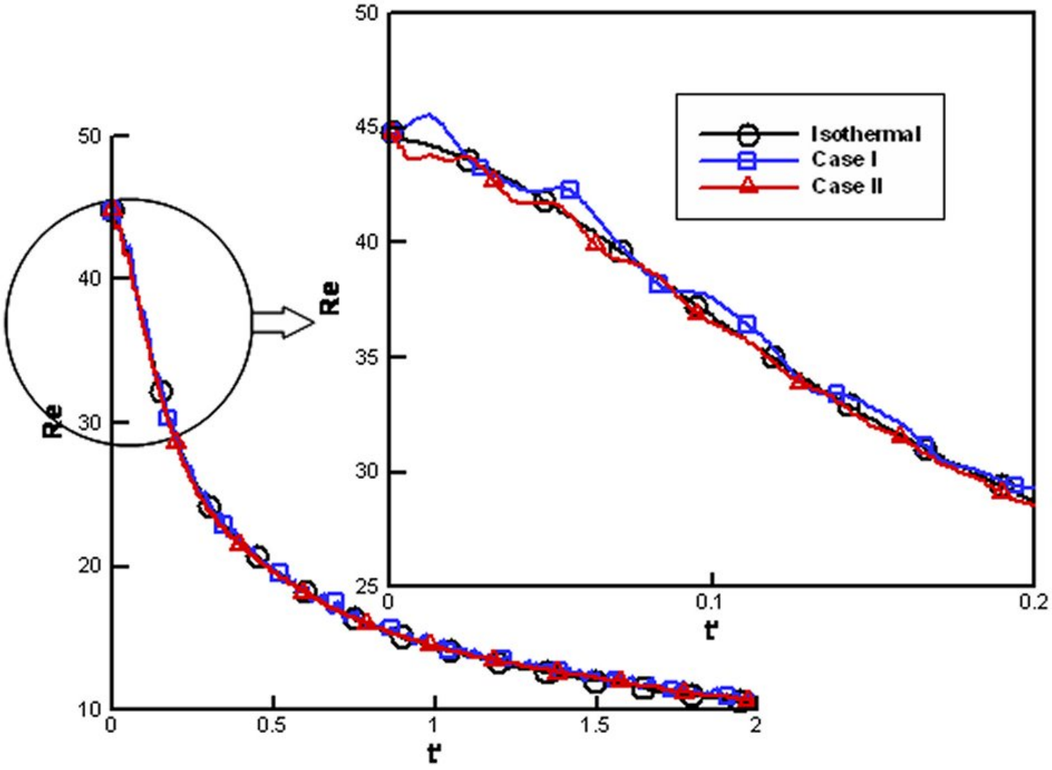

Fig. 14. Temporal variation of Reynolds number

3. Small-scale flow structure

We now investigate the effect of temperature fluctuations on the geometry of the gradients of velocity and thermodynamic variables. First, the variances of temperature, pressure, and temporal velocity gradient (TVG) are investigated in Fig. 15. The TVG is defined as a time derivative of velocity at a fixed point as follows:

$$\frac{\partial \vec{u}}{\partial t} \equiv \left(\frac{\partial u_x}{\partial t}, \frac{\partial u_y}{\partial t}, \frac{\partial u_z}{\partial t} \right).$$

The temperature variance in Case II decays faster than in Case I, which is consistent with the observations in the previous section. The frequency and amplitude of $< p'^2 >$ variation is nearly twice that of $< T'^2 >$ variation. It appears that the frequency of TVG variance is even higher. It is also important to note that in non-isothermal cases, the thermal fluctuations generate the TVG even though the kinetic energy decays at the same rate as in the isothermal case. The variance of TVG is higher in Case II than in Case I at early times. This is due to the fact that more of the thermal energy is transferred to the kinetic energy by the action of pressure work in Case II at early times (See Fig. 11(b)).

Now, we turn our attention to the strain-rate tensor. The eigenvalues of the strain-rate tensor are denoted by α, β, and γ, which are ordered from the largest to the smallest value. The eigenvalues are normalized with the root-mean square of the eigenvalues, $(\alpha^2 + \beta^2 + \gamma^2)^{1/2}$. The probability density function (PDF) of the eigenvalues of the strain-rate tensor at $t' = 0.4$ is plotted in Fig. 16. The distribution of the compressive eigenvalue (γ) is affected more than that of the other eigenvalues (α, β) in the presence of temperature fluctuations. Overall, larger ranges of values of α and γ are seen in the non-isothermal cases. The degree of impact of the temperature fluctuations is independent of the initial temperature length-scale in

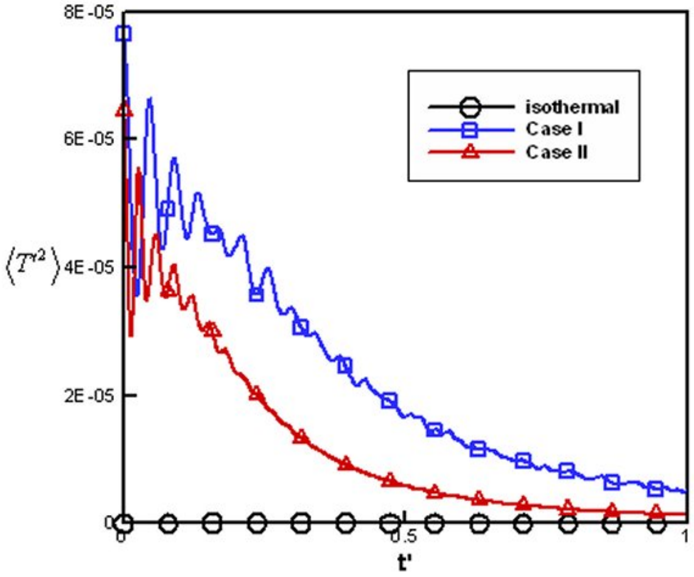

(a) Temperature variance

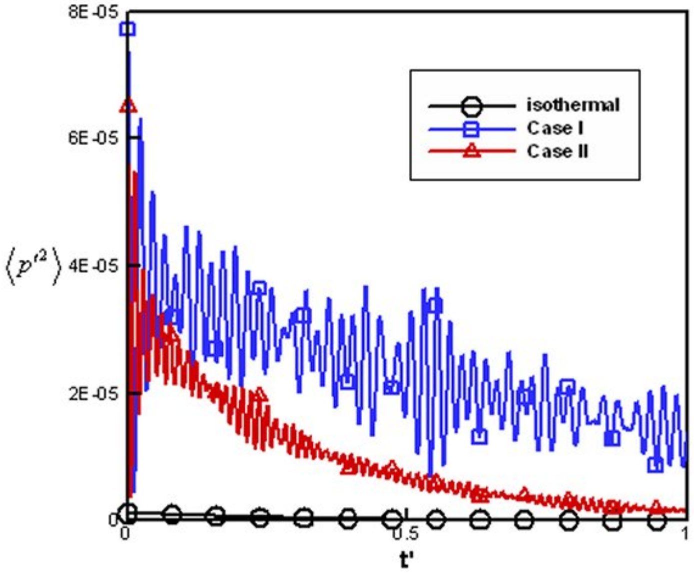

(b) Pressure variance

Fig. 15. Variance of temperature, pressure, and temporal velocity gradient

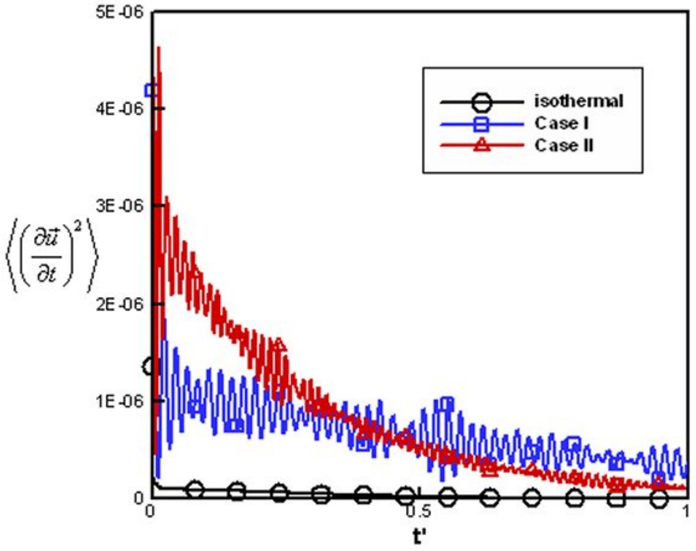

(c) Variance of temporal velocity gradient

Fig. 15. Continued

our computations.

The effect of temperature fluctuations on the alignment of vorticity vector with the eigenvectors of strain-rate tensor at $t' = 0.4$ is shown in Fig. 17. The angles between the vorticity vector and the eigenvectors corresponding to α, β, and γ eigenvalues are denoted by ζ_1, ζ_2, and ζ_3. The result shows no significant change in the alignment. This is contrary to Jaberi *et al.*[28], who showed that the effect of heat release is to decrease the alignment of the vorticity vector with the intermediate eigenvector and to increase the alignment with the largest eigenvector. In their work, the viscosity was allowed to change as a function of temperature. It would appear that their observation is due to variable viscosity rather than temperature fluctuations alone.

Next, the alignments among the vorticity vector, pressure gradient, density gradient, and temperature gradient are investigated. In the isothermal case, with high

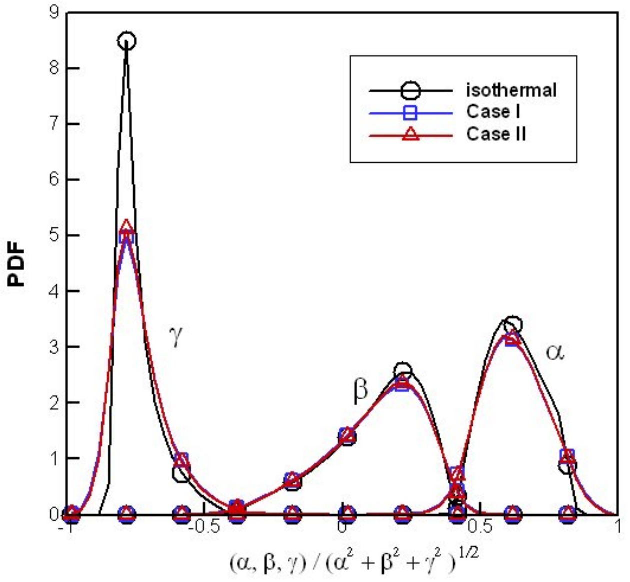

Fig. 16. PDF of eignenvalues of strain-rate tensor ($t' = 0.4$)

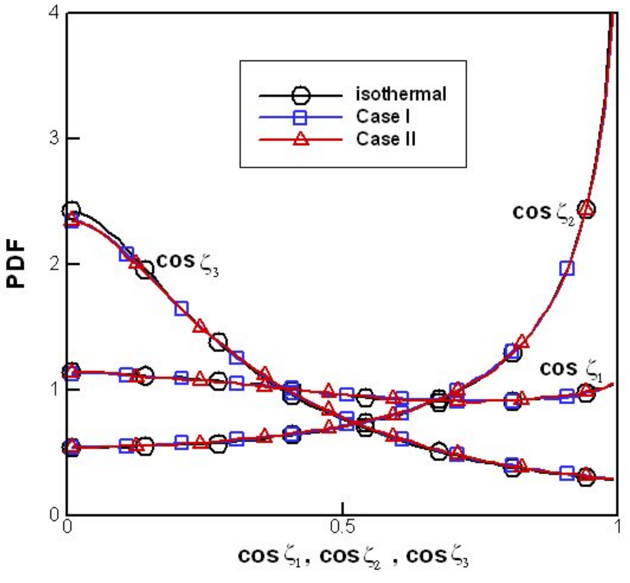

Fig. 17. Alignments of vorticity vector with eigenvectors of strain-rate tensor ($t' = 0.4$)

probability, the vorticity vector is perpendicular to the density, temperature, and pressure gradients as shown in Fig. 18(a), (b), and (c). The probability of vorticity being perpendicular to the density gradient is higher in Case I and unchanged from the isothermal case in Case II (Fig. 18(a)). The temperature fluctuations also increase the probability that the vorticity vector is perpendicular to the temperature gradient (Fig. 18(b)). The vorticity vector is perpendicular to the temperature gradient with higher probability in Case I than in Case II. However, the temperature fluctuations make the PDF of the angle between the vorticity vector and the pressure gradient nearly uniform as can be seen in Fig. 18(c). Thus, the pressure gradient is not correlated with the vorticity vector in the presence of temperature fluctuations in our simulations.

The pressure, density, and temperature gradients are preferentially aligned with each other in the isothermal case as shown in Fig. 18(d), (e), and (f). The temperature fluctuations improve the alignment of density gradient with temperature gradient (Fig. 18(d)), whereas they tend to reduce the preferential alignment of the pressure gradient with the density and temperature gradients (Fig. 18(e) and (f)). Especially, the PDF of the angle between the pressure and temperature gradients becomes nearly uniform in the presence of temperature fluctuations as can be seen in Fig. 18(f). Overall, the large-scale temperature field (Case I) modifies the alignment characteristics among the gradients of thermodynamic variables more than the small-scale one (Case II). This is probably due to the fact that the large-scale dilatational fluctuations produced in Case I dissipate slowly and therefore have longer duration to influence flow physics. In Case II, the dilatational fluctuations are produced in the smaller scales and they dissipate rapidly before they can have a significant effect on the flow physics.

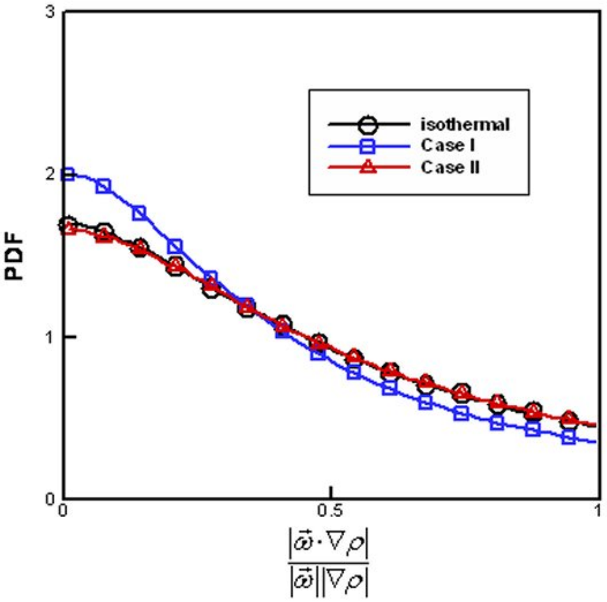

(a) Density gradient & vorticity

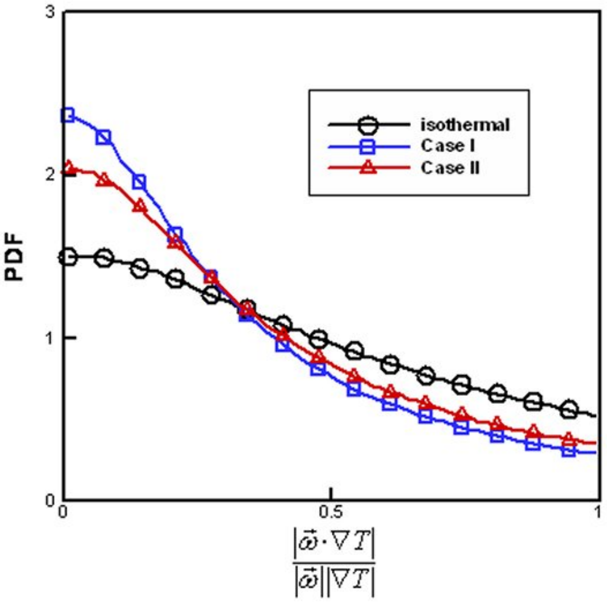

(b) Temperature gradient & vorticity

Fig. 18. Alignments among vorticity vector and gradient vectors of thermodynamic variables ($t' = 0.4$)

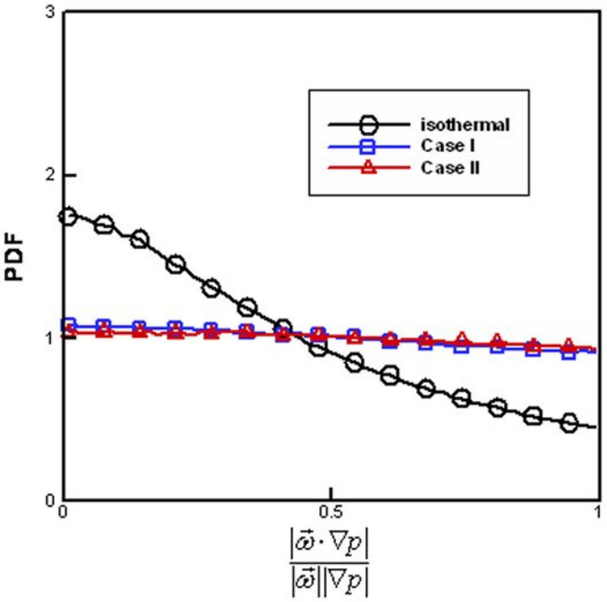

(c) Pressure gradient & vorticity

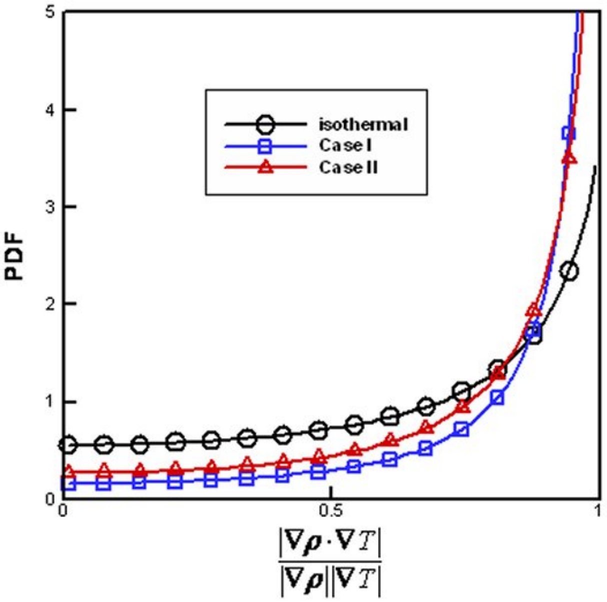

(d) Density & temperature gradient

Fig. 18. Continued

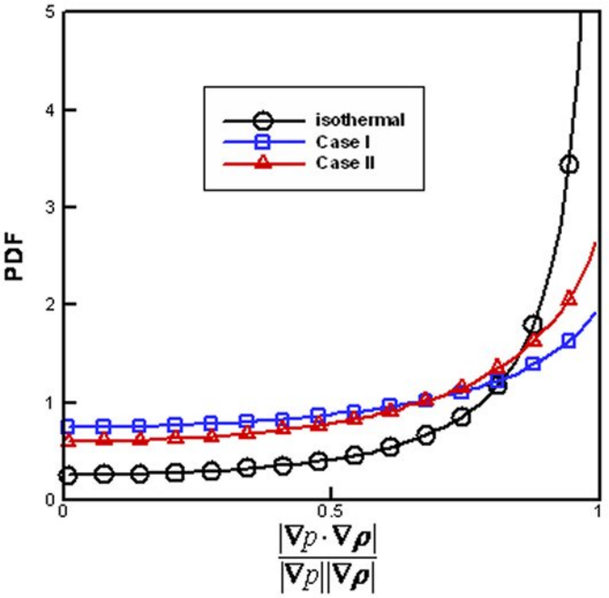

(e) Pressure & density gradient

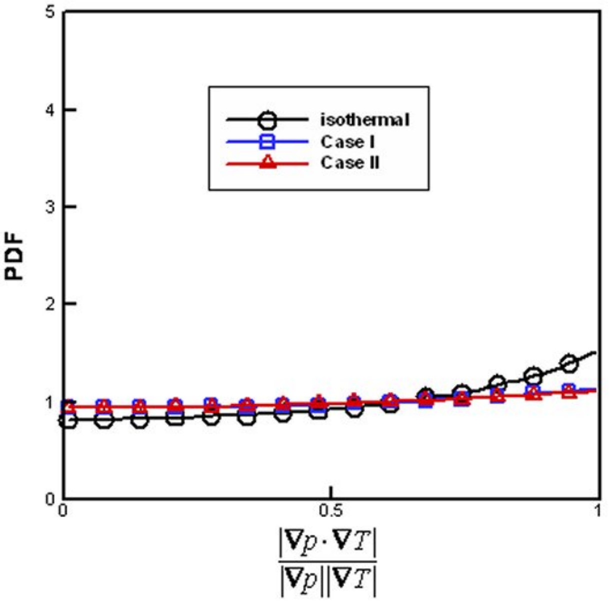

(f) Pressure & temperature gradient

Fig. 18. Continued

D. Conclusions

The hybrid thermal lattice Boltzmann method (HTLBM) is employed to simulate decaying compressible isotropic turbulence with imposed temperature fluctuations. The initial random velocity and temperature fields with different wave-number contents are generated. The numerical implementation is shown to conserve energy accurately and therefore is of high numerical fidelity.

The important findings are now summarized:

(1) The incompressible component of the velocity field appears unaffected by the presence of temperature fluctuations. However, the compressible component of the velocity field is profoundly affected by pressure work and dilatational dissipation (Fig. 11).

(2) Pressure work transfers energy back and forth between kinetic and thermal modes (Fig. 8(b), (c)). Over each transfer cycle, there is a small net flow of energy from the thermal to kinetic modes. This net transfer from the thermal to kinetic modes adds up to significant accumulation over the duration of the simulation (Fig. 11(b)). This energy is deposited in the large scales as dilatational velocity fluctuations (Fig. 10(b)). The large scale dilatational fluctuations then cascade to small scales. At the small scales, the kinetic energy is converted back to thermal energy via solenoidal and dilatational dissipation (Fig. 10(c), (d)). As this process proceeds, the initial large-scale thermal energy fluctuations are ultimately uniformly distributed over the flow domain by turbulence.

(3) The amplitude and length scale of the temperature fluctuations influence the time scale as well as the length scale of the pressure work (Fig. 8(b),(c) and Fig. 10(b)).

(4) The temporal velocity gradient (TVG) is enhanced due to the generation of

rapidly evolving dilatational velocity field in the presence of temperature fluctuations (Fig. 15(c)). However, this does not appear to affect the turbulence cascade, as the kinetic energy decays at the same rate as in the isothermal case.

(5) The alignments among vorticity vector and the gradients of pressure, density and temperature are altered by temperature fluctuations. Especially, the pressure gradient tends to be uncorrelated with the vorticity vector as well as with the density and temperature gradients in the presence of temperature fluctuations (Fig. 18(c), (e), and (f)).

This chapter shows that LBM can be a viable tool for simulating compressible turbulence with thermal field. However, the hybrid thermal LBM, in the current form, is limited to low Mach number flow. We will examine the small-scale structure at higher turbulent Mach numbers later in the dissertation.

CHAPTER V

RETURN-TO-ISOTROPY OF DECAYING ANISOTROPIC COMPRESSIBLE TURBULENCE IN THE PRESENCE OF TEMPERATURE FLUCTUATIONS

A. Introduction

Turbulence is a complicated three dimensional flow phenomenon encompassing a wide range of length and time scales. In general, turbulent energy is produced in the large scales by the action of mean velocity gradients. It is then redistributed among various Reynolds stress components by the action of pressure as it cascades down to small scales. At the final stage of the turbulence life-cycle, the turbulent kinetic energy dissipates into heat in small scales due to the action of molecular viscosity. Thus, fundamental knowledge of turbulent energy redistribution and its cascading properties is crucial for understanding turbulence physics. The simple case of return-to-isotropy of initially anisotropic decaying turbulence is an excellent venue for studying the non-linear redistributive action of pressure in isolation.

In compressible flows, the return-to-isotropy process is more complicated than in incompressible flows, due to the complications introduced by the activation of the thermal energy mode. In high speed flows (with high level of viscous heating) and flows with strong exothermic reactions, we can expect large temperature fluctuations and consequently, a great degree of thermal influence on fundamental turbulence processes such as return-to-isotropy. The goal of this study is to examine the return-to-isotropy process in an initially anisotropic turbulence field with imposed temperature fluctuations.

For incompressible turbulence, Rotta(1951) first proposed a linear model for return-to-isotropy: the rate of return-to-isotropy is linearly proportional to the degree of anisotropy [4]. Rotta's model has been used to represent slow pressure-strain correlation in numerous turbulence models and has been proven to predict many shear flows well. However, Rotta's model does not account for the correct energy redistribution when the flow field is strongly anisotropic. Furthermore, experiments show that the Rotta's constant depends on the type of flow field. In order to overcome this shortcoming of the linear model, Lumley and Newman [52] propose a model of return-to-isotropy that is a function of both the Reynolds number and the degree of anisotropy. Experiments by Gence and Mathieu [53], Choi and Lumley [54], and Le Penven *et al.* [55] show that return-to-isotropy is slower for the flow with a positive third invariant of anisotropy than the flow with a negative third invariant. Chung and Kim [56] reveal that return-to-isotropy depends on Reynolds number, and turbulence tends toward an axisymmetric state with a positive third invariant. Choi and Lumley [57] confirm that the turbulence first relaxes to an axisymmetric state as it ultimately tends toward an isotropic state. Further, it has been shown that the return-to-isotropy is much slower for turbulence with a greater third invariant of the anisotropy tensor. They also developed a turbulence model, which incorporates the effects of Reynolds number on the rate of return-to-isotropy. For more information about incompressible return-to-isotropy and its modeling, see [4].

There have been some important efforts to understand the return-to-isotropy of compressible turbulence. Sarkar *et al.* [18] analyze the compressible Navier-Stokes equation in low Mach-number asymptotic limit and find that the ratio between dilatational kinetic energy and fluctuating potential energy (root mean square of pressure fluctuations) exhibits interesting behavior with important modeling implications. Their work involves low-to-moderate turbulent Mach numbers and does not account for large temperature fluctuations typical of high enthalpy flows. Ristorcelli [58] decomposes the pressure dilatation and the dilatational dissipation into slow and rapid parts. He finds that the slow pressure dilatation scales with the square of turbulent Mach number, $\langle pd\rangle^s \sim M_t^2\varepsilon$, where M_t is the turbulent Mach number and ε is the dissipation rate, and the dilatational dissipation scales with $\frac{M_t^4}{R_t}$, where R_t is the turbulent Reynolds number, $R_t = \frac{4k^2}{9\varepsilon\nu}$. Crespo *et al.* [21] perform DNS with various anisotropic compressible fields and confirm that axisymmetric turbulence with a positive third invariant returns to isotropy slower than the case with a negative third invariant.

As mentioned earlier, the objective of this study is to examine the effects of large temperature fluctuations on the return-to-isotropy process. The initial anisotropic solenoidal velocity field is exposed to large temperature fluctuations which generate dilatational fluctuations. In the return-to-isotropy process, following questions are raised: How does the fluctuating internal energy affect the return-to-isotropy of solenoidal fluctuations? What are the features of dilatational fluctuations? (How does the dilatational kinetic energy scale? Is there equipartition between fluctuating internal energy and dilatational kinetic energy? Is the dilatational fluctuations anisotropic?) How much of fluctuating internal energy is converted to dilatational kinetic energy by pressure dilatation? Clearly, several factors influence the turbulence evolution and we identify three key parameters: turbulent Mach number, ratio of initial fluctuating internal energy to turbulent kinetic energy, and ratio of fluctuating to mean internal energy. We use the gas kinetic method (GKM) for our simulations. Details of the scheme were discussed in Chapter III.

B. Initial velocity field

To highlight the return-to-isotropy process, we start with a turbulence field that is initially entirely two componential. In other words, initially the kinetic energy is equally divided among two components of Reynolds stress and the third component is zero ($\langle u_1u_1\rangle = \langle u_2u_2\rangle = k\,;\ \langle u_3u_3\rangle = 0$). The fluctuations, although two-componential, can vary in all three directions. Such a fluctuation field is called a 2C3D initial field. The 2C3D axisymmetric solenoidal turbulence is obtained as follows:

Step (1): Generate a two-component velocity vector field ($\vec{u}$) in physical space using a random number generator, and set the third component to zero (third component can be assigned arbitrarily as determined at Step (4) to satisfy the incompressible condition and two-componentiality constraint).

Step (2): Transform the velocity field into Fourier space ($\vec{\hat{u}}$).

Step (3): Determine the solenoidal velocity amplitude from the solenoidal velocity condition:

$$\vec{\hat{u}}^{I} = \vec{\hat{u}} - \vec{\kappa}\,\frac{\vec{\kappa}\cdot\vec{\hat{u}}}{\kappa^2}\,, \tag{5.1}$$

where $\vec{\hat{u}}$ and $\vec{\kappa}$ denote the velocity amplitude vector and the wave number vector in Fourier space; $\vec{\hat{u}}^{I}$ is the projection vector of velocity amplitude perpendicular to the wave number vector, which is a purely incompressible turbulence field. This generates a non-zero third component, since $\vec{\kappa}(\vec{\kappa}\cdot\vec{\hat{u}})/\kappa^2$ yields a residual in the third direction. Thus, simply assigning zero to the third component in the physical space will not ensure a two-component axisymmetric field.

Step (4): To ensure two-componentiality, we enforce $\hat{u}^I_z = 0$ in Eq.(5.1). Then, we get the value of the third component amplitude ($\hat{u}_z$) in Fourier space, given the first two components ($\hat{u}_x$ and $\hat{u}_y$), as follows:

$$\hat{u}_z = \kappa_z \frac{\kappa_x\hat{u}_x + \kappa_y\hat{u}_y}{\kappa^2} \bigg/ \left(1 - \kappa_z\frac{\kappa_z}{\kappa^2}\right)\,. \tag{5.2}$$

When $\kappa^2 (= \kappa_x\kappa_x + \kappa_y\kappa_y + \kappa_z\kappa_z) = \kappa_z\kappa_z$, $\hat{u}_z$ is set to zero since any arbitrary value for $\hat{u}_z$ can satisfy the solenoidal condition.

Step (5): $\hat{u}_z$ as well as $\hat{u}_x$ and $\hat{u}_y$ are used to calculate solenoidal velocity amplitude fields from Eq.(5.1).

Step (6): To impose the required energy spectrum for the turbulence field, we use [46]

$$\vec{\hat{u}}^{I} = c\,\vec{\hat{u}}^{I}\sqrt{E(\kappa)}\,, \tag{5.3}$$

where

$$E(\kappa) = 0.057\kappa^4 e^{-0.14\kappa^2}\,. \tag{5.4}$$

In the above equations, κ is the magnitude of wave number vector ($\kappa = |\vec{\kappa}|$) and c is an arbitrary constant. The obtained velocity fields have zero value for the third component.

Step (7): By transforming the calculated amplitude vectors into the physical space, we obtain a solenoidal two-component three-dimensional (2C3D) axisymmetric turbulence field.

C. Simulation parameters

The simulation parameters are the turbulent Mach number M_t, the initial thermal fluctuation level T_r, and the ratio of initial fluctuating internal energy to turbulent kinetic energy ϕ, which are defined as

$$M_t = \frac{\sqrt{u^2}}{a}\,, \tag{5.5}$$

$$T_r = \frac{T'_{rms}(0)}{T_0}\,, \tag{5.6}$$

$$\phi = \frac{T'_{rms}(0)}{k_0}\,. \tag{5.7}$$

In the above definitions, $a = \sqrt{\gamma R T_0}$ is the speed of sound; T_0 is the mean of the initial temperature field; $T'_{rms}(0)$ is the root mean square value of the initial temperature fluctuations, $T - T_0$; and k_0 is the initial turbulent kinetic energy.

Table II. Cases for return-to-isotropy simulation

	$M_t(0)$		
	0.06	0.30	0.60
T_r	0.0	0.0	0.0
	0.0110	0.0275	0.0275
	0.0275	0.0688	0.1375
	0.0550	0.1375	0.2751
	0.1375	0.2751	-
	0.2751	-	-

All simulation cases are listed in Table II. The range of M_t is from 0.06 to 0.6 and the range of T_r is from 0.0 to 0.2751. The initial velocity field has a wave number range of 1 - 4 in a 128^3 computational domain. The initial temperature fluctuations are three-dimensional and isotropic. The initial mean temperature T_0 is $300K$ and the Prandtl number is 0.7 for all cases. The specific heat ratio γ and gas constant R are set to 1.4 and $287J/Kg \cdot K$ respectively. The dynamic viscosity μ is $4 \times 10^{-4} Kg/m \cdot s$, $2 \times 10^{-3} Kg/m \cdot s$, and $4 \times 10^{-3} Kg/m \cdot s$ for the initial turbulent Mach numbers of 0.06, 0.3, and 0.6 respectively. The initial Taylor-scale Reynolds number is set to 83.7 for all cases. The cell size and time step are set to $0.0002m$ and $1 \times 10^{-7}s$ respectively.

D. Results and discussion

1. Without temperature fluctuations

We first examine the effects of turbulent Mach number on Reynolds stresses in the absence of temperature fluctuations. The evolutions of Reynolds stress components at $M_t(0) = 0.06, 0.30,$ and 0.60 are plotted in Fig. 19. Initially, the third component $\langle u_3u_3\rangle$ is zero while the first two components, $\langle u_1u_1\rangle$ and $\langle u_2u_2\rangle$, are non-zero, which represents one extreme anisotropic flow condition. $\langle\cdots\rangle$ describes the density weighted average of Reynolds stress component over the computational domain. Here, we present only $\langle u_1u_1\rangle$ and $\langle u_3u_3\rangle$ since $\langle u_2u_2\rangle$ is statistically the same as $\langle u_1u_1\rangle$. The time is normalized by the initial eddy turnover frequency, $t' = t\frac{\varepsilon_0}{k_0}$.

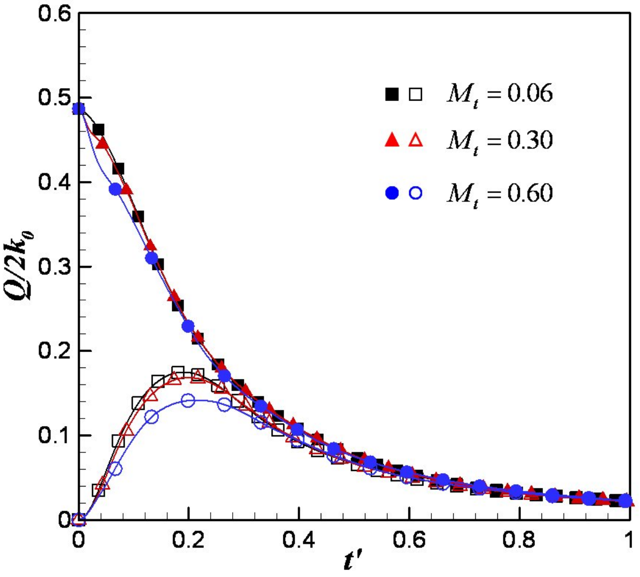

Fig. 19. Reynolds stress evolution in the absence of temperature fluctuations for different turbulent Mach numbers. $Q = \langle u_1u_1\rangle$ for solid symbol and $Q = \langle u_3u_3\rangle$ for open symbol.

In the case of $M_t(0) = 0.06$, Reynolds stress returns to isotropy state smoothly, and this corresponds to the return-to-isotropy of incompressible flows. In this case, the velocity fluctuations appear to be statistical isotropy beyond about 0.3 eddy turnover time. As the turbulent Mach number increases to 0.30 and 0.60, even though overall return-to-isotropy shows qualitatively the same feature as in the incompressible case ($M_t(0) = 0.06$), there appears a slight decrease in the Reynolds stress evolution, which is due to the energy subtraction from kinetic mode by pressure dilatation.

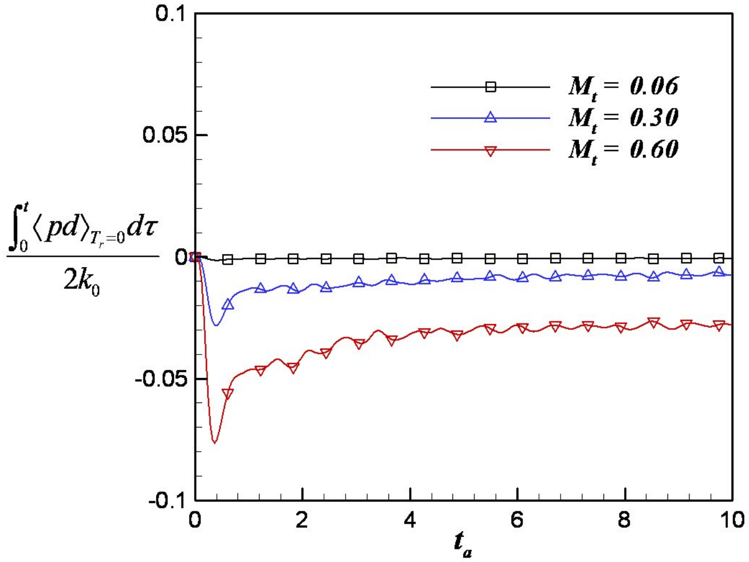

Fig. 20. Temporal integration of pressure dilatation for different turbulent Mach numbers in the absence of temperature fluctuations

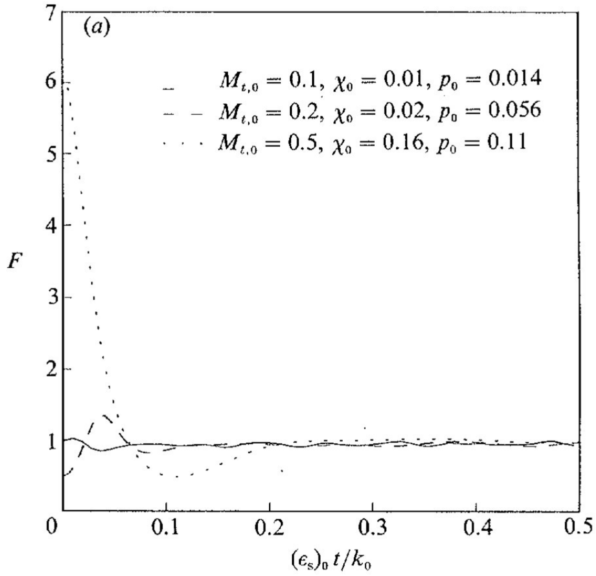

Fig. 21. Equipartition of compressible energy with various initial compressibility in the absence of fluctuating internal energy (Sarkar *et al.* [18])

The evolution of time integration of pressure dilatation is presented in Fig. 20. In the figure, the acoustic time is introduced as

$$t_a = t\frac{a}{l_0}\,, \tag{5.8}$$

where a is the speed of sound and l_0 is the characteristic length of the initial velocity field. The initial acoustic frequency, $\frac{a}{l_0}$, is $4.06 \times 10^4 s^{-1}$ for all cases. As seen in the figure, pressure dilatation is barely generated for the case with a turbulent Mach number of 0.06. As the turbulent Mach number increases to 0.3 and 0.6, the pressure dilatation decreases, which means that energy is transferred from the kinetic to internal modes.

In the absence of temperature fluctuations, Sarkar *et al.* [18] show the equipartition between fluctuating internal energy and dilatational kinetic energy from various initial compressibility flows (Fig. 21). Now we will investigate these issues in the presence of temperature fluctuations.

2. Return-to-isotropy with temperature fluctuations

Temperature fluctuations complicate the return-to-isotropy by introducing strong oscillatory behavior as seen in Fig. 22. Temperature fluctuations increase all Reynolds stress components. The increments of Reynolds stress are due to the dilatational field generated by temperature fluctuations (as shown later in this section). Despite the introduction of dilatational fluctuations, the time over which the flow field returns to isotropy is approximately the same as in the case without temperature fluctuations. In the high turbulent Mach number case ($M_t(0) = 0.60$), the increase of Reynolds stress is small as the initial fluctuating internal energy is small compared to the initial turbulent kinetic energy in this study. This suggests that the ratio of fluctuating internal energy to turbulent kinetic energy is an important parameter to measure the

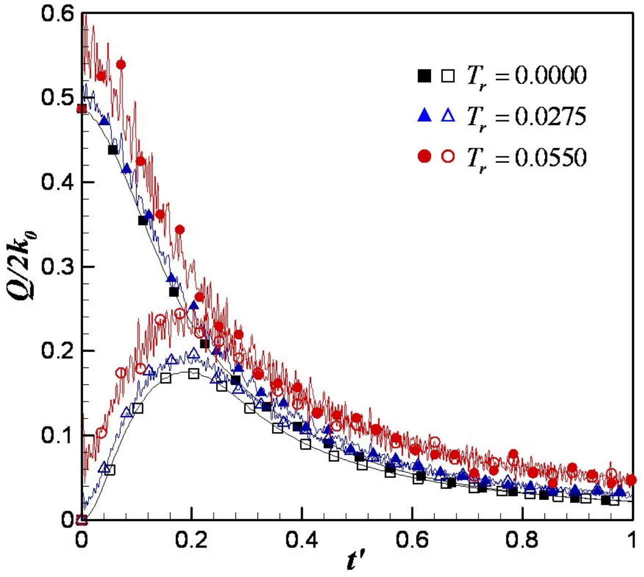

(a) $M_t(0) = 0.06$

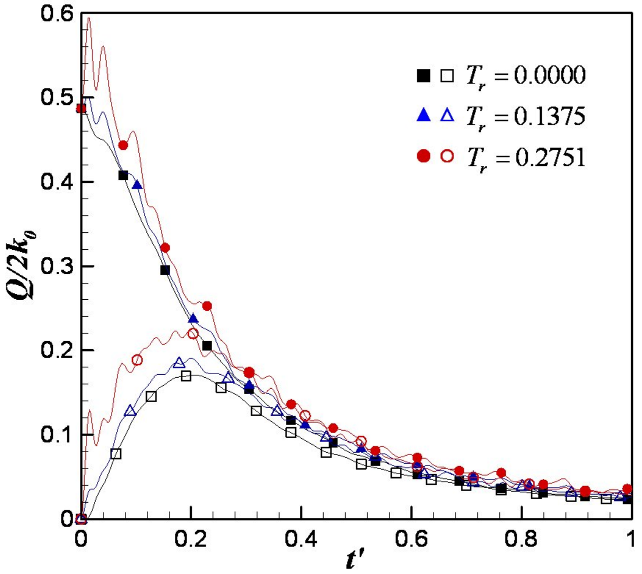

(b) $M_t(0) = 0.30$

Fig. 22. Reynolds stress evolution of total velocity field in eddy turnover time. $Q = \langle u_1 u_1 \rangle$ for solid symbol and $Q = \langle u_3 u_3 \rangle$ for open symbol.

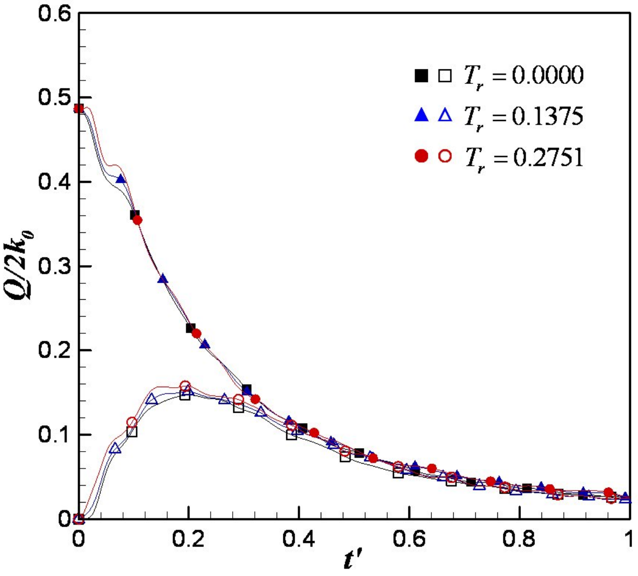

(c) $M_t(0) = 0.60$

Fig. 22. Continued

effect of thermal fluctuations on compressible turbulence.

a. Solenoidal velocity field

The next step is to decompose the velocity field into solenoidal and dilatational fluctuations. In each time step of simulations, the velocity field is decomposed in the Fourier space according to incompressible and compressible flow conditions. The evolution of Reynolds stresses of the solenoidal field is shown in Fig. 23. Regardless of the influence of the thermal field, the Reynolds stresses of the solenoidal field collapse well on that of the case without temperature fluctuations. For the turbulent Mach number range of 0.06 - 0.60, temperature fluctuations do not affect the return-to-isotropy of the solenoidal field. The inference is that the interactions between solenoidal and dilatational fluctuations are weak since temperature fluctuations provide only the dilatational motion and do not affect the return-to-isotropy of the solenoidal field.

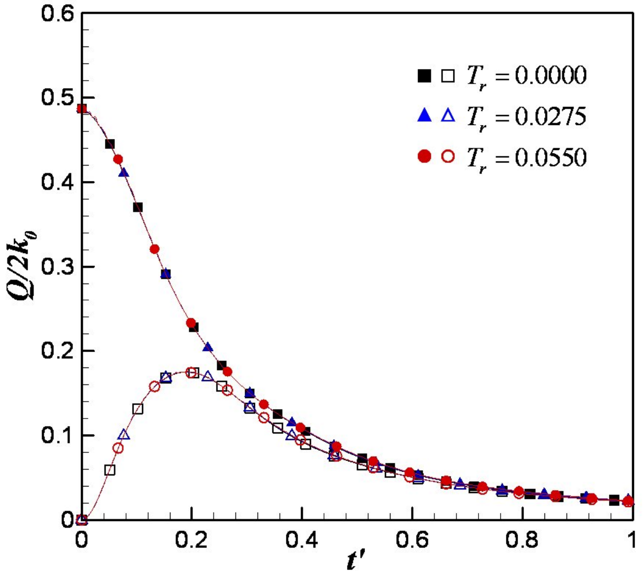

(a) $M_t(0) = 0.06$

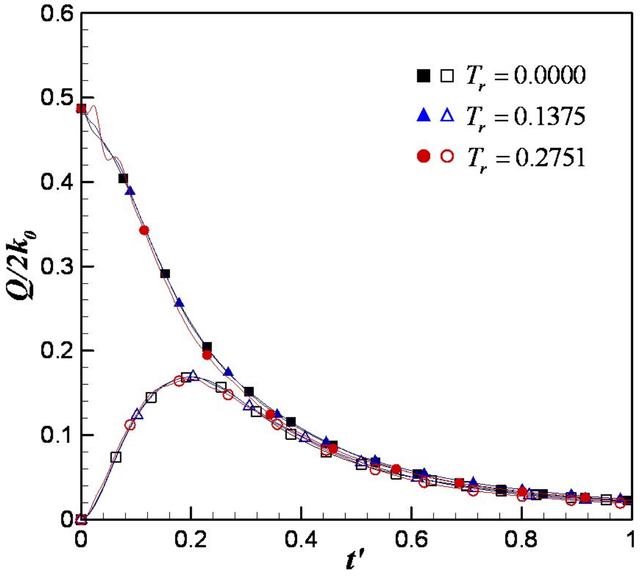

(b) $M_t(0) = 0.30$

Fig. 23. Reynolds stress evolution of solenoidal velocity field in eddy turnover time. $Q = \langle u_1 u_1 \rangle$ for solid symbol and $Q = \langle u_3 u_3 \rangle$ for open symbol.

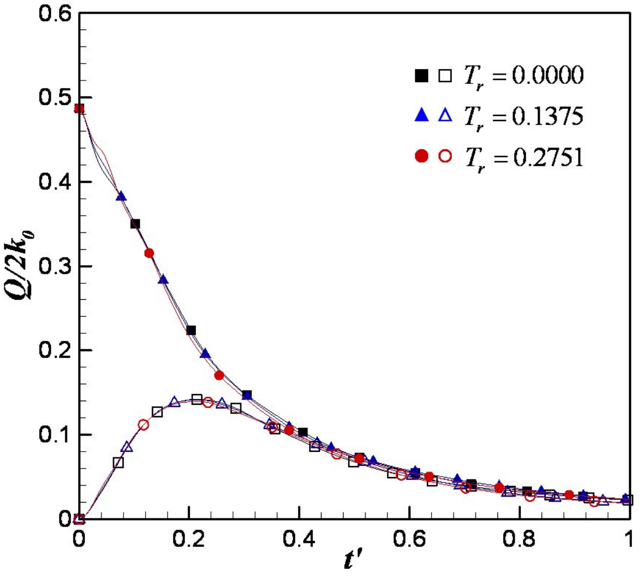

(c) $M_t(0) = 0.60$

Fig. 23. Continued

b. Dilatational velocity field

The evolution of the dilatational component of the Reynolds stress is shown in Fig. 24. Without temperature fluctuations, there are no dilatational components generated in low turbulent Mach number flows ($M_t(0) = 0.06$). However in high turbulent Mach numbers ($M_t(0) = 0.30,\ 0.60$), the dilatational field is generated since the initial solenoidal field is not balanced with thermodynamic variables.

The dilatational component of the Reynolds stress increases as temperature fluctuations increase. The increase in the dilatation component, while the solenoidal component keeps the same value, indicates that temperature fluctuations provide only dilatational motion in the flows. Interestingly, dilatational components of Reynolds stress do not react linearly to the magnitude of temperature fluctuations. Examining the case with $M_t(0) = 0.3$, for example, the facts become clear. When the temperature fluctuations of $T_r = 0.1375$ are applied, the initial response in dilatational Reynolds

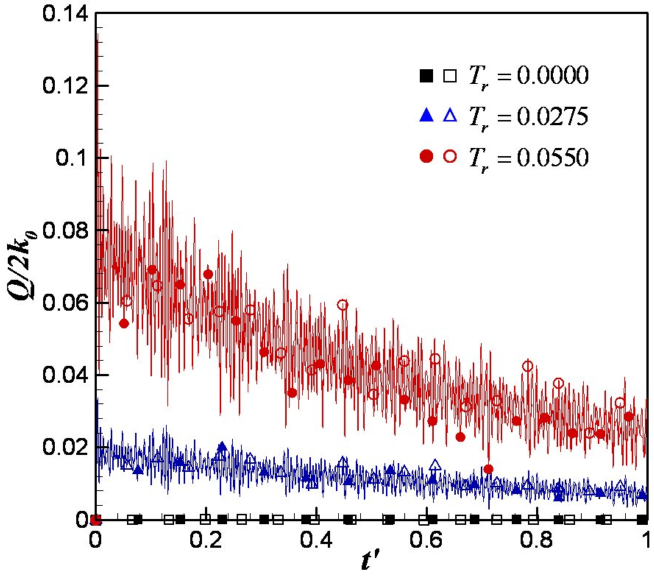

(a) $M_t(0) = 0.06$

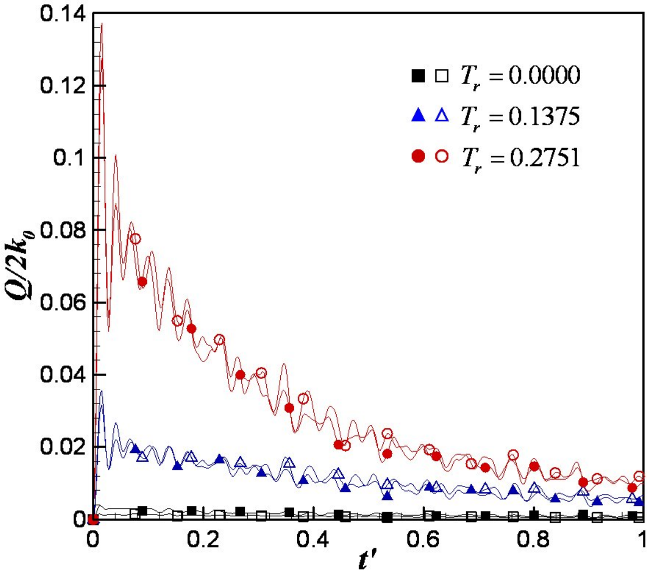

(b) $M_t(0) = 0.30$

Fig. 24. Reynolds stress evolution of dilatational velocity field in eddy turnover time. $Q = \langle u_1 u_1 \rangle$ for solid symbol and $Q = \langle u_3 u_3 \rangle$ for open symbol.

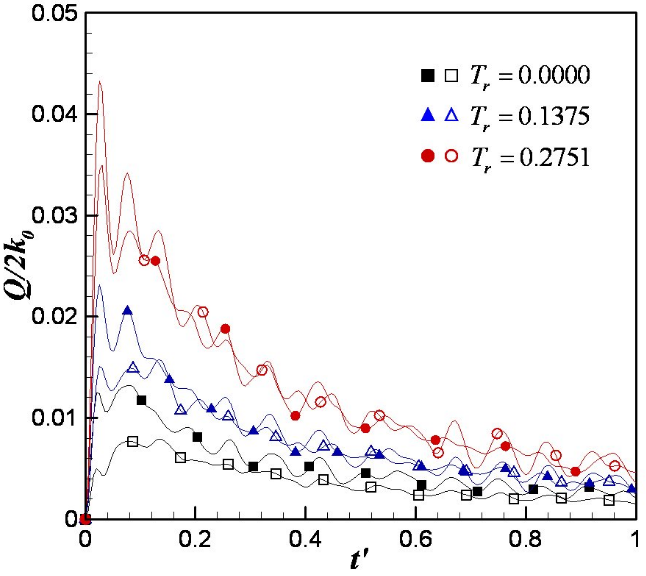

(c) $M_t(0) = 0.60$

Fig. 24. Continued

stress is around 0.02 on average. When temperature fluctuation increases two-fold ($T_r = 0.2751$), the initial Reynolds stress response goes up to 0.08. This means that there exists a quadratic relationship between dilatational kinetic energy and fluctuating internal energy. One may note that dilatational fluctuations are increased by almost an equal amount in all three directions by thermal fluctuations.

3. Pressure dilatation with temperature fluctuations

The role of pressure dilatation, in the absence of temperature fluctuations, is to transfer energy from kinetic to thermal modes. In the presence of temperature fluctuations, the pressure dilatation converts fluctuating internal energy into dilatational kinetic energy. Fig. 25 is the time integration of pressure dilatation for different turbulent Mach number and thermal fluctuation ratios. In the case with a turbulent Mach number of 0.06, with a small amount of thermal fluctuations ($T_r = 0.0275$), pressure

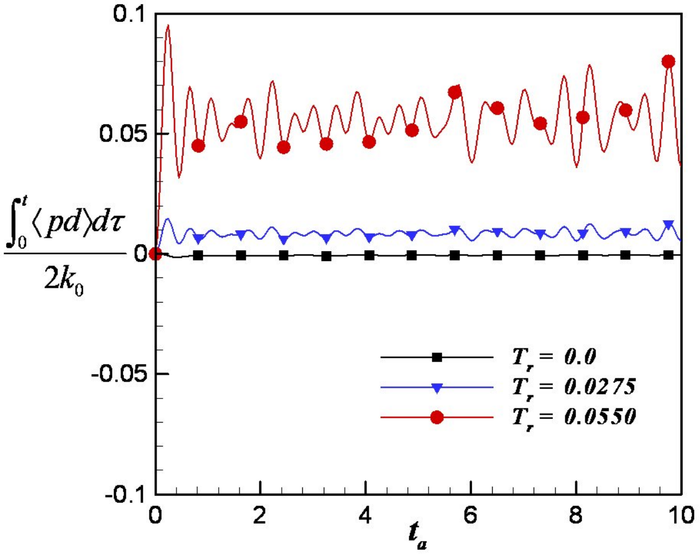

(a) $M_t(0) = 0.06$

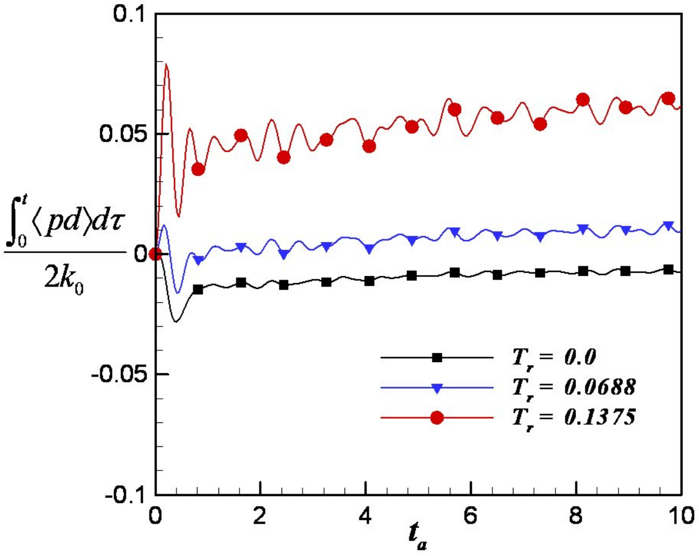

(b) $M_t(0) = 0.30$

Fig. 25. Temporal integration of pressure dilatation for different turbulent Mach numbers in the presence of temperature fluctuations

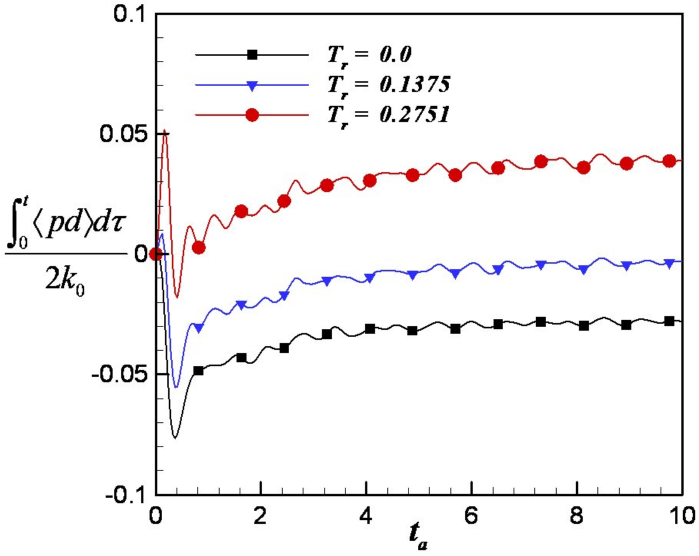

(c) $M_t(0) = 0.60$

Fig. 25. Continued

dilatation transfers energy from thermal to kinetic modes. However, at a turbulent Mach number of 0.6, with a large amount of thermal fluctuations ($T_r = 0.1375$), pressure dilatation still transfers energy from kinetic to thermal modes. In high turbulent Mach numbers, flow field has a large amount of dilatational kinetic energy, so that the pressure dilatation cannot convert fluctuating internal energy into dilatational kinetic energy. Thus, the ratio of fluctuating internal energy to kinetic energy is an important parameter to account for the thermal fluctuation effects in compressible flows.

4. Fluctuating internal vs. dilatational kinetic energy distribution

Compressible energy is known to be equilibrated between dilatational kinetic energy and fluctuating potential energy in the absence of temperature fluctuations [18]. Then, in the presence of temperature fluctuations, does the same equipartition exist

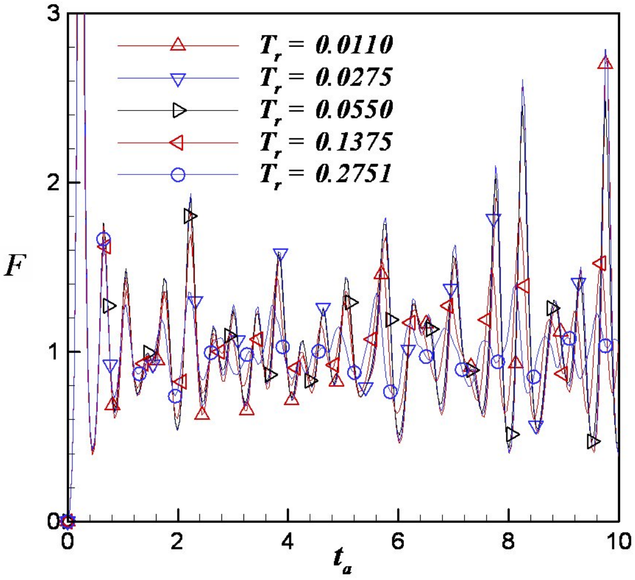

(a) $M_t(0) = 0.06$

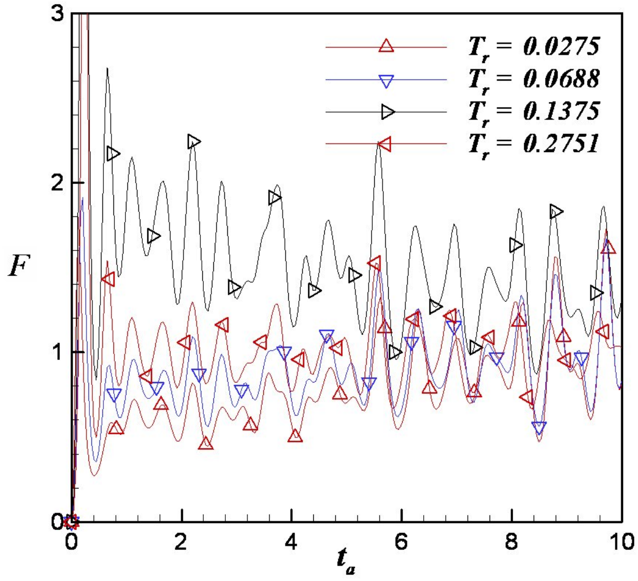

(b) $M_t(0) = 0.30$

Fig. 26. The evolution of F in acoustic time

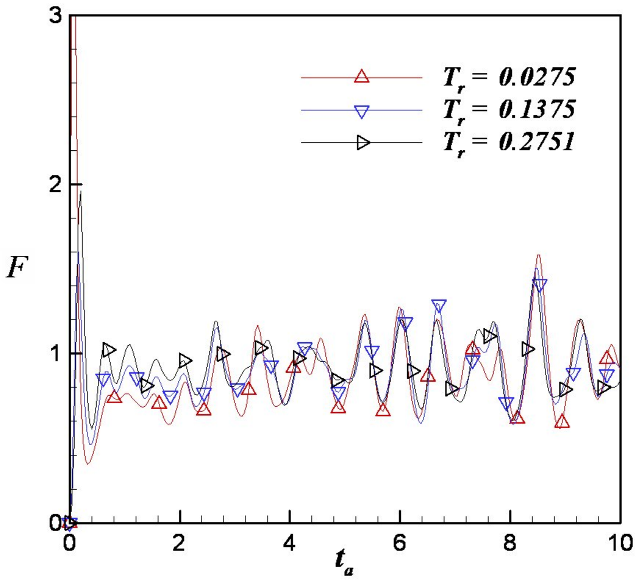

(c) $M_t(0) = 0.60$

Fig. 26. Continued

between fluctuating internal energy and dilatational kinetic energy? To identify the response of dilatational fluctuations to the fluctuating internal energy, we introduce a non-dimensional parameter, ratio of dilatational kinetic energy to the fluctuating pressure square, such that [18]

$$F = \frac{2k_d}{\overline{p_c'^2}} \overline{\rho} \gamma \overline{p} \,, \tag{5.9}$$

where k_d is dilatational kinetic energy; p_c' is the compressible component of pressure fluctuations; $\overline{\rho}$ is mean density; and $\overline{p}$ is mean pressure. Sarkar *et al.* [18] showed $F \simeq 1$ via an asymptotic analysis in low turbulent Mach numbers and DNS for $M_t < 0.5$. In Fig. 26, the non-dimensional parameter, F, is calculated in an acoustic time scale for the various thermal fluctuation levels in three different turbulent Mach numbers. In all cases, the equilibrium value, $F \simeq 1$, is obtained in an acoustic time scale. Thus, in the presence of temperature fluctuations, flow field achieves equipartition between fluctuating internal energy and dilatational kinetic energy.

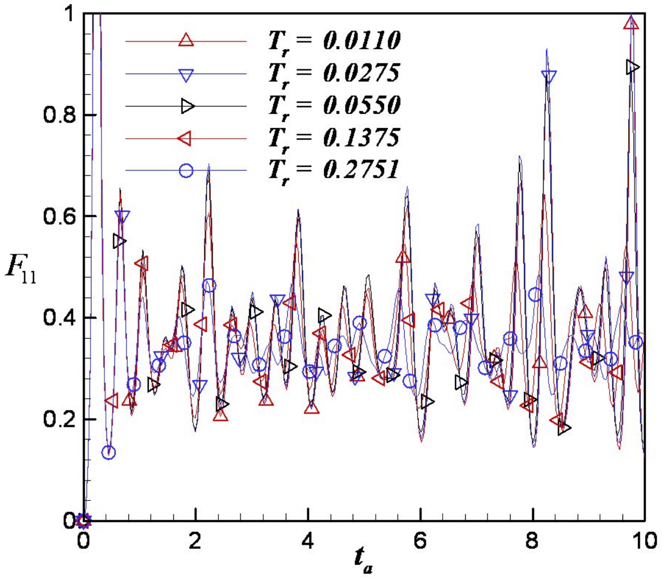

(a) $\langle u_1u_1\rangle$ component

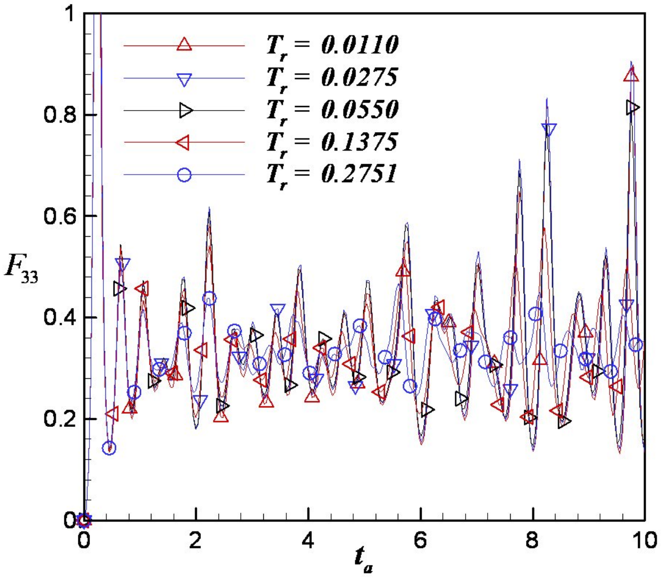

(b) $\langle u_3u_3\rangle$ component

Fig. 27. Dilatational field Reynolds stress normalized by the current pressure fluctuations at $M_t(0) = 0.06$

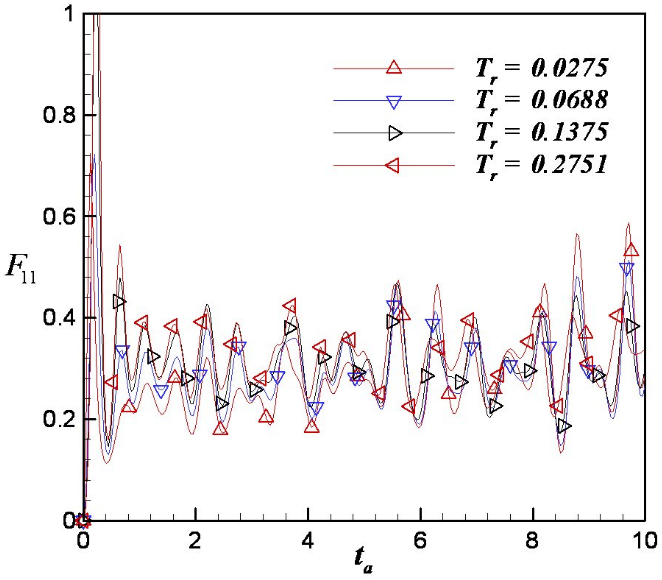

(a) $\langle u_1 u_1 \rangle$ component

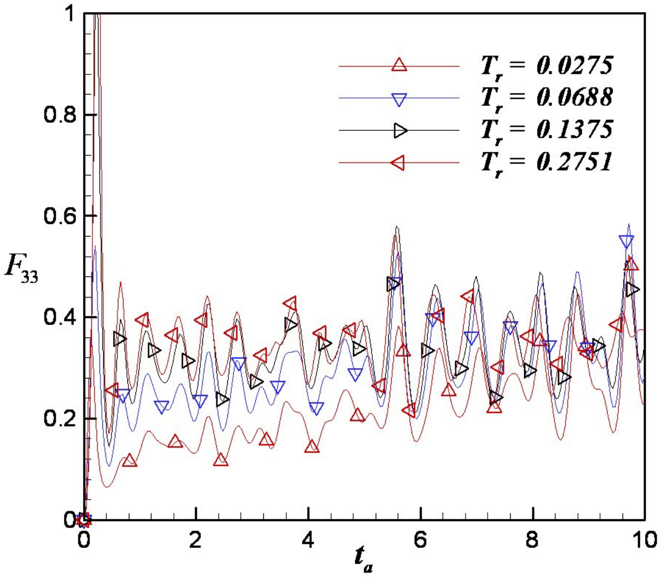

(b) $\langle u_3 u_3 \rangle$ component

Fig. 28. Dilatational field Reynolds stress normalized by the current pressure fluctuations at $M_t(0) = 0.30$

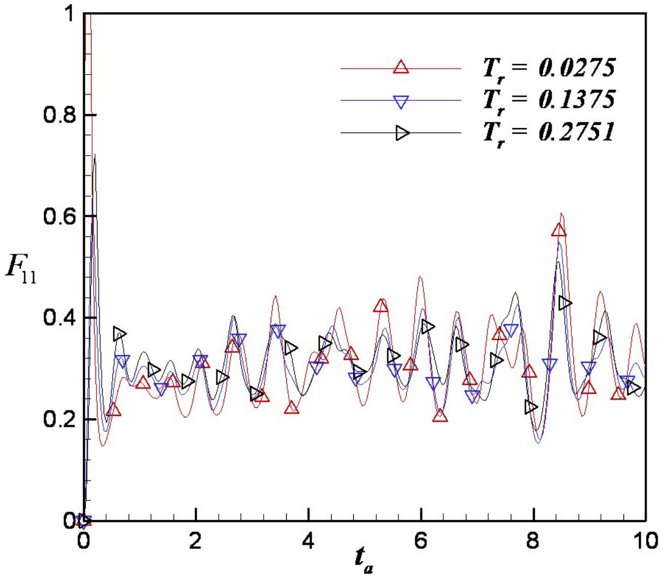

(a) $\langle u_1 u_1 \rangle$ component

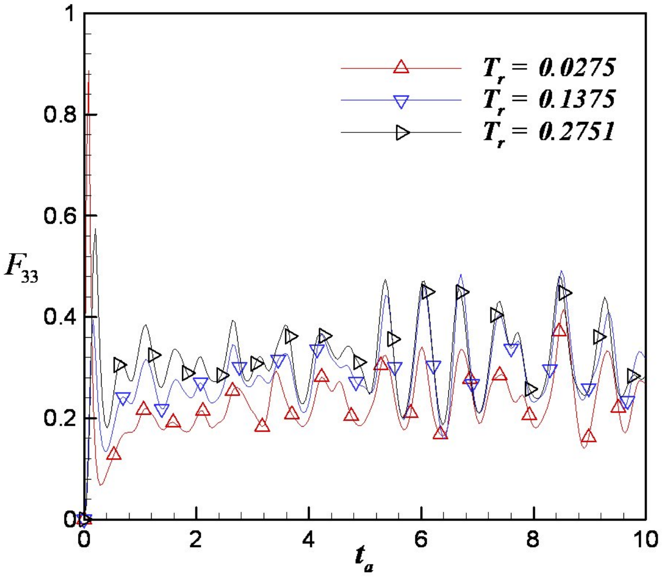

(b) $\langle u_3 u_3 \rangle$ component

Fig. 29. Dilatational field Reynolds stress normalized by the current pressure fluctuations at $M_t(0) = 0.60$

To study the effect of thermal fluctuations on each component of Reynolds stress, we introduce a non-dimensional parameter:

$$F_{ii} = \frac{\langle u_i u_i \rangle_d}{\overline{p_c'^2}} \overline{\rho} \gamma \overline{p}\,, \tag{5.10}$$

where $\langle u_i u_i \rangle_d$ is the dilatational component of Reynolds stress; $i = 1, 2, 3$; and the repeated subscript does not represent summation here. The evolution of F_{11} and F_{33} is plotted for different Mach numbers in Figs. 27, 28 and 29. The equilibrium state of each component, $F_{11} \approx F_{22} \approx F_{33} \approx \frac{1}{3}$, is obtained in all cases. This is another evidence that temperature fluctuations provide dilatational motion equally in all three directions and the resulting dilatational fluctuations are isotropic.

To quantify the response of the dilatational component of Reynolds stress, it is normalized with the initial pressure fluctuations. First, the dilatational component generated by the velocity field itself is subtracted in order to isolate the temperature fluctuation effect. Then the dilatational component of $\langle u_i u_i \rangle$ is normalized by the mean square of initial pressure fluctuations as follows:

$$\Delta F_{ii}^0 = \frac{\langle u_i u_i \rangle_{T_r} - \langle u_i u_i \rangle_{T_r=0}}{\overline{\left(p_c'(t=0)\right)^2}} \overline{\rho} \gamma \overline{p}\,, \tag{5.11}$$

where the subscripts, T_r and $T_r = 0$, represent the case with and without thermal fluctuations respectively. The repeated subscript does not represent summation here.

The evolution of ΔF_{11}^0 and ΔF_{33}^0 is plotted in Figs. 30, 31, and 32. The normalized dilatational components of Reynolds stress, ΔF_{11}^0 and ΔF_{33}^0, collapse well with the different thermal fluctuation cases at $M_t(0) = 0.06$ and $M_t(0) = 0.30$. This confirms that the initial response of dilatational motion can be scaled with the initial temperature fluctuation level. In high temperature fluctuation level ($T_r = 0.2751$), ΔF_{11}^0 and ΔF_{33}^0 start to deviate from the other cases in time. This deviation comes from dilatational dissipation, which is large in high temperature fluctuation cases

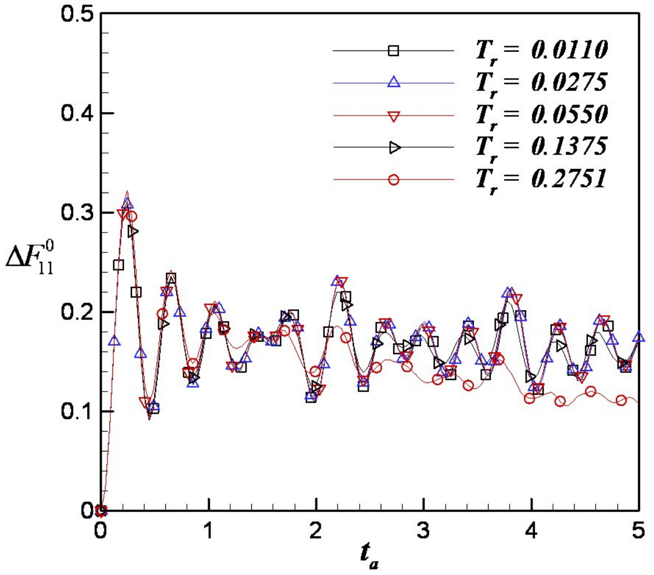

(a) $\langle u_1 u_1 \rangle$ component

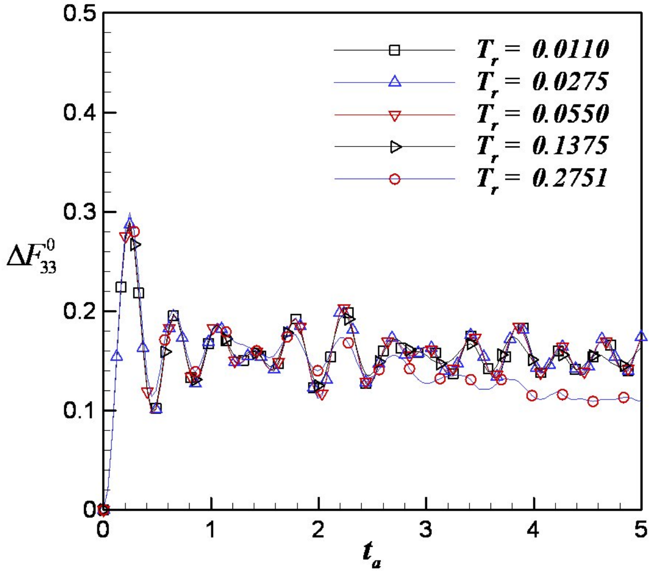

(b) $\langle u_3 u_3 \rangle$ component

Fig. 30. Dilatational field Reynolds stress normalized by the initial pressure fluctuations at $M_t(0) = 0.06$

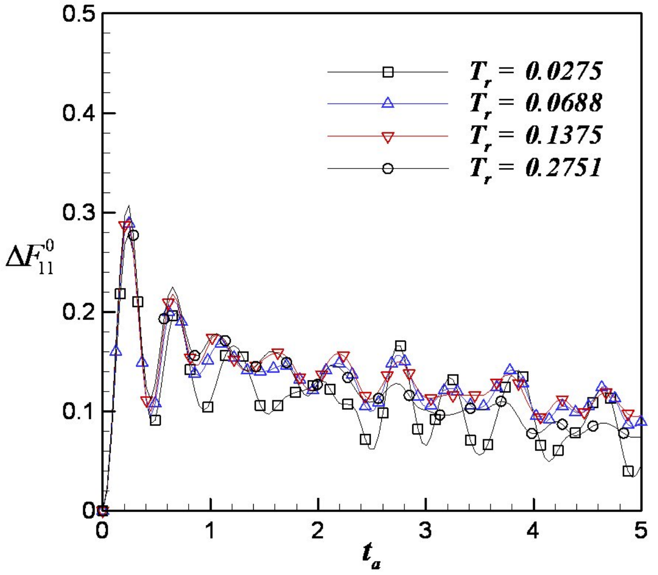

(a) $\langle u_1 u_1 \rangle$ component

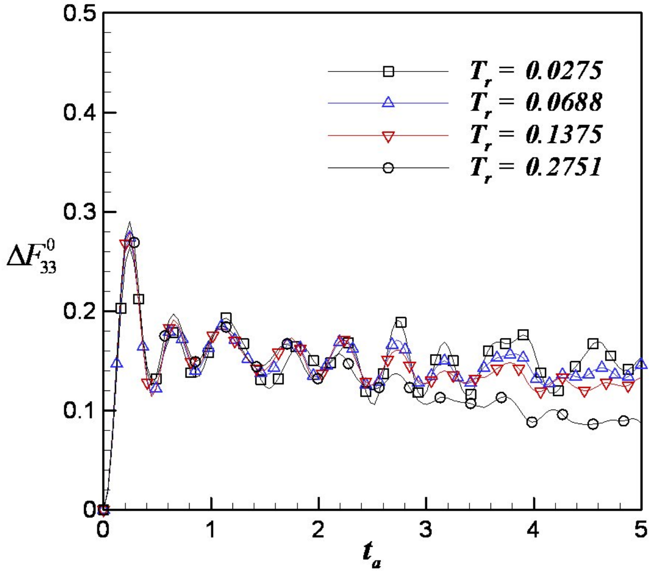

(b) $\langle u_3 u_3 \rangle$ component

Fig. 31. Dilatational field Reynolds stress normalized by the initial pressure fluctuations at $M_t(0) = 0.30$

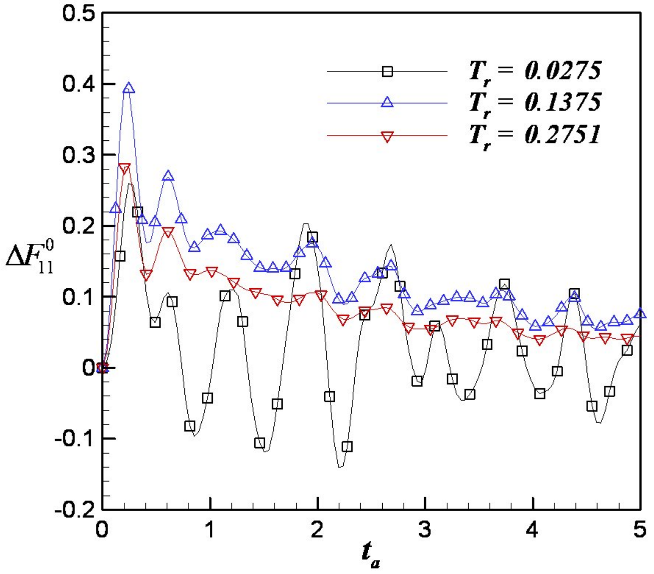

(a) $\langle u_1 u_1 \rangle$ component

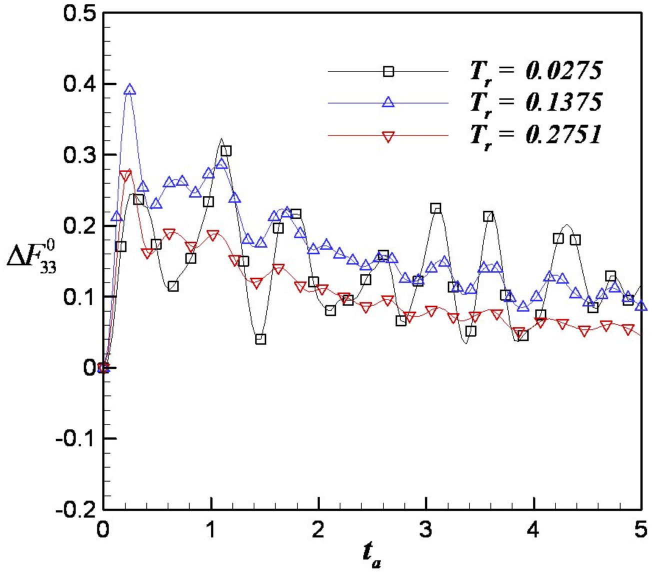

(b) $\langle u_3 u_3 \rangle$ component

Fig. 32. Dilatational field Reynolds stress normalized by the initial pressure fluctuations at $M_t(0) = 0.60$

and subtracts energy from kinetic to internal modes. This feature can be explicitly explained with the evolution of pressure dilatation later in this section. For a turbulent Mach number of 0.6, the amount of initial temperature fluctuations are small compared to the given turbulent kinetic energy. Thus the dilatational components of Reynolds stress have more saturation than the low turbulent Mach number cases due to the numerical truncation error. It should be noted that even for different turbulent Mach numbers, ΔF_{11}^0 and ΔF_{33}^0 tend to have a universal value.

Dilatational fluctuations are generated via pressure dilatation. In general, in the presence of temperature fluctuations, pressure dilatation converts the fluctuating internal energy into dilatational kinetic energy. To identify the amount of energy transferred, we introduce a non-dimensional parameter, ΔG^0, which describes the ratio of the time integral value of the pressure dilatation to the initial pressure fluctuations as follows:

$$\Delta G^0 = \frac{\int_0^t \left(\langle pd \rangle_{T_r} - \langle pd \rangle_{T_r=0} \right) d\tau}{\overline{\left(p_c'(t=0)\right)^2}} \overline{\rho} \gamma \overline{p} \,, \tag{5.12}$$

where $\langle pd \rangle$ represents the domain average of pressure dilatation. Figs. 33, 34 and 35 show the evolution of ΔG^0 for various turbulent Mach numbers and thermal fluctuation levels. Interestingly, ΔG^0 converges to a constant value for each turbulent Mach number. This confirms that the pressure dilatation scales with the mean square of initial fluctuating pressure. In our study, the initial fluctuating pressure comes from the temperature fluctuations. Thus, there exists a similar scaling between the integral of pressure dilatation and temperature fluctuations as well. Combined with dilatational dissipation, the pressure dilatation determines the amount of dilatational fluctuations in the flows.

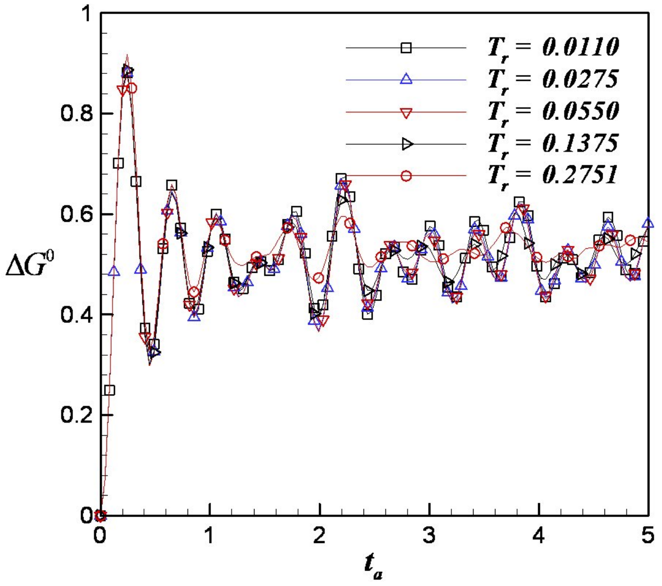

(a) At early times

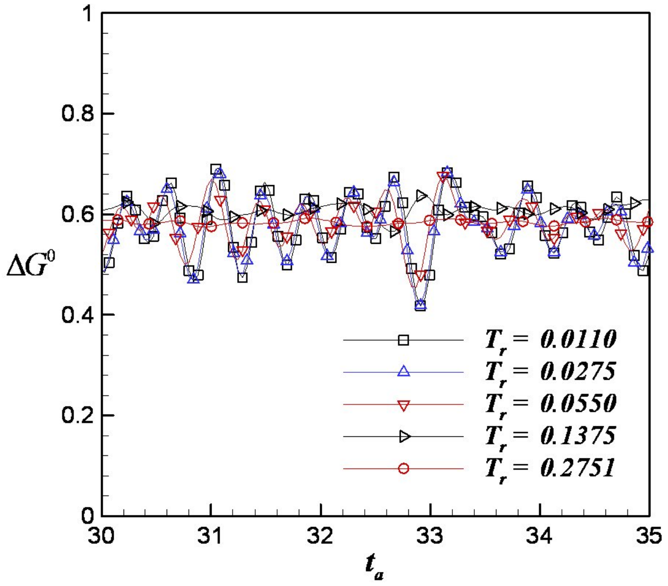

(b) At later times

Fig. 33. Integrated pressure dilatation normalized by the initial pressure fluctuations at $M_t(0) = 0.06$

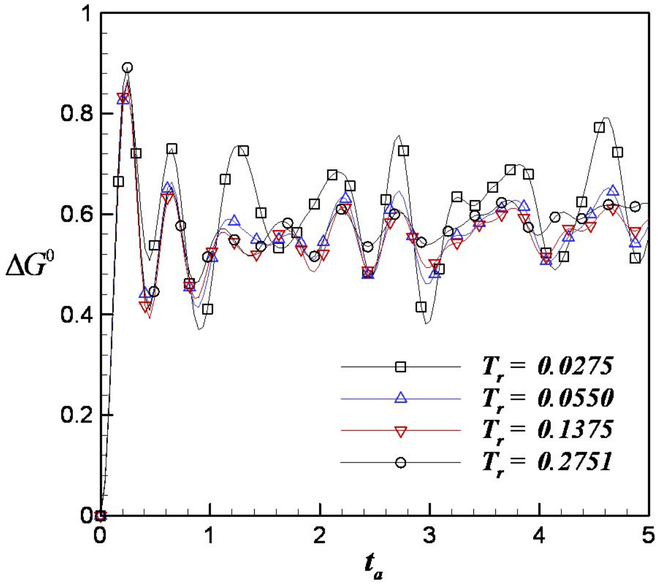

(a) At early times

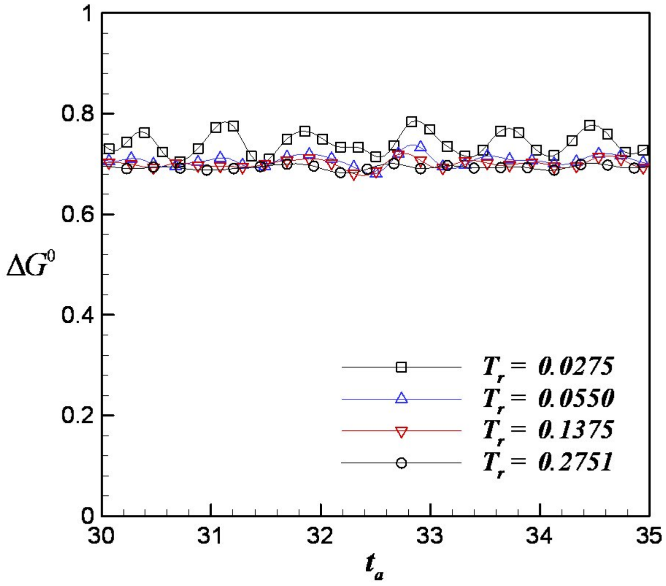

(b) At later times

Fig. 34. Integrated pressure dilatation normalized by the initial pressure fluctuations at $M_t(0) = 0.30$

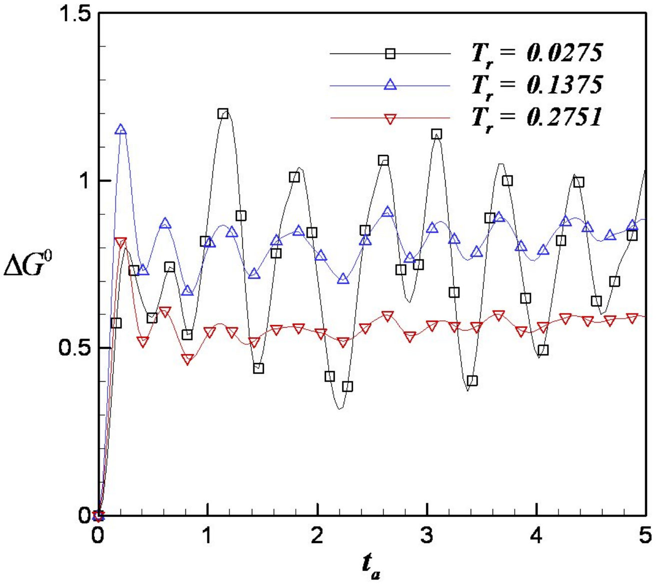

(a) At early times

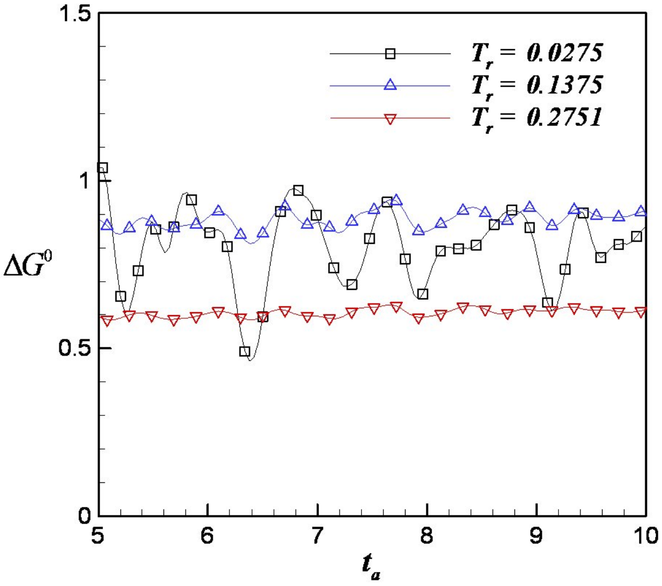

(b) At later times

Fig. 35. Integrated pressure dilatation normalized by the initial pressure fluctuations at $M_t(0) = 0.60$

E. Conclusions

Direct numerical simulations of decaying anisotropic compressible turbulence are performed using the Boltzmann BGK equation based gas kinetic method (GKM). The initial anisotropic velocity field is generated satisfying the incompressible flow conditions in Fourier space, but it has high amplitude fluctuations, facilitating high turbulent Mach number flows. Further, three dimensional isotropic temperature fluctuations are applied to study the thermal effects on the return-to-isotropy of Reynolds stress. The important findings are:

(1) Temperature fluctuations provide only dilatational motion in the flows: equal amounts of kinetic energy are added into all three components of Reynolds stress. In the absence of temperature fluctuations, pressure dilatation transfers energy from kinetic and thermal modes and the amount of energy transfer increases as turbulent Mach number increases. In the presence of temperature fluctuations, pressure dilatation tends to transfer energy from thermal to kinetic mode but it depends on the ratio of fluctuating internal energy to dilatational kinetic energy.

(2) Heat release does not change the Reynolds stress evolution of solenoidal field for the turbulent Mach number range of 0.06 - 0.6 and the thermal fluctuation level up to 0.27. The interactions between the dilatational and solenoidal fluctuations are negligible for the same range of turbulent Mach numbers and thermal fluctuation levels.

(3) Equipartition of the initial fluctuating internal energy is achieved in an acoustic time scale. Dilatational kinetic energy scales with the mean square of fluctuating pressure in the presence of thermal fluctuations. Isotropic temperature fluctuations generate isotropic dilatational fluctuations.

(4) The energy deposited by pressure dilatation is proportional to the mean

square of the initial fluctuating pressure, which leads to a similar relationship between dilatational kinetic energy and fluctuating internal energy at early times. The dilatational dissipation removes energy from the dilatational motion and the relationship weakens.

CHAPTER VI

EFFECT OF COMPRESSIBILITY ON TURBULENT VELOCITY GRADIENTS AND SMALL-SCALE STRUCTURE

A. Introduction

Velocity gradient dynamics and small-scale structure hold the key to understanding many important turbulence processes such as cascade dynamics, scalar mixing, material element deformation and intermittency. The alignment between vorticity and strain-rate eigenvectors determines the extent of vortex stretching which is a crucial element of cascade dynamics. It is also well known that scalar gradients align with the most compressive strain-rate eigenvector. Material line elements tend to align along the most extensive strain-rate eigen direction.

In incompressible turbulence, Ashurst *et al.* [59] examine the probability of alignment between vorticity and strain-rate eigenvectors and the distribution of strain-rate eigenvalues. They find that the vorticity preferentially aligns with an intermediate strain-rate eigenvector and the most probable strain-rate eigenvalues are of ratio $3:1:-4$, which means that flow structures are generally sheet-like. The small-scale vortex structure is first visualized from direct numerical simulations (DNS) of isotropic incompressible turbulence by She *et al.* [60]. They find that strongest vortex structures are intermittent and typically tube-like, and moderate amplitude vortex structures are sheet-like. Kalelkar [61] investigates the orientation among vorticity, velocity, pressure gradient, strain-rate eigenvectors, and eigenvectors of pressure Hessian tensor.

Erlebacher and Sarkar [20] study the velocity gradient structure in compressible homogeneous shear turbulence. They find that the solenoidal part of strain rate has the same distribution of eigenvalues $(3 : 1 : -4)$ as in incompressible turbulence. However, the distribution of dilatational strain-rate eigenvalues is quite different. In the regions of strong dilatation, the flow forms a sheet-like structure on the plane perpendicular to the shear. Kosovic *et al.* [62] perform large eddy simulations of compressible turbulence and study various statistics including alignment of vorticity with strain-rate eigenvectors at a turbulent Mach number of 0.4 and find no significant changes from incompressible turbulence.

Compressible flow velocity-gradient studies undertaken so far show little change in flow structure from incompressible results due to two important factors: (i) at the turbulent Mach number levels considered, dilatational component of fluctuations is quite small; and (ii) the effects of positive and negative dilatations could possibly be opposite of one another, leaving the most probable behavior nearly unchanged. Therefore, the best manner to assess the effects of compressibility is to examine the velocity gradient dynamics and small-scale structure conditioned on a given value of dilatation. We demonstrate that, irrespective of the Mach number of the flow, the velocity-gradient structure conditioned on a given value of normalized dilatation is statistically nearly self-similar. The role of the Mach number is merely to modify the intensity and distribution of dilatation.

The objective of this chapter is to investigate the velocity-gradient structure conditioned on different dilatation levels. The dilatation effects on velocity gradients are examined using DNS of decaying isotropic turbuelnce at various Mach numbers. The gas kinetic method (GKM) detailed in Chapter III is employed for the simulations.

The remainder of the chapter is organized as follows. In Section B, the parameters of the various simulations are given. In Section C, we investigate the effects of turbulent Mach number and Reynolds number on velocity gradients. In Section D, the velocity gradient behavior conditioned on dilatation level is examined. Summary and conclusions are presented in Section E.

B. Simulation parameters

The most important simulation parameters are the Taylor-scale Reynolds number and the turbulent Mach number, which are defined as

$$Re_\lambda = \sqrt{\frac{20}{3\varepsilon\nu}}k\,, \tag{6.1}$$

$$M_t = \frac{\sqrt{u^2}}{a}\,, \tag{6.2}$$

where $a = \sqrt{\gamma RT}$ is the speed of sound; k is turbulent kinetic energy; ε is the turbulent energy dissipation rate; and ν is kinematic viscosity. All simulation cases considered in this study are listed in Table III. The initial turbulent Mach number ranges from 0.059 to 0.885 and the initial Taylor-scale Reynolds number is set to 55.6 and 110.5. The computational domain is a 256^3 box and periodic boundary condition is applied in all directions. The wave number contents of the initial velocity field is in the range $\kappa(0) = 1 \sim 8$. The initial density and temperature are set to constant values of $\rho_0 = 1.0Kg/m^3$ and $T_0 = 300K$ respectively. The grid size and time step are set to $\Delta x = 1.0 \times 10^{-4}m$ and $\Delta t = 2.0 \times 10^{-8}s$. The gas constant, specific heat ratio, and Prandtl number are $R = 287J/Kg \cdot K$, $Pr = 0.7$, and $\gamma = 1.4$ respectively.

Table III. Simulation cases for decaying isotropic compressible turbulence

Simulation cases	Case 1	Case 2	Case 3	Case 4	Case 5
$Re_\lambda(0)$	55.6	55.6	55.6	55.6	110.5
$M_t(0)$	0.059	0.413	0.708	0.885	0.708
$\mu \times 10^{-4}[Kg/m \cdot s]$	4	28	48	60	24

To analyze the small-scale structure of the flow, from each simulation, we output

Table IV. Measured flow fields in each simulation

Simulation case	$t\frac{\varepsilon_0}{k_0}$	M_t	Re_λ
Case 1	0.1967	0.05	31.7
	0.3934	0.04	23.1
Case 2	0.1945	0.35	31.7
	0.3890	0.28	23.4
Case 3	0.1666	0.61	31.8
	0.3332	0.50	24.7
Case 4	0.1389	0.78	31.2
	0.2778	0.66	25.2
Case 5	0.1319	0.60	49.4
	0.2638	0.46	35.0

full velocity fields at two different times, one at the dissipation peak (highest level of non-linearity) and the other at a later stage when viscous effects have set in. Table IV identifies the normalized time and corresponding Reynolds and Mach numbers at which the flow field is examined. Using the total velocity field, various turbulence small-scale features are computed.

C. Effect of turbulent Mach number and Reynolds number

The evolution of turbulent kinetic energy and dissipation rate are shown in Figs. 36 and 37. For a given Reynolds number, $Re_\lambda(0) = 55.6$, the evolution of kinetic energy and dissipation rate do not show significant differences for four different turbulent Mach numbers. The dependence on Reynolds number is, however, evident as in incompressible turbulence.

We next investigate the strain-rate eigenvalue distribution at different Reynolds

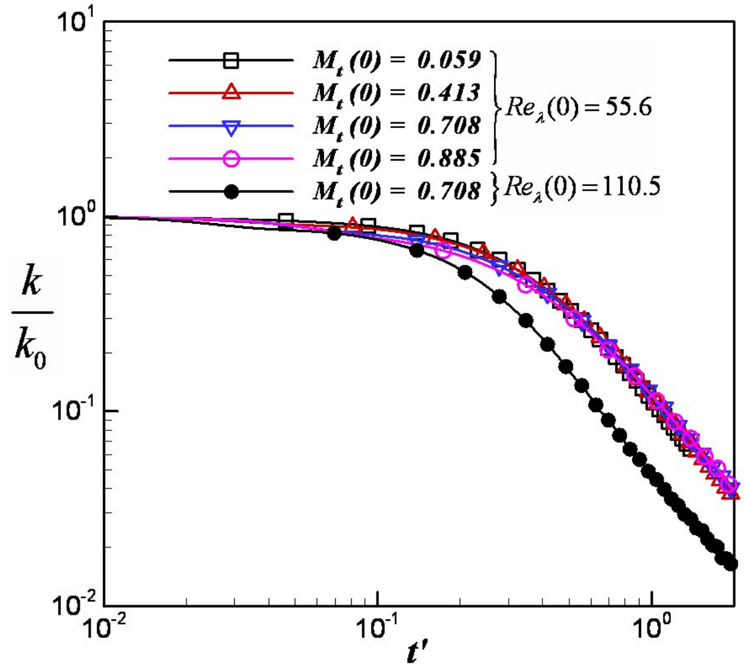

Fig. 36. Kinetic energy evolution for different turbulent Mach numbers and Reynolds numbers

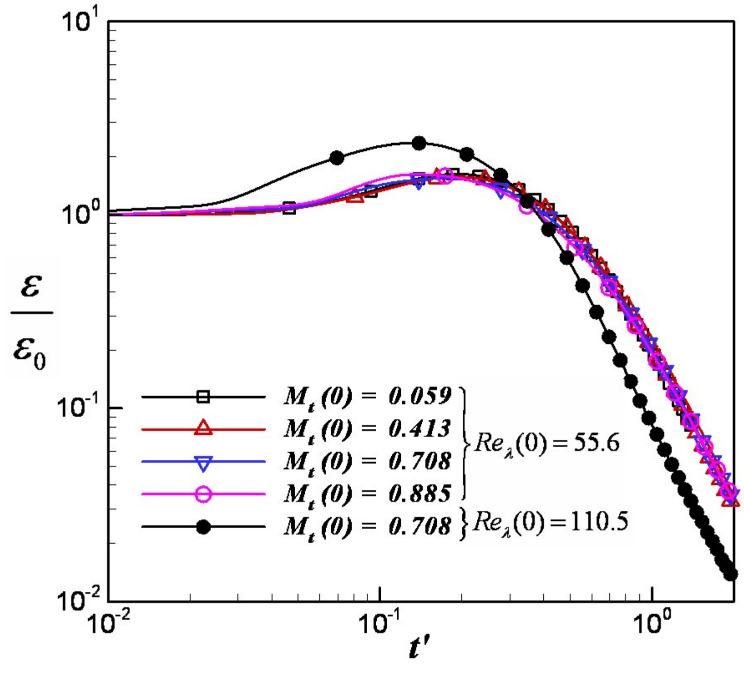

Fig. 37. Dissipation rate for different turbulent Mach numbers and Reynolds numbers

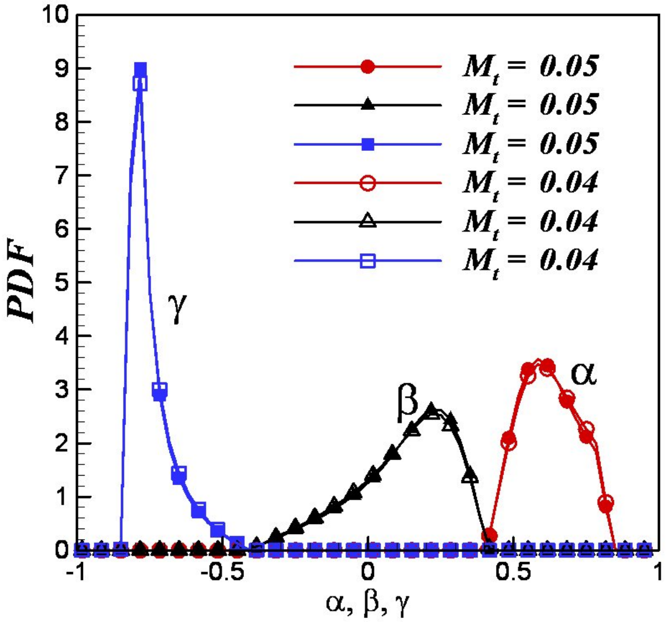

(a) $M_t(0) = 0.059$

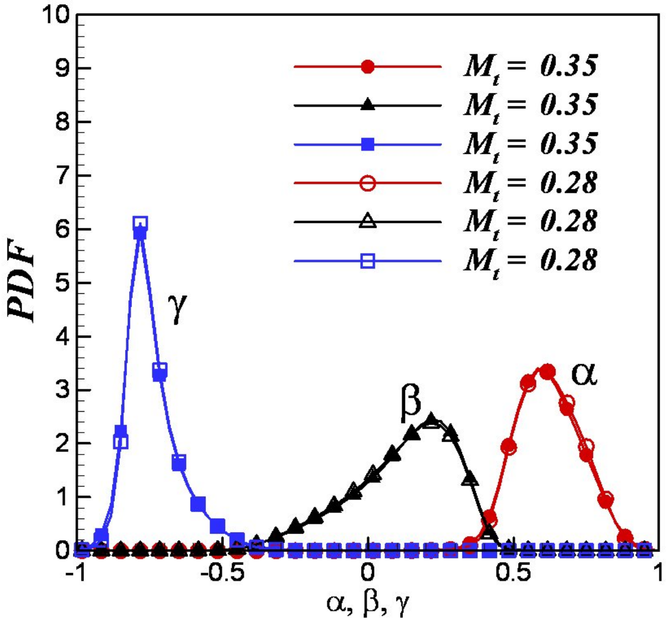

(b) $M_t(0) = 0.413$

Fig. 38. Strain-rate eigenvalues at different turbulent Mach numbers ($Re_\lambda(0) = 55.6$)

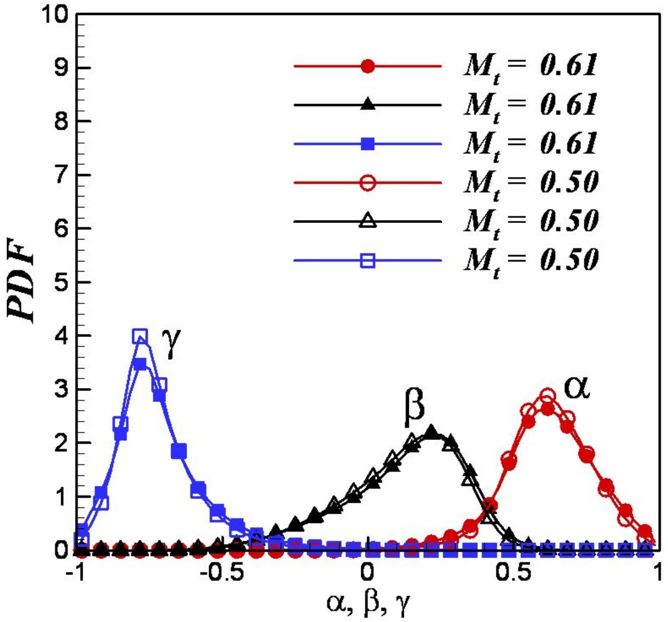

(c) $M_t(0) = 0.708$

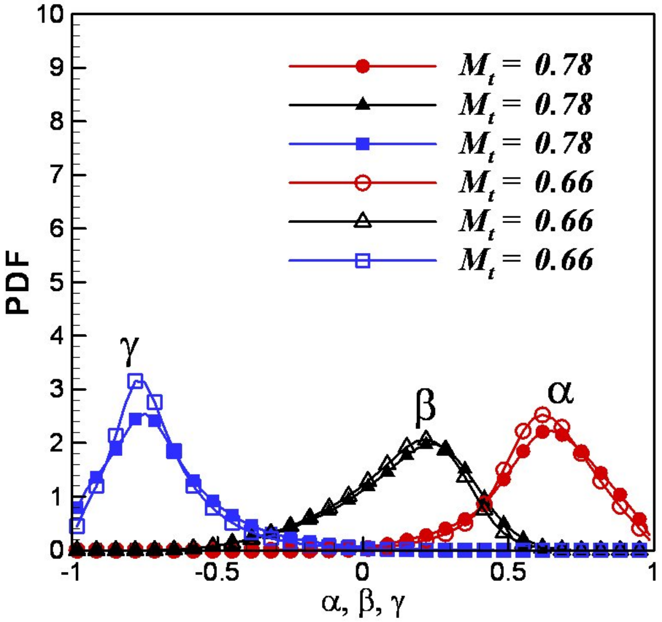

(d) $M_t(0) = 0.885$

Fig. 38. Continued

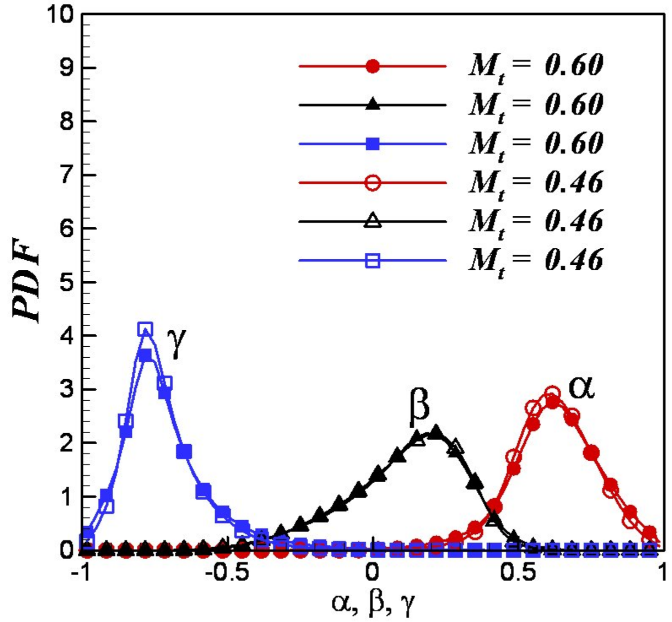

Fig. 39. Strain-rate eigenvalues in higher Reynolds number flows ($Re_\lambda(0) = 110.5$, $M_t(0) = 0.708$)

and Mach numbers. The strain-rate eigenvalues indicate the nature of self-straining of small-scale turbulence [63]. The strain-rate tensor magnitude is important since it represents the rate of turbulent energy cascade and the tendency toward intermittency. In Fig. 38, the distributions of eigenvalues are plotted for four cases in $Re_\lambda(0) = 55.6$. The eigenvalues are normalized with the root-mean square of all eigenvalues. For the case with a turbulent Mach number of 0.059 (Fig. 38(a)), the distribution of eigenvalues is nearly the same as in incompressible turbulence (see [59]). The eigenvalues are distributed widely for high turbulent Mach numbers (Figs. 38(b), 38(c) and 38(d)), while the probabilities of eigenvalues' peak are decreased. However, the most probable eigenvalues do not seem to change at high turbulent Mach numbers. The Reynolds number effects on the eigenvalue distribution are studied in Fig. 38(c) and Fig. 39. The statistics of strain-rate eigenvalues does not depend on the Reynolds number for $Re_\lambda = 55.6 - 110.5$.

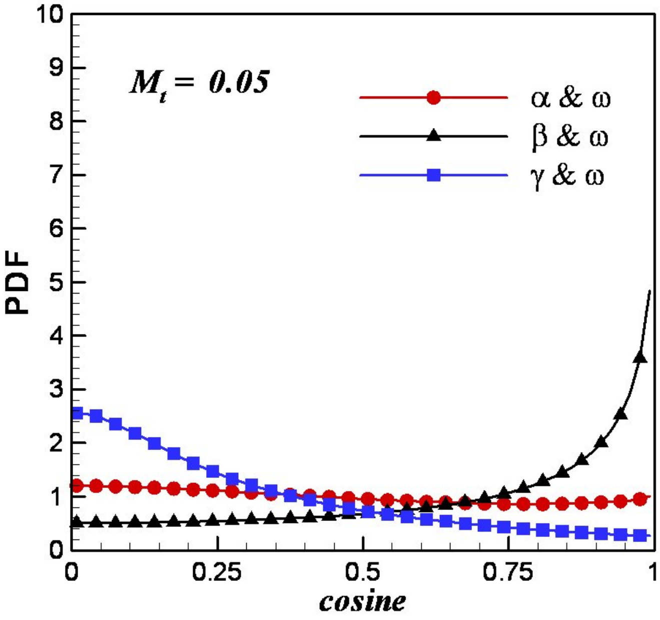

(a) $M_t(0) = 0.059$

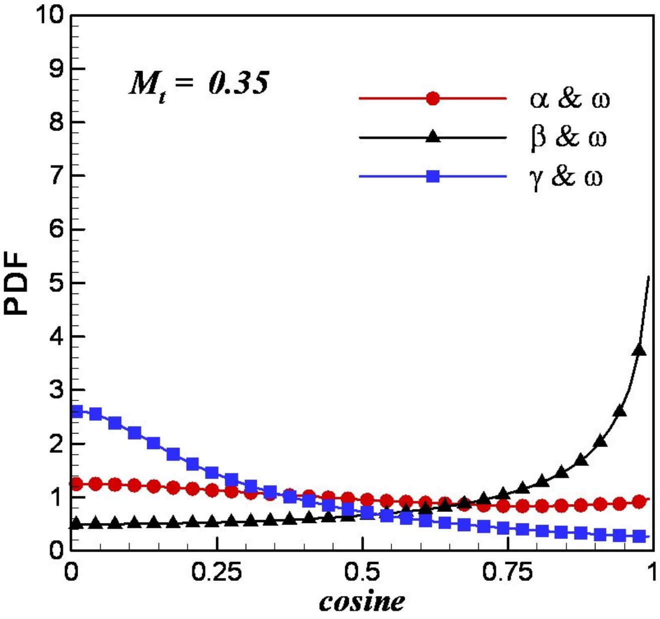

(b) $M_t(0) = 0.413$

Fig. 40. Alignment of vorticity with strain-rate eigenvectors at different turbulent Mach numbers ($Re_\lambda(0) = 55.6$)

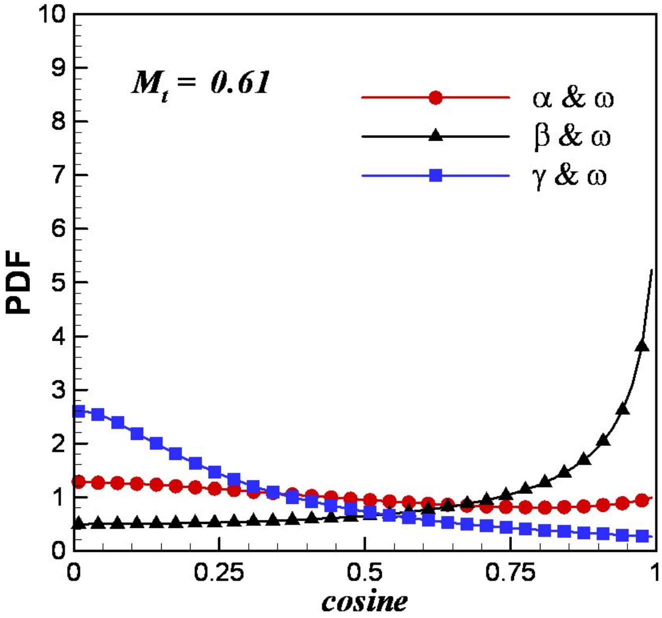

(c) $M_t(0) = 0.708$

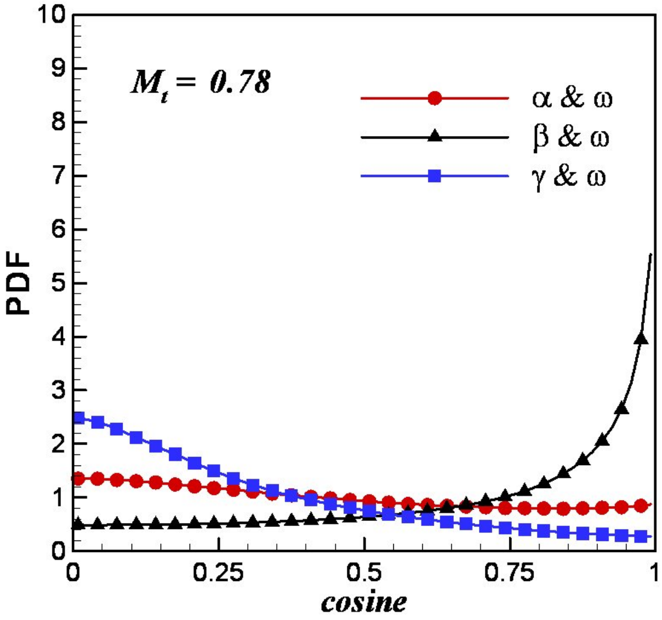

(d) $M_t(0) = 0.885$

Fig. 40. Continued

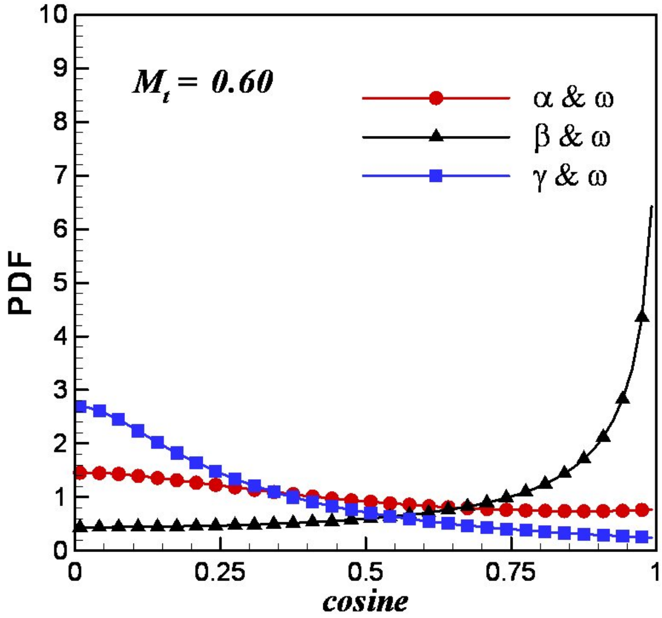

Fig. 41. Alignment of vorticity with strain-rate eigenvectors in higher Reynolds number flows ($Re_\lambda(0) = 110.5$, $M_t(0) = 0.708$)

The alignment of vorticity vector with strain-rate eigenvectors are important because it describes how turbulence effectively cascades down to small scales. The alignment determines whether vortices experience stretching or compression [63]. The vorticity is known to align well with the intermediate strain-rate eigenvector in incompressible flows [59]. We show similar results for low turbulent Mach numbers ($M_t(0) = 0.059$) in Fig. 40(a). The alignment statistics do not change in higher turbulent Mach numbers (Fig. 40(b), 40(c), and 40(d)). However, the alignment of vorticity with the intermediate strain-rate eigenvector becomes stronger at high Reynolds number, as seen in Fig. 40(c) and Fig. 41.

Turbulence has strong intermittent behavior in dissipation scales. The statistics of turbulence deviate from Gaussian distribution, which indicates that a strong coherent flow structure exists in the scale [60]. Now, we examine the effect of turbulent Mach number on the coherence of small-scale structure. The small-scale structure

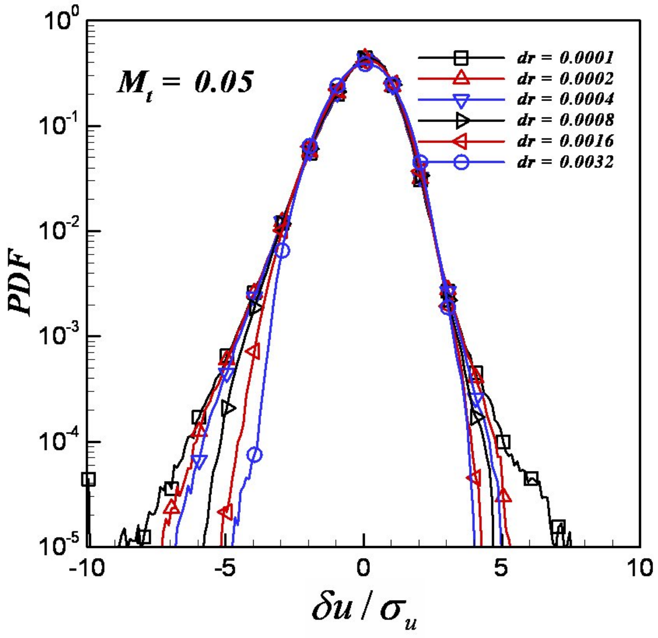

(a) $M_t(0) = 0.059$

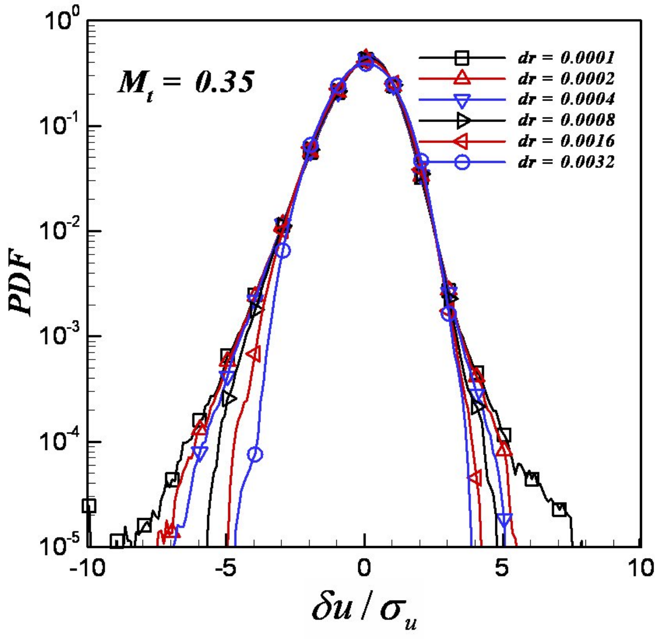

(b) $M_t(0) = 0.413$

Fig. 42. Longitudinal velocity difference distribution at different turbulent Mach numbers ($Re_\lambda(0) = 55.6$)

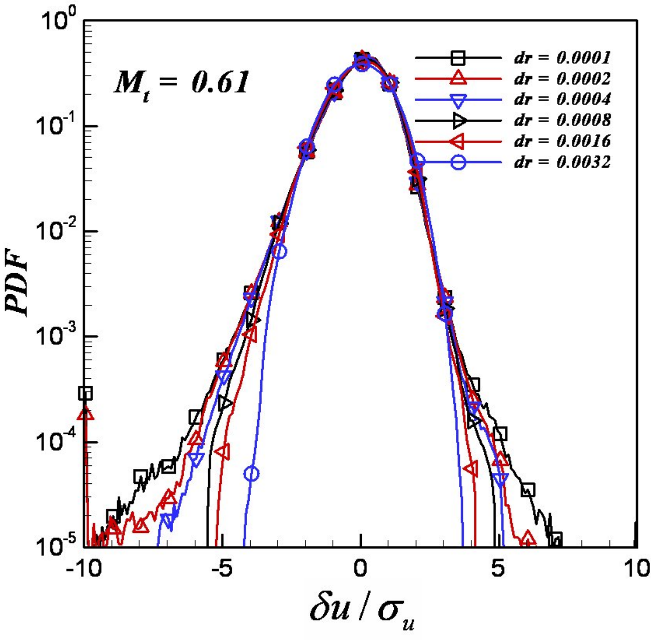

(c) $M_t(0) = 0.708$

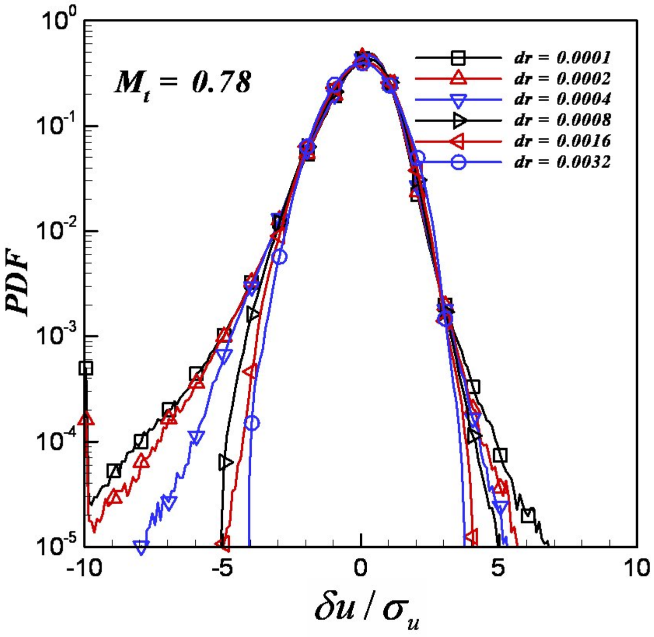

(d) $M_t(0) = 0.885$

Fig. 42. Continued

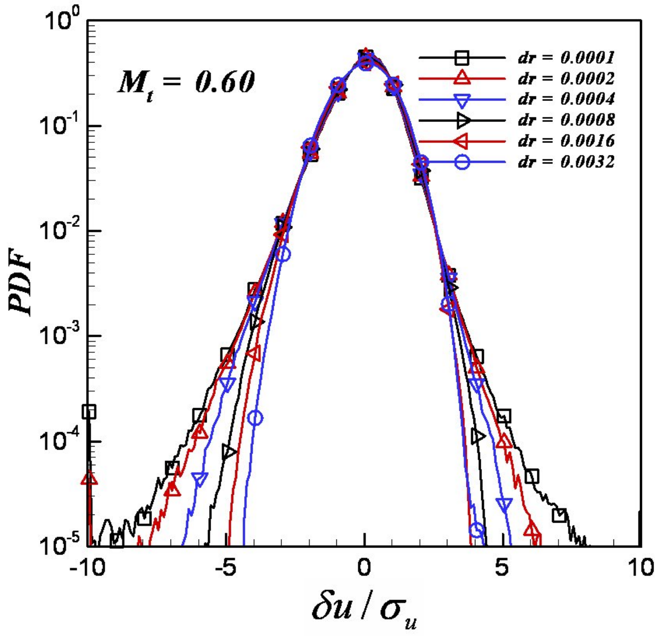

Fig. 43. Longitudinal velocity difference distribution in high Reynolds number flows ($Re_\lambda(0) = 110.5$, $M_t(0) = 0.708$)

can be seen in velocity difference statistics [64]. Longitudinal velocity difference is defined as

$$\delta u \equiv (u(\vec{r} + d\vec{r}) - u(\vec{r})) \cdot \frac{d\vec{r}}{|d\vec{r}|}\,, \tag{6.3}$$

which shows a two point correlation along the velocity vector direction. The probability distributions of longitudinal velocity difference are shown in Figs. 42 and 43, where the velocity difference is normalized by its variance σ_u.

For the case with a turbulent Mach number of 0.06, the distribution of longitudinal velocity difference is studied with various separation dr in (Fig. 42(a)). The distribution has significant amounts of tail pocket in $dr = 0.0001$, which is non-Gaussian distribution and indicates a strong intermittent behavior of turbulence at the scale. As the separation increases, the distribution of longitudinal velocity difference approaches Gaussian distribution, which means that there is no correlation between the two points and it follows Kolmogorov's universal law. As the turbulent Mach number increases (Figs. 42(b), 42(c), and 42(d)), the tail pocket increases in small scales which means that flow field has stronger coherent structure in the scales in high turbulent Mach numbers. Thus, modeling compressible turbulence using one point closure may not give better results than for incompressible turbulence. The effects of Reynolds number on turbulence intermittency is not apparent for the Reynolds number range of 55.6 and 110.5 (Figs. 42(c) and 43).

D. Effect of dilatation

The dilatational field is known to be one of the most distinct flow features in compressible flows. The dilatation distribution is investigated for different turbulent Mach numbers in Fig. 44. It should be noted that all statistics are measured at the cascade peak and beyond so that the non-linear processes are fully in effect. To identify the relative dilatational levels, normalized dilatation, d, is defined as

$$d = \frac{\frac{\partial u_i}{\partial x_i}}{\left(\frac{\partial u_l}{\partial x_m}\frac{\partial u_l}{\partial x_m}\right)^{1/2}}, \tag{6.4}$$

where repeated indices represent summation. The normalized dilatation, d, mathematically ranges from $-\sqrt{3}$ to $\sqrt{3}$.

In low turbulent Mach numbers (Fig. 44(a)), the dilatation exhibits only small departures from zero. As the turbulent Mach number increases, the non-zero dilatation levels increase significantly. For a turbulent Mach number of 0.35 (Fig. 44(b)), the extreme values of dilatation distribution approach 1.5 and -1.6, which are near the mathematical maximum (or minimum) values ($\pm\sqrt{3}$) of dilatation. Non-zero dilatation continues to increase while the peak of the distribution (at $d = 0$) decreases for higher turbulent Mach numbers (Fig. 44(c) and 44(d)). This confirms that the

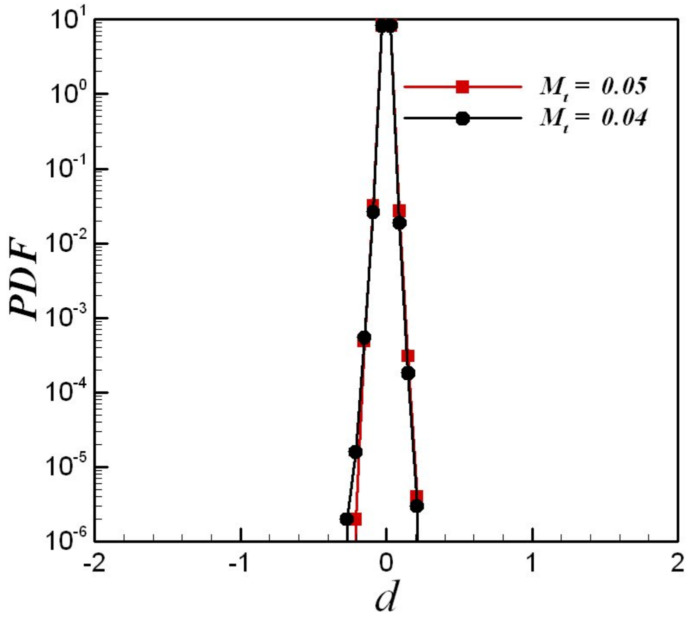

(a) $M_t(0) = 0.059$

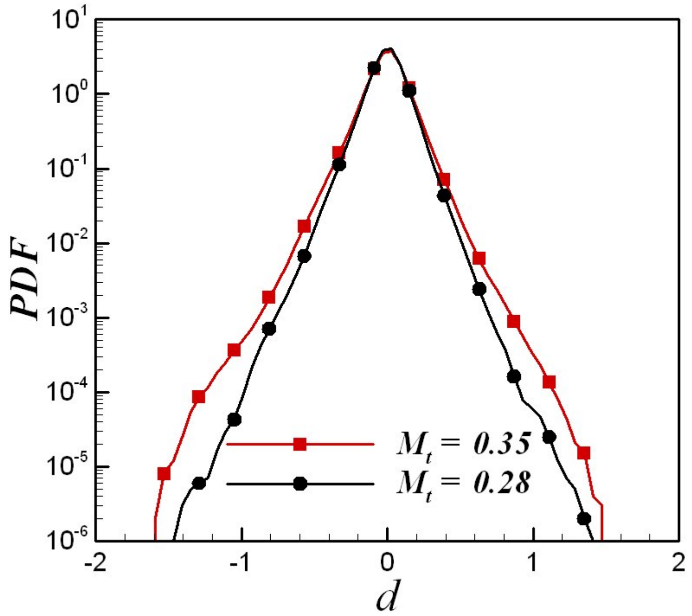

(b) $M_t(0) = 0.413$

Fig. 44. Dilatation distribution at different turbulent Mach numbers ($Re_\lambda(0) = 55.6$)

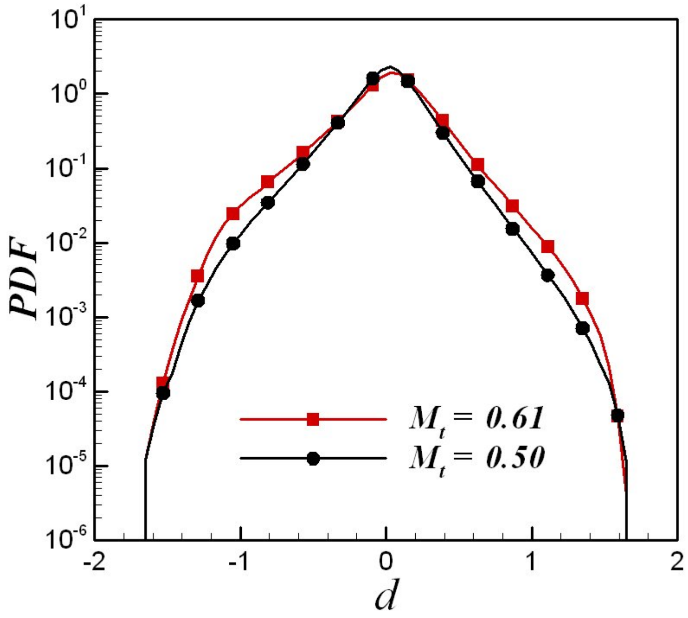

(c) $M_t(0) = 0.708$

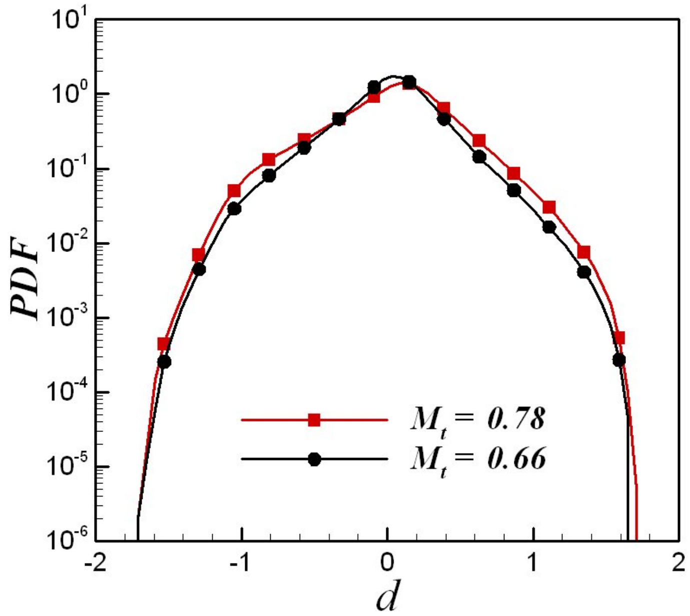

(d) $M_t(0) = 0.885$

Fig. 44. Continued

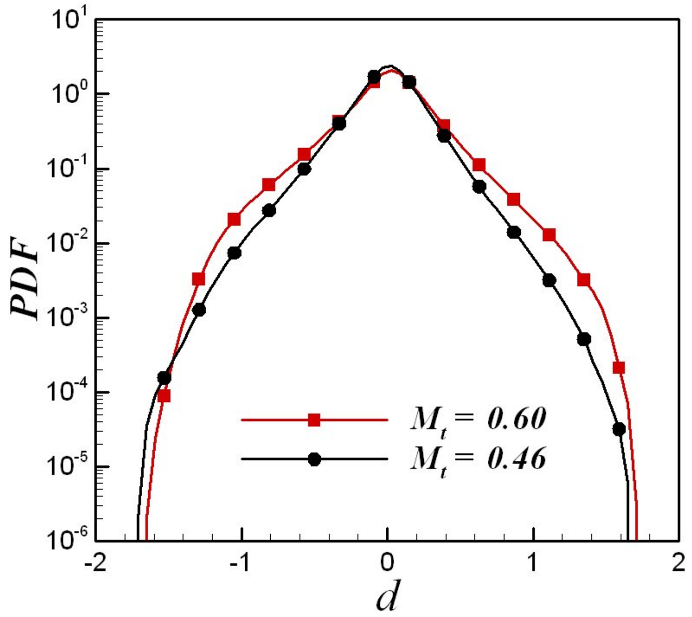

Fig. 45. Dilatation distribution in higher Reynolds number flows ($Re_\lambda(0) = 110.5$, $M_t(0) = 0.708$)

high turbulent Mach number flows have a significant amount of non-zero dilatation, even though the average of dilatation distribution or the most probable dilatation is the same as the incompressible flows. From these results we infer that the average quantities (or most probable quantities) may not be useful in specifying the compressible flows. To see the effect of Reynolds number on the dilatation distribution, the Reynolds number is increased in Fig. 45 with the same initial velocity fields as in Fig. 44(c). It is seen that the Reynolds number does not have significant influence on the dilatation distribution.

The most probable dilatation and eigenvalues do not change as the turbulent Mach number increases (Figs. 44 and 38). At the turbulent Mach number levels considered, dilatational component of fluctuations is quite small, and the effects of positive and negative dilatations could possibly be opposite of one another, leaving the most probable behavior nearly unchanged. Then, the role of dilatation is an

Table V. Range and Number of sample for each dilatation level, d, at $t' = 0.1389$ ($M_t = 0.78$, $Re_\lambda = 31.2$) in Case 4

Median value of d	Range of d	Number of sample
-1.7	$d < -1.60$	54
-1.4	$-1.45 < d < -1.35$	3,725
-1.0	$-1.05 < d < -0.95$	108,741
-0.5	$-0.51 < d < -0.49$	96,626
0.0	$-0.01 < d < 0.01$	401,321
0.5	$0.49 < d < 0.51$	133,926
1.0	$0.95 < d < 1.05$	83,955
1.4	$1.35 < d < 1.45$	8,962
1.7	$1.60 < d$	207

important issue in small-scale structure of turbulence. Therefore, to study compressible turbulence, one must look at the flow characteristics as a function of dilatation level [12]. The velocity field at $t' = 0.1389$ of simulation case 4 ($Re_\lambda(0) = 55.6$ and $M_t(0) = 0.885$) is selected to study the dependence of flow statistics on dilatation level, d. Nine groups are selected as a representation of the range of dilatation level from -1.7 to 1.7. The median value, band width, and number of the sample are given in Table V.

The distributions of eigenvalues are plotted for different dilatation levels in Fig. 46. Overall, as the dilatation level increases, the distribution of eigenvalues increases. The intermediate eigenvalue β increases monotonically as the dilatation level increases from minimum to maximum value. However, it is not monotonic for the largest and smallest eigenvalues. Around the extreme negative dilatation level ($d = -1.7$), the smallest eigenvalue γ decreases even though the dilatation d increases. Its peak

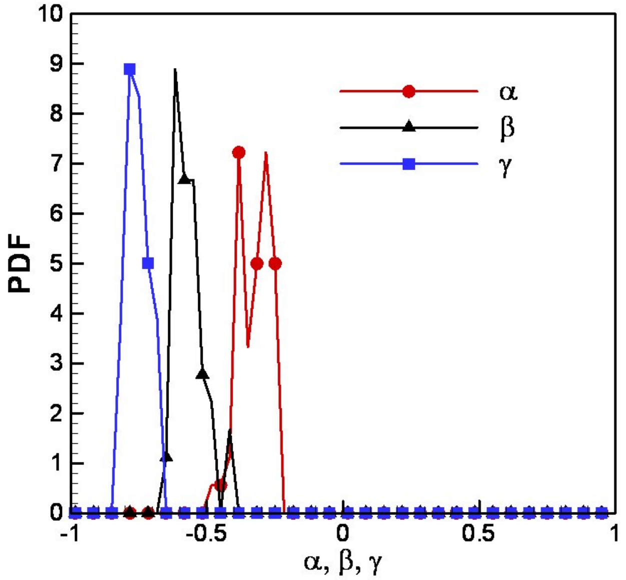

(a) $d = -1.7$

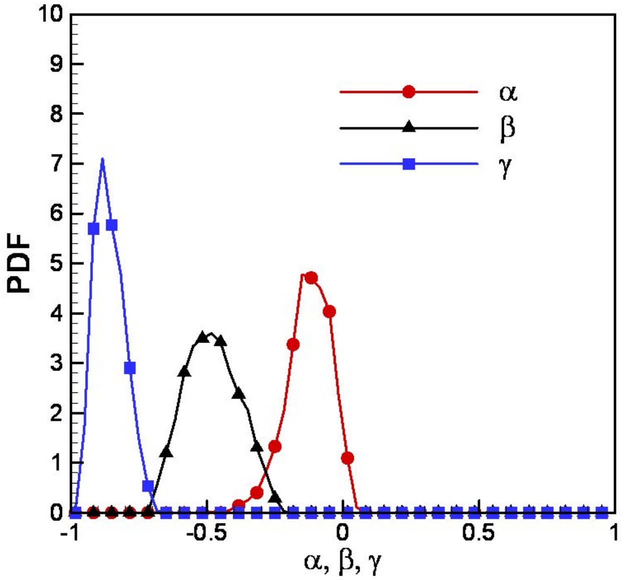

(b) $d = -1.4$

Fig. 46. Strain-rate eigenvalues at different dilatation levels ($Re_\lambda(0) = 55.6$, $M_t(0) = 0.885$)

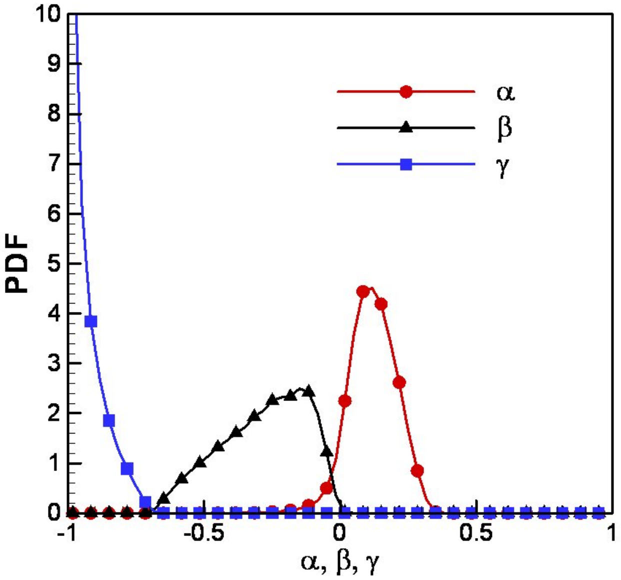

(c) $d = -1.0$

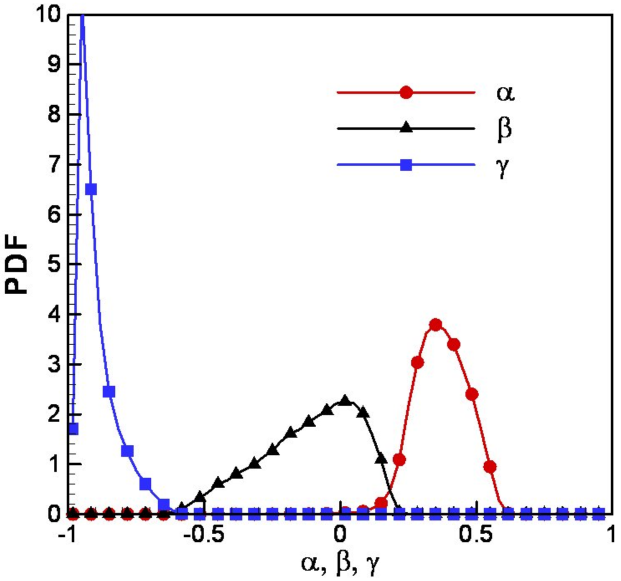

(d) $d = -0.5$

Fig. 46. Continued

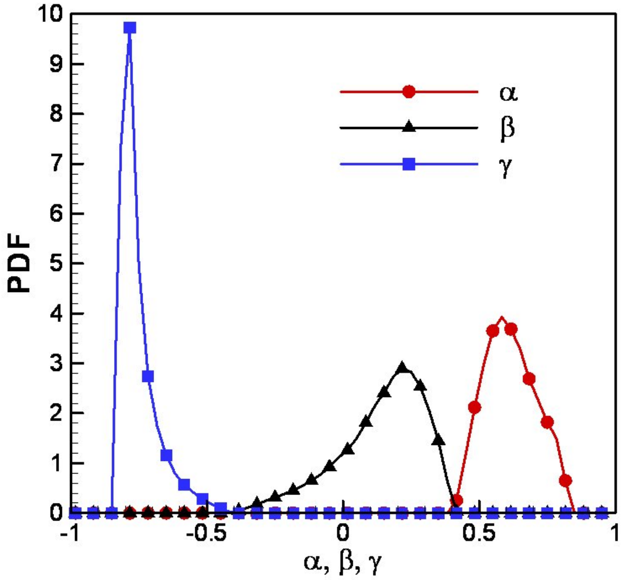

(e) $d = 0.0$

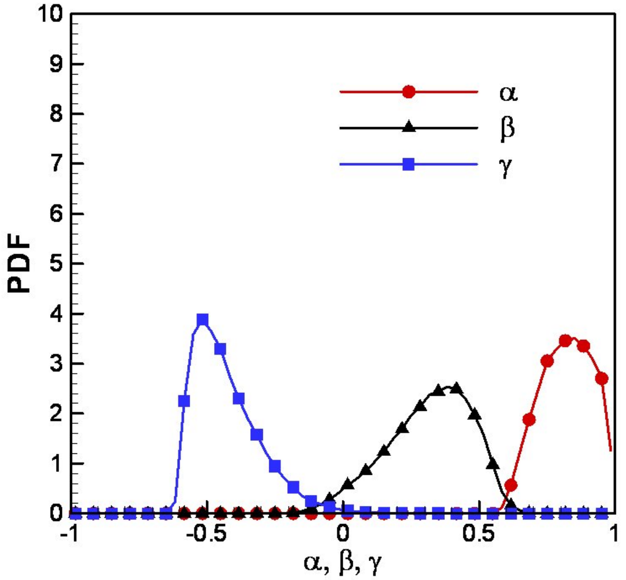

(f) $d = 0.5$

Fig. 46. Continued

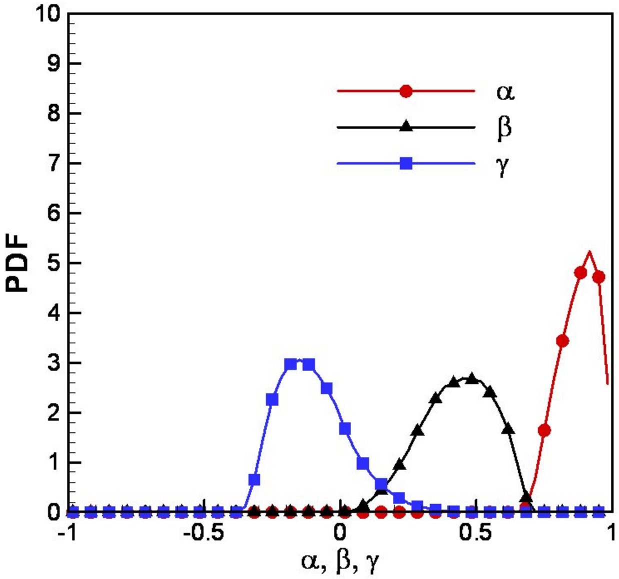

(g) $d = 1.0$

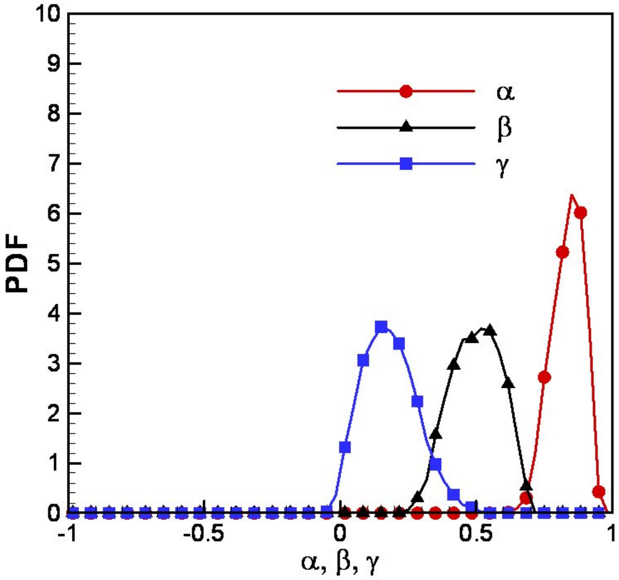

(h) $d = 1.4$

Fig. 46. Continued

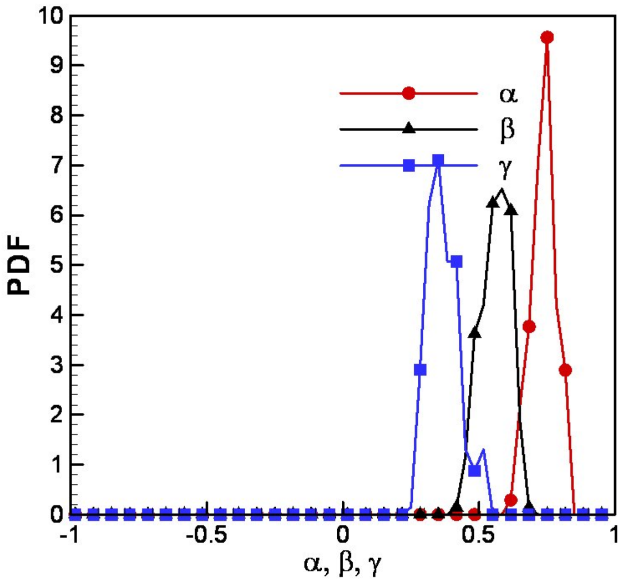

(i) $d = 1.7$

Fig. 46. Continued

reaches $\gamma = -1.0$ at $d = -1.0$. At $d = -1.0$ (Fig. 46(c)), the largest eigenvalue α is relatively negligible and the flow structure experiences two-dimensional compression. But as already acknowledged, for extreme negative values of d, all three eigenvalues approach each other and the flow experiences nearly isotropic compression as seen in Fig. 46(a).

The distribution of eigenvalues conditioned on $d = 0$ is the same as that of incompressible turbulence (Fig. 46(e)). As we increase the dilatation level, d, to positive values, the largest eigenvalue α has a trend similar to the smallest eigenvalue γ in the negative dilatation level. The largest eigenvalue α increases as the dilatation level, d, increases, and the peak of the largest eigenvalue α reaches around $\alpha = 1.0$ at $d = 1.0$ (Fig. 46(g)). At $d = 1$, the expansion is much stronger in the largest and intermediate strain-rate directions than in the smallest strain-rate direction, and flow field experiences two-dimensional expansion. As the dilatation level increases

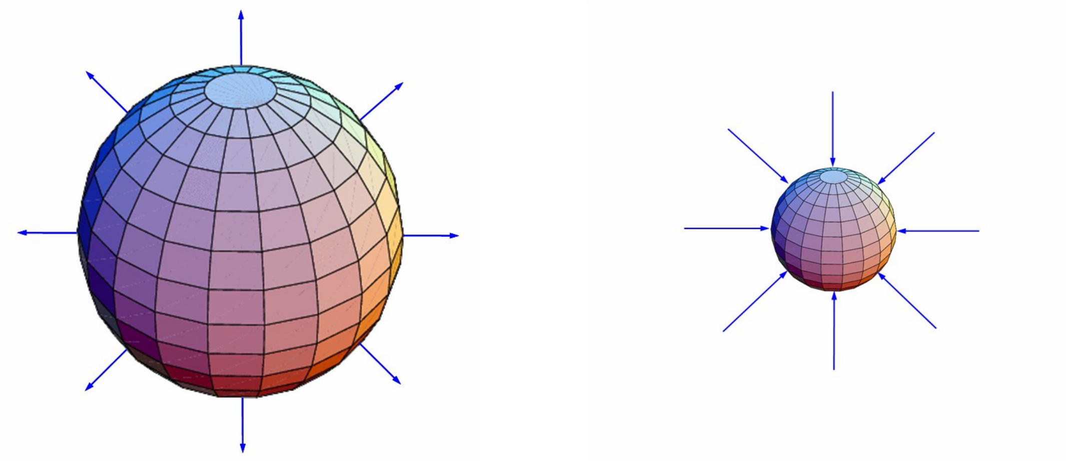

(a) Three-dimensional isotropic expansion in positive extreme dilatation region ($d = 1.7$)

(b) Three-dimensional isotropic compression in negative extreme dilatation region ($d = -1.7$)

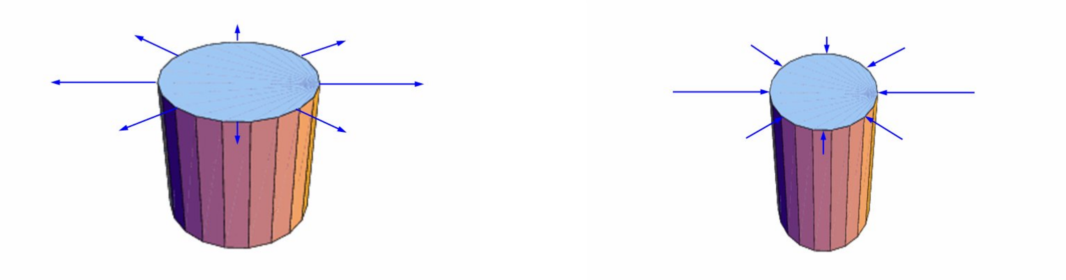

(c) Two-dimensional expansion in positive intermediate dilatation region ($d = 1.0$)

(d) Two-dimensional compression in negative intermediate dilatation region ($d = -1.0$)

Fig. 47. Deformation of small-scale structure in compressible flows

further to the extreme positive value ($d = 1.7$), the most probable value of the largest eigenvalue α decreases and approaches the intermediate and smallest eigenvalues (β and γ). At the positive extreme value of dilatation level ($d = 1.7$), the smallest eigenvalue γ is positive and the flow experiences nearly isotropic expansion (Fig. 46(i)).

Thus, it can be confirmed that at the extreme dilatation levels, either positive or negative, flow tends to expand or contract isotropically, which does not change the flow structure significantly as seen in Figs. 47(a) and 47(b). But at intermediate dilatation levels ($d = 1.0$ or -1.0), flow field undergoes two-dimensional expansion or compression, which leads to radical changes in flow structure, as seen in Figs. 47(c) and 47(d). Thus, we confirm that the small-scale structure of turbulence strongly depends on the dilatation level.

The alignment of vorticity with strain-rate eigenvectors are studied with the condition on dilatation level. The effect of dilatation is obvious in the alignment of vorticity with strain-rate eigenvectors as seen in Fig. 48. The intermediate strain-rate eigenvector is well aligned with vorticity at a low dilatation level. Especially at $d = 0$, the alignment characteristics agree well with that of incompressible flows [59]. As the dilatation level, d, increases or decreases, flow field loses its alignment characteristics dramatically, as seen in Fig. 48(c) and 48(e). This confirms that in the strong dilatation region, the vorticity field is weak, leading to random distribution of alignment of vorticity with the other vectors including strain-rate eigenvectors at high dilatation levels.

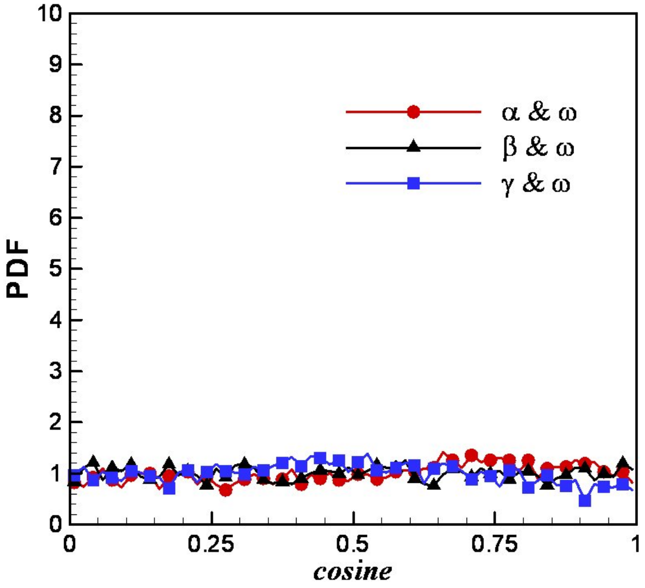

(a) $d = -1.4$

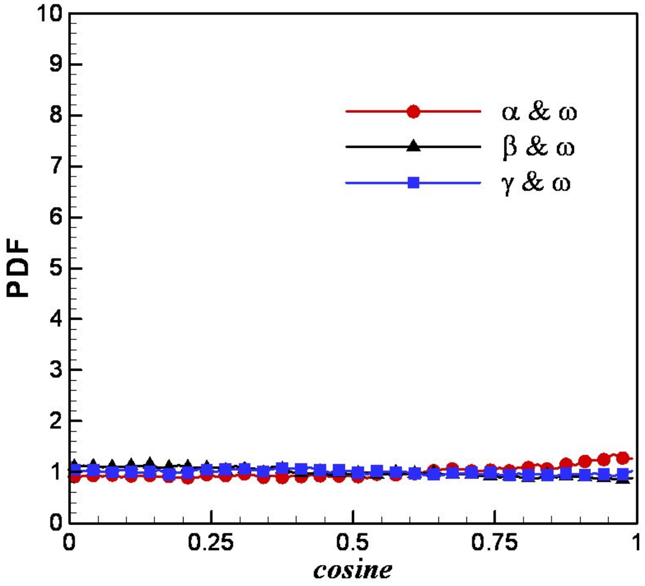

(b) $d = -1.0$

Fig. 48. Alignment of vorticity with strain-rate eigenvectors at different dilatation levels ($Re_\lambda(0) = 55.6$, $M_t(0) = 0.885$)

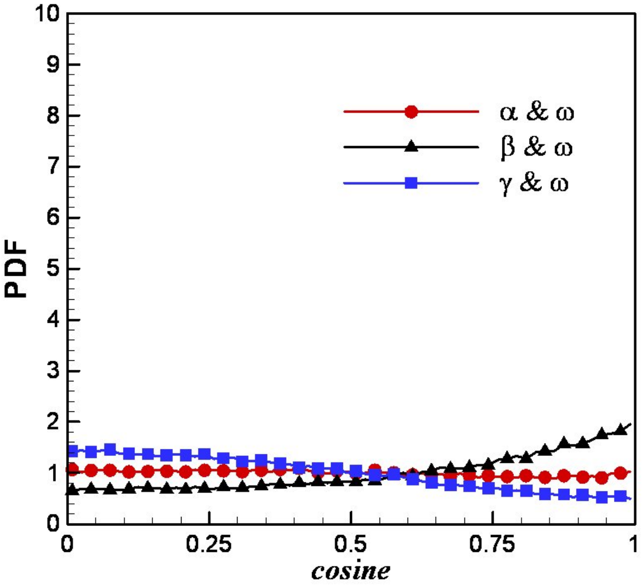

(c) $d = -0.5$

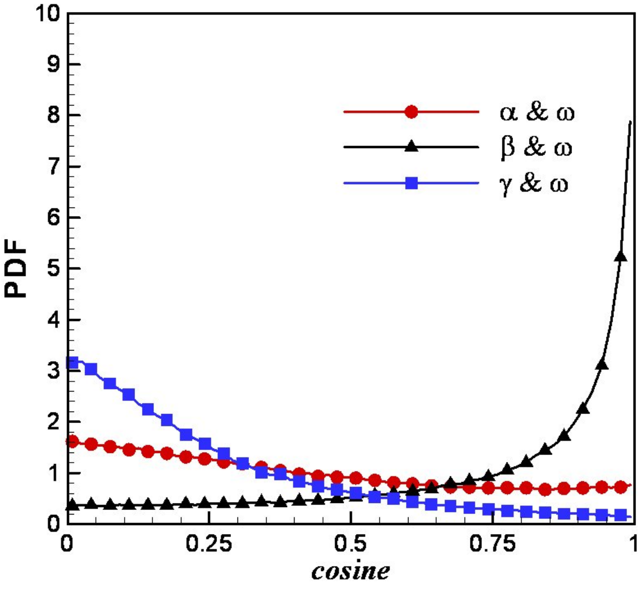

(d) $d = 0.0$

Fig. 48. Continued

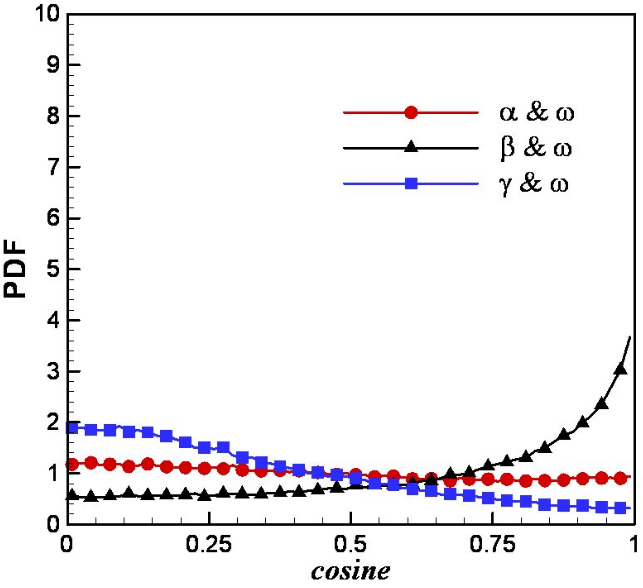

(e) $d = 0.5$

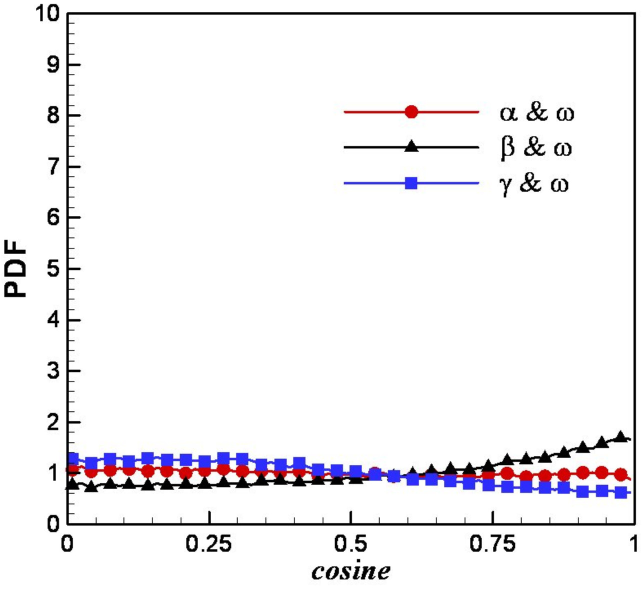

(f) $d = 1.0$

Fig. 48. Continued

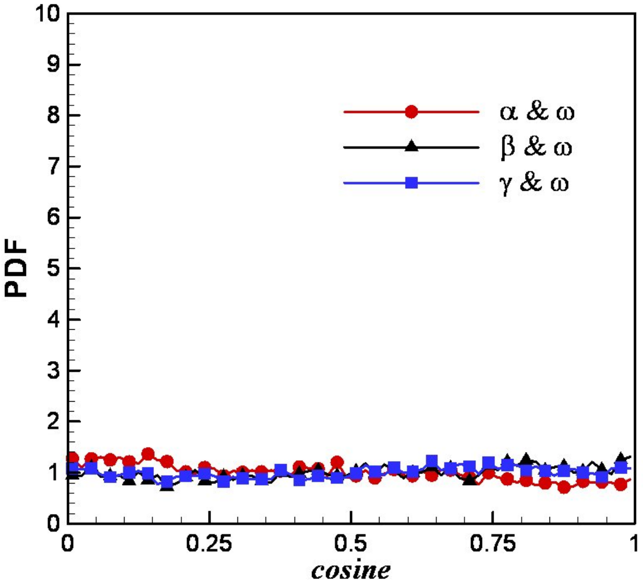

(g) $d = 1.4$

Fig. 48. Continued

E. Conclusions

The small-scale structure of compressible turbulence is studied using the gas kinetic method (GKM). The simulation parameters are the turbulent Mach number and the Taylor-scale Reynolds number. The initial velocity field is the solenoidal isotropic turbulence, and the initial pressure, density, and temperature fluctuations are set to zero. The unbalanced flow field undergoes a transient state until it balances with the thermodynamic variables. The small-scale structures are investigated at the time of cascade peak and beyond. The important findings are:

(1) The kinetic energy and dissipation rate depend weakly on the turbulent Mach number, but strongly on the Reynolds number. The most probable strain-rate eigenvalues do not change as the turbulent Mach number increases. However, the distribution of dilatation and eigenvalues change significantly depending on the turbulent Mach number, which indicates the need for detailed study of the statistics.

(2) Intermittent behavior of small-scale turbulence tends to increase as turbulent Mach number increases. Thus, modeling compressible turbulence using one point closure may not give better results than for incompressible turbulence.

(3) The flow structure strongly depends on dilatation level. It is found that at extreme dilatation level ($d = 1.7$ or -1.7), flow field may experience isotropic expansion or compression. At the intermediate dilatation level ($d = 1.0$ or -1.0), flow field experiences two-dimensional expansion or compression, which deforms the flow structure significantly. At zero dilatation level ($d = 0$), the flow field reveals the same strain-rate eigenvalue distribution as in incompressible flows. The preferential alignment between vorticity and strain-rate eigenvectors weakens in strong dilatation region as vorticity itself starts to vanish.

CHAPTER VII

VARIABLE TRANSPORT-COEFFICIENT EFFECTS ON DISSIPATION PROCESSES

In aerodynamic flow over hypersonic vehicles, there exist steep temperature gradients in the shock zones and viscous boundary layers. The temperature gradients induce variation in transport coefficients, such as viscosity, conductivity, and diffusivity. We study the effects of these transport-coefficient variations on velocity and scalar field fluctuations. A Boltzmann-equation based direct numerical simulations are performed with a binary mixture of fluids with identical densities but vastly different viscosities and diffusivities. The initial velocity field is isotropic with each fluid occupying one-half of the computational domain, which is a 256^3 box of turbulence with Taylor-scale Reynolds numbers of 40 and 200. We confirm the Taylor (1935) conjecture by showing that the small scale velocity and scalar field fluctuations adjust themselves to the imposed viscosity and diffusivity. Dissipation rates of both turbulence and scalar field tend to be uniform over the flow domain with different transport coefficients. This study can also be applied to a non-premixed combustion problem, where the rate of molecular mixing depends on the scalar dissipation rate.

A. Introduction

In hypersonic flight, the flow experiences a high temperature gradient through the shock and around the boundary layer. The steep change in temperature induces variation of fluid properties, including viscosity, conductivity, and diffusivity [1]. Viscosity is considered to be a destruction media for turbulence field at small scales, whereas diffusivity destroys the small scales of the scalar field. Thus, the viscosity variation is expected to affect the turbulent energy dissipation process in the flow, which is critical in predicting force around the hypersonic vehicle. Similarly, the diffusivity variation affects the mixing properties at a molecular level. In this study, we focus on the effect of viscosity and diffusivity variations on turbulent kinetic energy and scalar field dissipation.

Turbulence is produced at large scales by the action of mean velocity gradients and then it cascades down to small scales due to nonlinear interactions. At the final stage of the turbulence life-cycle, turbulent energy is dissipated at small scales by the action of molecular viscosity [3, 4, 65]. The dissipation, at inertial scales, is considered to be a nonlinear cascading process. It does not depend on the viscosity but on the production rate of large scale turbulence. However, at dissipation scales, the dissipation is influenced by viscosity as well as by the energy cascading rate.

In 1935, Taylor [66] conjectured that at high Reynolds numbers, dissipation is considered to be an outer scale variable since it is determined by the characteristic outer scale variables:

$$\varepsilon \sim \frac{u^3}{l}\,, \tag{7.1}$$

where u is the energy containing characteristic velocity and l is the length scale of the characteristic velocity field. Taylor's conjecture implies that dissipation is governed by outer scale variables even though its scale is determined by inner scale variables. Kolmogorov [67, 68] greatly influenced turbulence study with his hypotheses (K41) on the statistics of small scale turbulence. In the first hypothesis of similarity, he proposed that at very high, but not infinite Reynolds numbers, all small-scale statistical properties are uniquely and universally determined by the mean kinetic energy dissipation rate and viscosity. In the second hypothesis of similarity, he stated that in the limit of infinite Reynolds numbers, all small-scale statistical properties are uniquely and universally determined only by the mean kinetic energy dissipation rate. The second Kolmogorov hypothesis implies that viscosity does not affect the dissipation rate and viscosity controls the dissipation scale.

Sreenivasan [69] examined various experimental data and found that in a square-mesh grid generated turbulence, the non-dimensional dissipation rate, $\varepsilon l_0/u_0^3$, is independent of Reynolds number for $50 < R_\lambda < 500$, where R_λ is the Taylor-scale Reynolds number defined as $u\lambda/\nu$; λ is the Taylor micro-scale; ν is the kinematic viscosity; ε is the mean kinetic energy dissipation rate; l is the characteristic length scale; and u is the characteristic velocity scale. Brachet *et al.* [70] performed Navier-Stokes direct numerical simulations (DNS) with a Taylor-Green vortex flow at various Reynolds numbers ($100 < R_\lambda < 3000$). They found that the peak value of dissipation rate changes by only 30% even though the Reynolds numbers are altered by the order of magnitude. Frisch [64] explained the independence of viscosity from dissipation rate with a conceptual derivation of the energy dissipation rate of a moving object. The energy dissipation rate is a function of drag coefficient, which does not involve viscosity at high Reynolds numbers. Thus, high Reynolds number flows have a finite limit in energy dissipation rate irrespective of viscosity.

While Sreenivasan [69] and Brachet *et al.* [70] drew the conclusion from various different experiments or simulations, we study the viscosity independence from dissipation in a simulation domain with a given viscosity variation. At the same time, the scalar field is allowed to evolve to study the effects of diffusivity variation on the scalar field mixing properties.

B. Computational method and simulation parameters

In this study, the gas kinetic method (GKM) [42] is applied for the Boltzmann BGK equation, and various statistics of isotropic turbulence are obtained. The solution from this method is known to give the same results as Navier-Stokes DNS for nearly incompressible flows [43]. The details of the method can be found in Kerimo and Girimaji [43]. The corresponding Navier-Stokes equation of the GKM is

$$\frac{\partial \rho}{\partial t} + \frac{\partial \rho u_j}{\partial x_j} = 0\,; \tag{7.2}$$

$$\frac{\partial \rho u_i}{\partial t} + \frac{\partial \rho u_i u_j}{\partial x_j} = -\frac{\partial p}{\partial x_i} + \frac{\partial \sigma_{ij}}{\partial x_j}\,, \tag{7.3}$$

where $\sigma_{ij} = 2\mu s_{ij} - \frac{2}{3}\mu s_{kk}\delta_{ij}$ and s_{ij} is the strain rate tensor. We do not list the energy equation since it barely contributes to dissipation physics in nearly incompressible flow. For a scalar field, a passive scalar diffusion equation is used:

$$\frac{\partial \phi}{\partial t} + \frac{\partial \phi u_j}{\partial x_j} = D\frac{\partial^2 \phi}{\partial x_j \partial x_j}\,, \tag{7.4}$$

where D is the diffusivity of scalar field. Viscosity and diffusivity are also allowed to evolve as a passive scalar. We confine our interests in nearly incompressible flow, so that the turbulent Mach number ($M_t = \sqrt{u_i u_i}/a$) of our simulations is set to 0.01. Even though GKM is a compressible solver, the physics of incompressible turbulence can be captured in this low turbulent Mach number flow simulation.

The computational domain is a cubic box of turbulence and consists of 16.8 million nodes (256^3). The grid size and time step is $1 \times 10^{-4} m$ and $1 \times 10^{-7} s$. The initial velocity field is isotropic turbulence and the number of the characteristic wave of turbulence ranges from 1 to 16 in the domain. The viscosity is initially set to $2 \times 10^{-5} Pa \cdot s$ in one half of the domain and $1 \times 10^{-4} Pa \cdot s$ in the other half, which correspond to the Taylor-scale Reynolds numbers of 200 and 40. The density, temperature and gas constant are set to $1.0 kg/m^3$, $300K$ and $287 J/kgK$ respectively. The Prandtl number and specific heat ratio are set to 0.7 and 1.4. The diffusivity is initially set to $2 \times 10^{-5} m^2/s$ in one half of the domain and $1 \times 10^{-4} m^2/s$ in the other half.

C. Velocity field dissipation

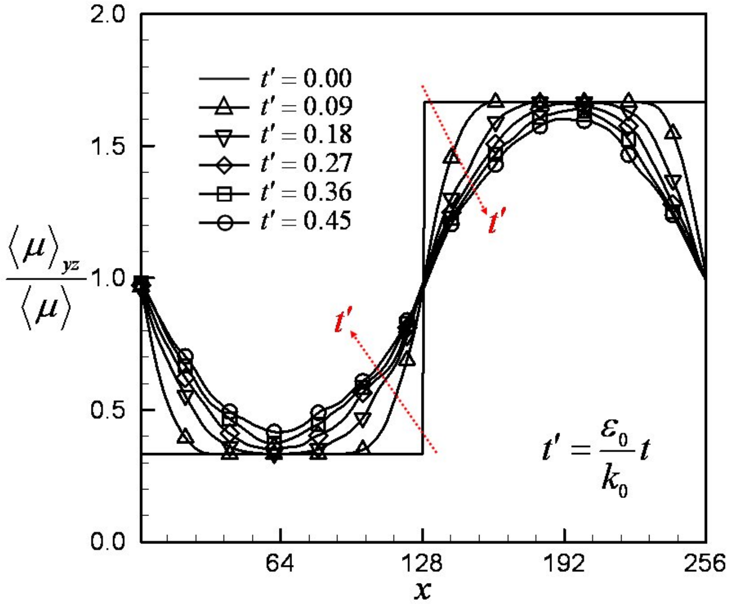

Fig. 49. Plane averaged viscosity variation

To investigate the effect of variable viscosity on turbulence, we present the $yz-$plane averaged quantities, $\langle\cdots\rangle_{yz}$, along the $x-$coordinate. The viscosity variation, $\langle\mu\rangle_{yz}$, normalized by the volume averaged viscosity, $\langle\mu\rangle$, is plotted in Fig. 49. The time is normalized by the initial turbulence eddy turnover time such that $t' = t\frac{\varepsilon_0}{k_0}$. Initially, we have five times higher viscosity in one side than in the other. Due to diffusion and advection, the two different viscosities diffuse. But the flow domain keeps the strong viscosity variation while other statistical properties of the flow are investigated. In Fig. 50, we present the kinetic energy variation, which is normalized by the initial average kinetic energy, k_0. The initial kinetic energies are statistically the same along the $x-$coordinate. As flow evolves, the kinetic energy in a high vis-

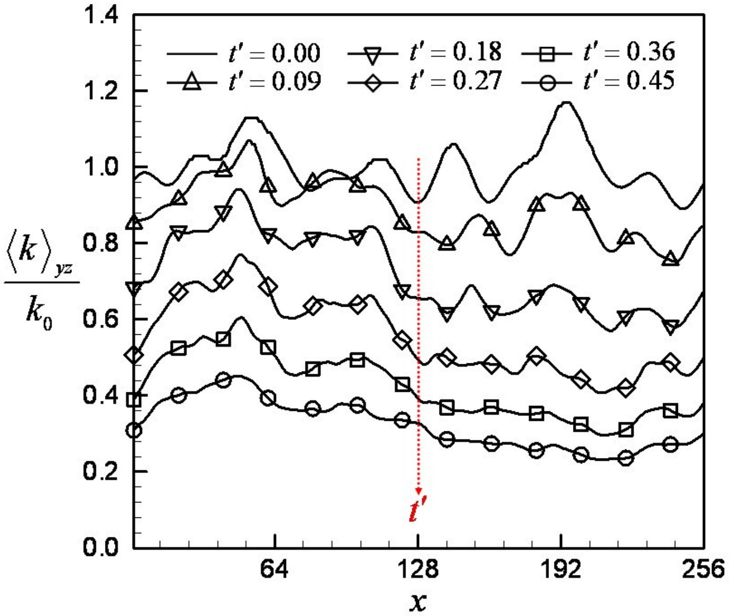

Fig. 50. Plane averaged kinetic energy

cosity region becomes lower than in a low viscosity region, which means that the flow with high viscosity dissipates more turbulent energy into heat than that with low viscosity.

Now we examine the dissipation rate and scale. The dissipation rate, $\varepsilon = 2\mu s_{ij}s_{ij}$, is presented in Fig. 51. The initial dissipation rate is five times higher in a high viscosity region, since we set five times higher viscosity in the region with the same strain rate, s_{ij}, along the $x-$coordinate. The dissipation rate tends to become uniform as the flow evolves. In this case, after about half eddy turnover time, the dissipation rate reflects a uniform distribution along the $x-$coordinate. It should be noted that the flow field still has a vast variation of viscosity on either side during this investigation. This confirms that the dissipation rate tends to be independent of viscosity even in this low Reynolds number flow.

The uniform dissipation rate is obtained through the scale adjustment of the

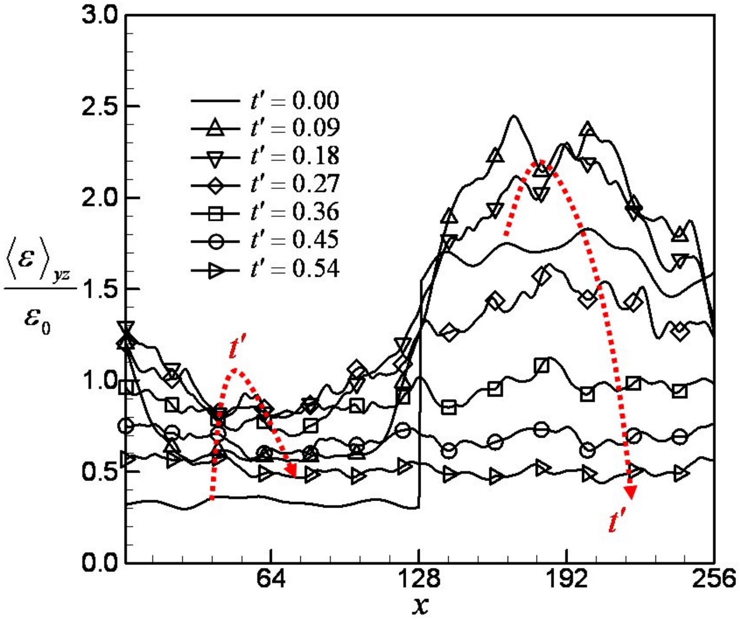

Fig. 51. Plane averaged dissipation rate

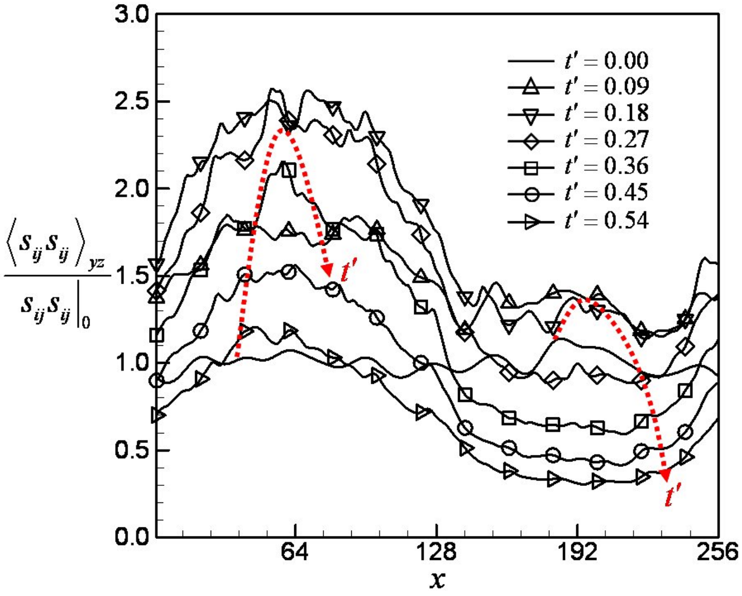

Fig. 52. Plane averaged strain-rate magnitude

velocity field, as seen in the variation of the strain-rate magnitude, $\langle s_{ij}s_{ij}\rangle_{yz}$, in Fig. 52. The higher magnitude of strain rate implies that the flow field has more small scales in the flow. As seen in Fig. 52, the flow field generates more small scales in the low viscosity region than in the high viscosity region. The viscosity itself is not enough to dissipate turbulent energy in the low viscosity region, so that much more small scale motion is generated to accommodate the low viscosity of the fluid. Thus, we confirm that the strain rate depends on viscosity.

The turbulence scale can also be seen in the energy spectrum (Fig. 53). Two locations in high and low viscosity regions ($x = 64$, 192) are selected for the energy spectrum, which provides extreme scale difference in the flow. The initial energy spectrums in both locations show the same scale distribution as seen in the figure. But as flow evolves, more small scales are generated in the low viscosity region than in the high viscosity region. To visualize the difference of turbulence scale, we present the vorticity iso-surface in Fig. 54. The vorticity iso-surface describes how many scales are in the domain for a given vorticity. As seen in the figure, the initial turbulence scales are the same in all regions and the iso-vorticity surface forms a mild sphere-like shape. But as flow evolves, the turbulence field is stretched. Especially, turbulence in a low viscosity region generates more scales than in a high viscosity region, as seen in the second and third figures in Fig. 54. The dissipation rate is visualized with iso-surface in Fig. 55, where we describe the square-root of dissipation at $t' = 0.45$. It should be noted that the total area of a dissipation iso-surface is uniform along the $x-$coordinate, which means uniform distribution of the dissipation rate over the domain. From Figs. 52, 53, 54, and 55, we confirm that small scale turbulence adjusts itself to the magnitude of viscosity in order to make the dissipation rate independent of viscosity. Thus, the implication of Taylor's conjecture is validated after about a half eddy turnover time in this low Reynolds number flow simulation.

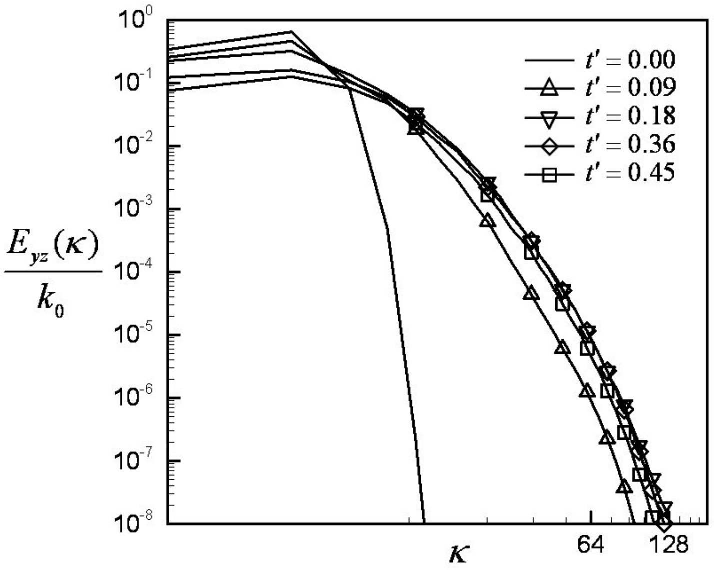

(a)

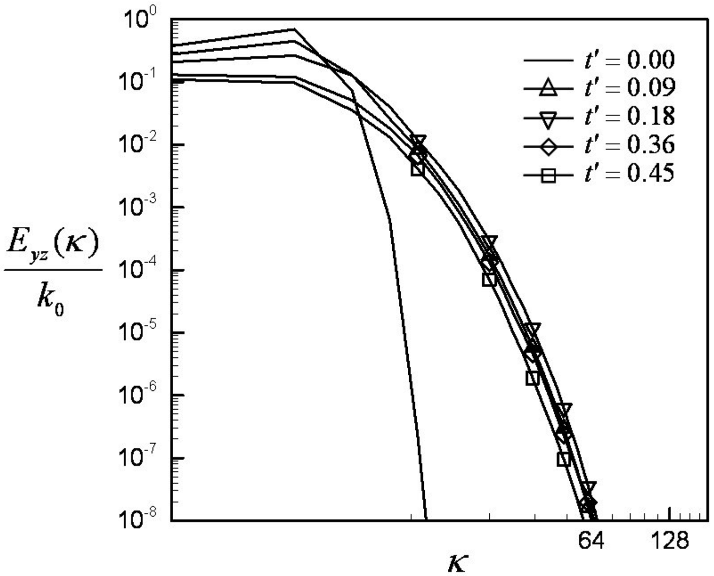

(b)

Fig. 53. Energy spectrum at (a) low viscosity region ($x = 64$) and (b) high viscosity region ($x = 192$). E_{yz} denotes the energy spectrum at a given $yz-$plane.

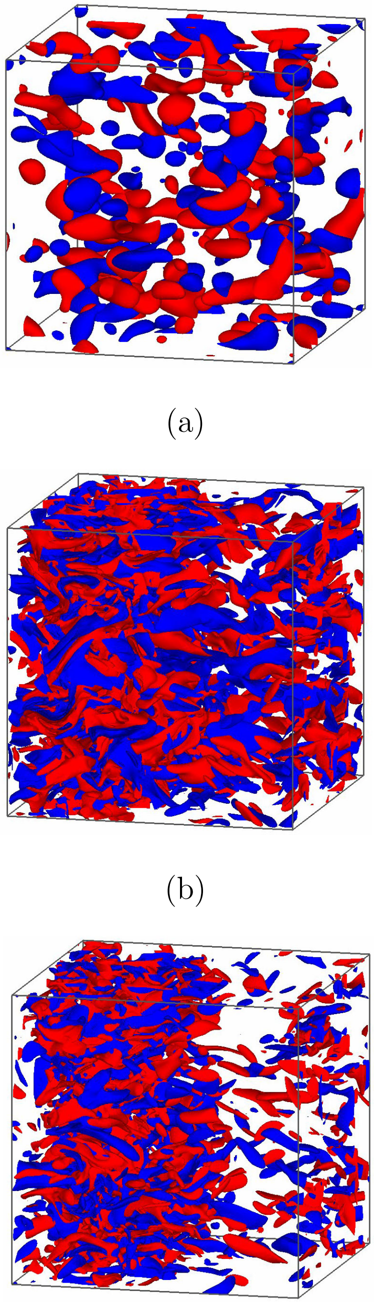

(a)

(b)

(c)

Fig. 54. Iso-surface of $x-$component vorticity, w_x, at (a) $t' = 0.0$; (b) $t' = 0.27$; and (c) $t' = 0.45$. Blue and red describe the opposite sign of vorticity with the same magnitude($w_x = -5000$ and 5000).

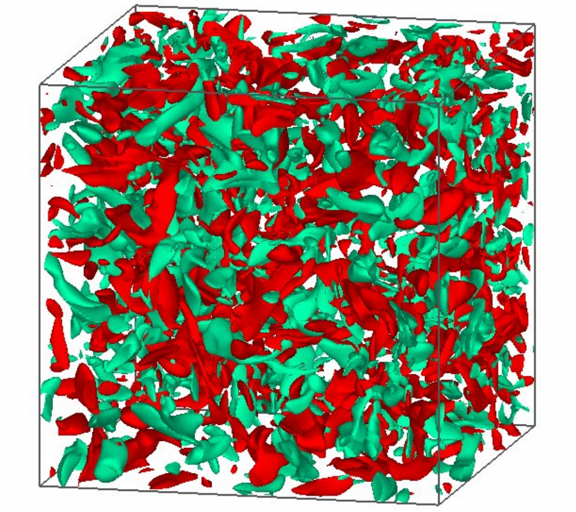

Fig. 55. Iso-surface of the dissipation rate square-root, $\sqrt{\mu}s_{ij}$, at $t' = 0.45$. The green and red denote the same magnitude but opposite sign ($\sqrt{\mu}s_{ij} = -30$ and 30).

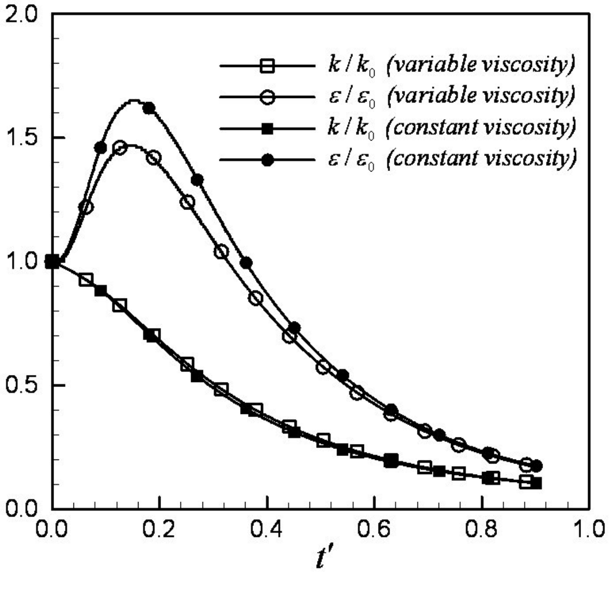

Fig. 56. Comparison of two simulations with variable viscosity and corresponding constant viscosity

The alignment between vorticity and strain rate eigenvector is known to play an important role in vortex stretching, which accelerates the energy cascading process. However, the alignment is not altered much with viscosity variations in low or moderate Reynolds number flow simulations (figures are not shown here).

To see whether one could use an averaged constant viscosity model for variable viscosity flows, we simulate the same flow field with a constant viscosity corresponding to the average of variable viscosity. In Fig. 56, the volume average of the kinetic energy and dissipation rate are presented. The dissipation rate is higher in constant viscosity flow than in variable viscosity flow at early times before a half eddy turnover time. But after about a half eddy turnover time, the two methods give nearly the same dissipation rate.

D. Scalar field dissipation

The effects of variable diffusivity on scalar field dissipation are investigated. The diffusivity variation, $\langle D \rangle_{yz}$, normalized by the volume averaged viscosity, $\langle D \rangle$, is plotted in Fig. 57. Initially, we have five times higher diffusivity in one side than in the other. The diffusivity is allowed to diffuse itself. However, the flow domain keeps the steep diffusivity variation while we investigate other statistical properties of the flow.

Now, the scalar field dissipation rate and scale are studied. The scalar field dissipation rate, $\varepsilon_\phi = 2D\phi_i\phi_i$, is presented in Fig. 58. The initial scalar field dissipation rate is five times higher in the high viscosity region, since we set the five times higher diffusivity in the region with the same scalar field gradient, ϕ_i, along the $x-$coordinate, where $\phi_i = \frac{\partial \phi}{\partial x_i}$. The scalar field dissipation rate tends to become uniform as the flow evolves. In this case, after about 0.7 eddy turnover time, the

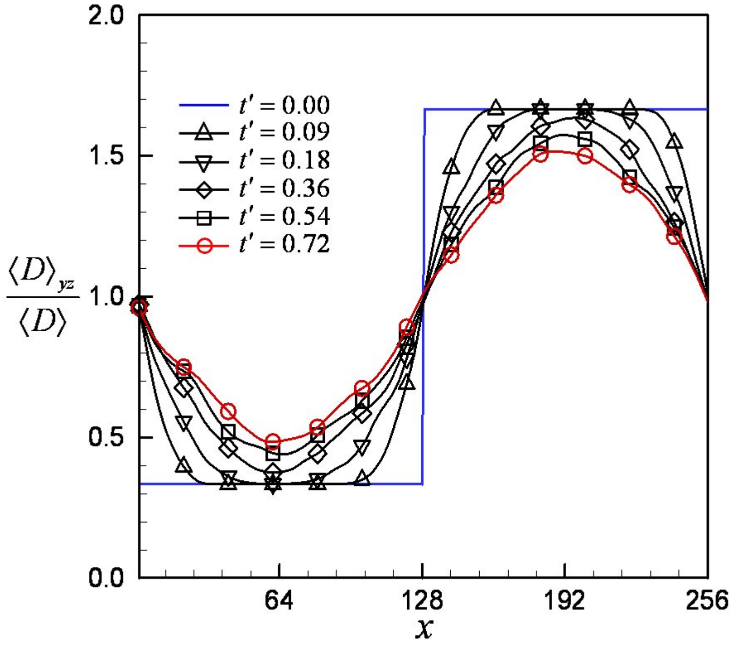

Fig. 57. Plane averaged diffusivity variation

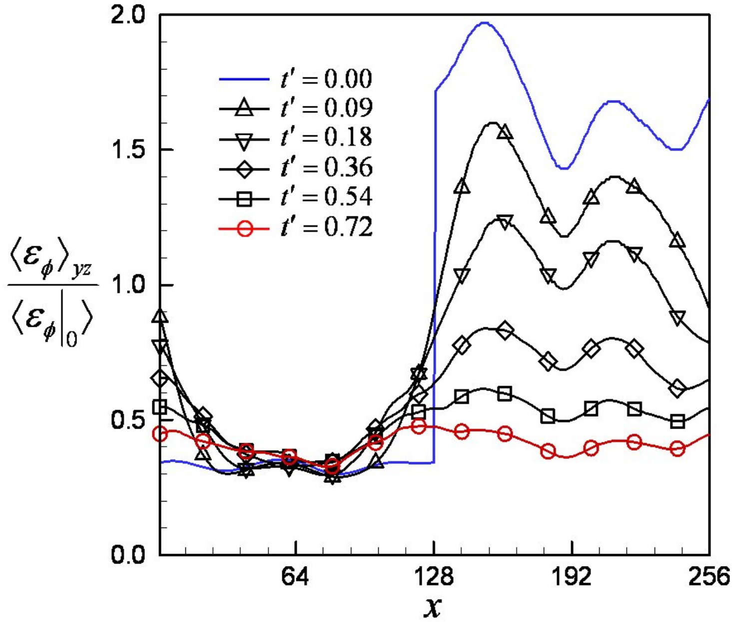

Fig. 58. Plane averaged scalar field dissipation rate

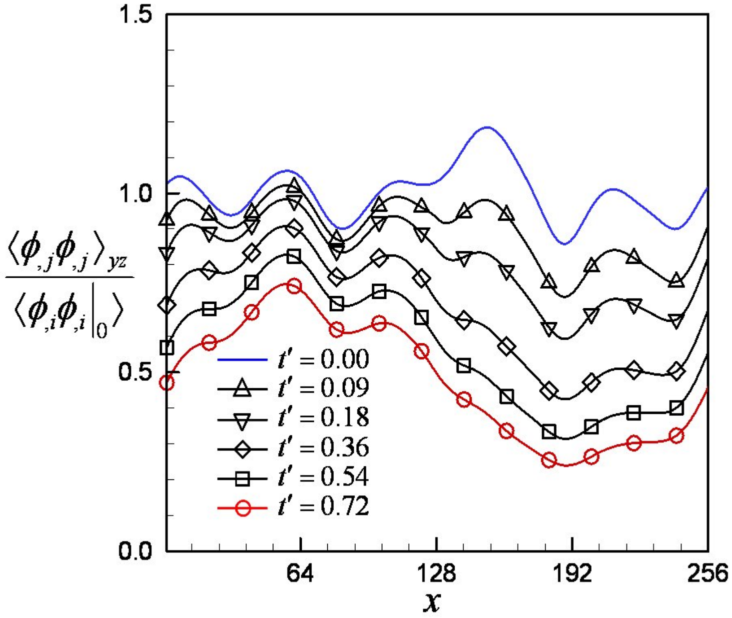

Fig. 59. Plane averaged scalar field gradient

scalar field dissipation rate shows uniform distribution along the $x-$coordinate. This confirms that the scalar field dissipation rate tends to be independent of diffusivity.

As in the velocity field, uniform scalar field dissipation rate is obtained through the scale adjustment of the scalar field, as seen in the variation of the scalar gradient magnitude, $\langle \phi_i \phi_i \rangle_{yz}$, in Fig. 59. The higher magnitude of scalar gradient implies that the scalar field has more small scales in the flow. As seen in Fig. 59, the scalar field generates more small scales in low diffusivity region than in the high diffusivity region. Thus, we confirm that the scalar gradient depends on diffusivity.

For a qualitative picture of the difference in the scale of the scalar field, we present the scalar gradient iso-surface in Fig. 60. The scalar gradient iso-surface describes how much scale is observed in the domain for a given value of scalar gradient. As seen in the figure, the initial scales of the scalar field are same in all regions. As flow evolves, scalar field in a low diffusivity region generates more scales than in a high

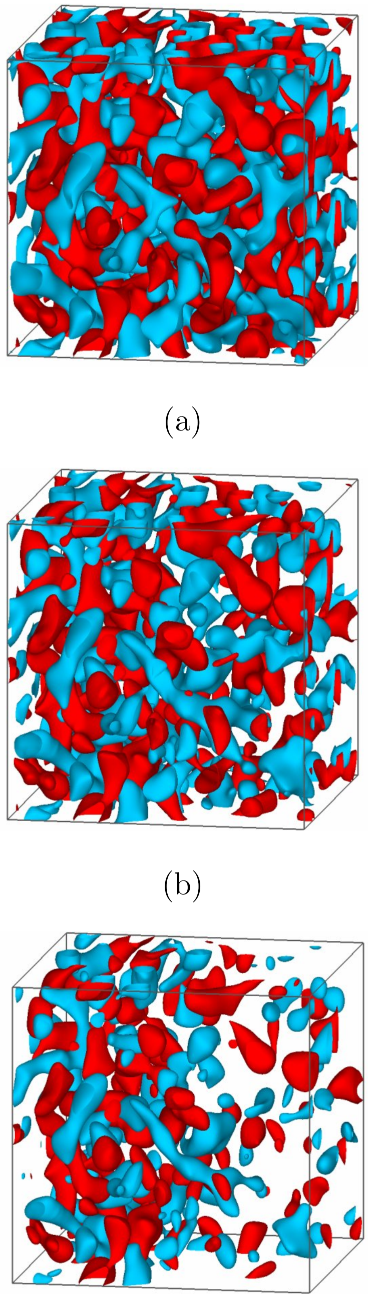

(a)

(b)

(c)

Fig. 60. Iso-surface of $x-$component scalar field gradient, ϕ_x, at (a) $t' = 0.0$; (b) $t' = 0.36$; and (c) $t' = 0.72$. Blue and red describe opposite signs of vorticity with the same magnitude ($\phi_x = -2000$ and 2000).

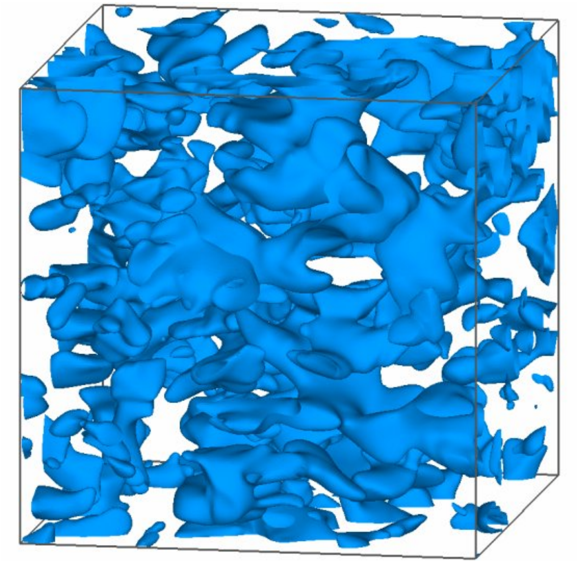

Fig. 61. Iso-surface of the scalar field dissipation rate, $D\phi_i\phi_i$, at $t' = 0.72$ ($D\phi_i\phi_i = 1800$)

diffusivity region, as seen in the second and third figures in Fig. 60. The scalar field dissipation rate is visualized with iso-surface at $t' = 0.72$ in Fig. 61. It should be noted that the total area of a scalar field dissipation iso-surface is uniform along the $x-$coordinate, which means uniform distribution of the scalar field dissipation rate over the domain. From Figs. 59, 60, and 61, we confirm that the small scale scalar field adjusts itself to the magnitude of diffusivity in order to make the dissipation rate of scalar field independent of diffusivity. Thus, the implication of Taylor's conjecture is validated for the scalar field. These results suggest that for variable transport-coefficient flows, the dissipation processes, either for velocity field or for scalar field, have the same characteristics in developing small scales to destroy a given fluctuating energy.

In compressible flow, temperature plays an important role in turbulence energy dissipation. Thus, the temperature fluctuations also need to be considered for accurate turbulence modeling. The effect of thermal conductivity variation on temperature fluctuations is also studied. The temperature fluctuations show similar characteristics to both velocity and scalar fields. The scale of temperature fluctuations adjusts itself to impose the given thermal conductivity and the thermal dissipation tends to be independent of thermal conductivity.

E. Conclusions

Numerical experiments are performed for variable transport-coefficient flows to study the dissipation process. We find that small scale turbulence adjusts itself to imposed viscosity, and the dissipation rate tends to be independent of viscosity. As in the velocity field, the scalar field develops more scales in low diffusivity flows than in high diffusivity flows, making the scalar field dissipation rate independent of imposed diffusivity. Thus, Taylor's (1935) postulate, which states that turbulent dissipation is determined exclusively by large scale flow parameters and is independent of viscosity, is validated even in low Reynolds number flows. This has important consequences for closure modeling of dissipation in high enthalpy flows. This study can also be applied to a non-premixed combustion problem, where the rate of molecular mixing depends on the scalar dissipation rate.

CHAPTER VIII

SUMMARY

Numerical experiments are performed to identify the effect of large temperature fluctuations on compressible turbulence. Boltzmann BGK solvers are employed in the direct numerical simulations. The main focus of the dissertation is to study the nonlinear processes of energy cascading, redistribution, and dissipation in compressible turbulence.

A. Heat release effects

The heat release effects on decaying isotropic and anisotropic compressible turbulence are studied with four investigations. Heat release is represented by initially imposed temperature fluctuations in our study. The main findings are summarized as follows:

1) In the presence of large temperature fluctuations, pressure dilatation transfers energy back and forth between kinetic and thermal modes. However, on an average, pressure dilatation transfers energy from the thermal to the kinetic mode. The temporal velocity gradient is enhanced due to the generation of a rapidly evolving dilatational velocity field in the presence of temperature fluctuations. The alignments among vorticity vector and the gradients of pressure, density and temperature are altered by temperature fluctuations. Especially, the pressure gradient tends to be uncorrelated with the vorticity vector, as well as with the density and temperature gradients in the presence of temperature fluctuations.

2) Isotropic temperature fluctuations introduce isotropic dilatational fluctuations: equal amounts of kinetic energy are added into all three components of Reynolds stress. Temperature fluctuations do not change the return-to-isotropy of the anisotropic solenoidal field. The interactions between solenoidal and dilatational fluctuations are

negligible for turbulent Mach number up to 0.6. The energy deposited by pressure dilatation is proportional to the mean square of initial pressure fluctuations: $\int_a^t \langle pd \rangle d\tau \sim \overline{p'(t=a)p'(t=a)}$. There exists a similar scaling between the integral of pressure dilatation and temperature fluctuations as well. Dilatational dissipation removes energy from the dilatational fluctuations. Equipartition between fluctuating internal energy and dilatational kinetic energy is observed in all numerical experiments, and the dilatational kinetic energy is, in turn, found to scale with the mean square of pressure fluctuations: $k_d \sim \overline{p'p'}$.

3) The most probable strain-rate eigenvalue ratio $(3:1:-4)$ persists at all turbulent Mach numbers. However, the probability of other ratios increase with the turbulent Mach number, which indicates the need for detailed study of the distributions. The small-scale flow structure strongly depends on dilatation level. It is found that at extreme dilatation ($d = -1.7$, 1.7), flow field may experience isotropic compression or expansion. At the intermediate dilatation level ($d = -1.0$, 1.0), small-scale turbulence experiences nearly two-dimensional compression or expansion (planar compression waves or expansion waves), which deforms the flow structure significantly. At zero dilatation level, the flow field reveals the same strain-rate eigenvalue distribution as in incompressible flows. The preferential alignment between vorticity and strain-rate eigenvectors weakens in strong dilatation region as vorticity itself starts to vanish. Thus, for accurate modeling of compressible turbulence, one must incorporate the dilatation level as a parameter rather than turbulent Mach number.

4) The effects of variable transport-coefficients on compressible turbulence are studied. It is confirmed that small-scale turbulence and scalar field adjust themselves to the imposed viscosity and diffusivity, and the dissipation rate tends to be independent of viscosity and diffusivity. This study confirms Taylor's conjecture (1935), which states that the inner-scale dissipation process is determined by the outer-scale

variables of a given flow.

B. Implications for turbulence modeling

This work improves our understanding of compressible turbulence at high turbulent Mach numbers and in the presence of thermal fluctuations, and provides valuable guidance for pressure-strain correlation and pressure dilatation modeling in compressible flows.

The Favre-averaged momentum equation (FANS) is given by

$$\frac{\partial \bar{\rho}\tilde{u}_i}{\partial t} + \frac{\partial \bar{\rho}\tilde{u}_i\tilde{u}_j}{\partial x_j} = -\frac{\partial \bar{\rho}\widetilde{u_i''u_j''}}{\partial x_j} - \frac{\partial \bar{p}}{\partial x_i} + \frac{\partial \bar{\tau}_{ij}}{\partial x_j}\,, \tag{8.1}$$

where $\widetilde{u_i''u_j''}$ is the important unclosed term, Favre-averaged Reynolds stress. The transport equation of the Reynolds stress is expressed as

$$\frac{\partial(\bar{\rho}\widetilde{u_i''u_j''})}{\partial t} = T_{ij} + P_{ij} + R_{ij} - \varepsilon_{ij}\,, \tag{8.2}$$

where T_{ij}, P_{ij}, and ε_{ij} are the turbulent transport, production, and dissipation terms respectively. R_{ij} is the pressure-strain correlation tensor given by

$$R_{ij} = \overline{p\left(\frac{\partial u_i''}{\partial x_j} + \frac{\partial u_j''}{\partial x_i}\right)}\,, \tag{8.3}$$

and redistributes the turbulent kinetic energy. The pressure-strain correlation has two parts, rapid (linear) and slow (non-linear):

$$R_{ij} = R_{ij}^r + R_{ij}^s\,, \tag{8.4}$$

where R_{ij}^r describes the rapid pressure response for a given mean shear force. R_{ij}^s is the return-to-isotropy term, and redistributes the turbulent kinetic energy among Reynolds stresses. In compressible flows, the slow pressure-strain correlation R_{ij}^s is a function of anisotropy, Reynolds number, and Mach number: $R^s_{ij} = f(b_{ij}, Re, M_t)$, where b_{ij} is the anisotropy tensor defined as

$$b_{ij} = \frac{\widetilde{u''_i u''_j}}{2k_0} - \frac{1}{3}\delta_{ij}\,, \tag{8.5}$$

Re is the Reynolds number, and M_t is the turbulent Mach number.

The slow pressure-strain correlation R^s_{ij} can be decomposed into solenoidal and dilatational components:

$$R^s_{ij} = R^{ss}_{ij} + R^{sd}_{ij}\,. \tag{8.6}$$

In this study, the interactions between solenoidal and dilatational fluctuations are found to be weak. Thus, for the solenoidal component of slow pressure-strain correlation R^{ss}_{ij}, in the presence of thermal fluctuations, we may use the same pressure-strain correlation model as in incompressible flows: $R^{ss}_{ij} = -2C_R\varepsilon b^{ss}_{ij}$ [4]. For the dilatational component of slow pressure-strain correlation R^{sd}_{ij}, one possible form of the turbulence field anisotropy can be

$$b^{sd}_{ij} = \langle \frac{\partial T}{\partial x_i}\frac{\partial T}{\partial x_j}\rangle - \frac{1}{3}\langle \frac{\partial T}{\partial x_k}\frac{\partial T}{\partial x_k}\rangle\delta_{ij} \tag{8.7}$$

in the presence of heat release. The trace of pressure-strain correlation, $\langle pd\rangle$, is responsible for the energy exchange between thermal and kinetic modes. The time integration of pressure dilatation $\langle pd\rangle$ can be modeled as

$$\int_a^t \langle pd\rangle d\tau = C_{pd}\overline{T'T'}\,, \tag{8.8}$$

where C_{pd} is a constant. Then, the pressure dilatation can be expressed as

$$\langle pd\rangle = \frac{1}{\tau}C_{pd}\overline{T'T'}\,. \tag{8.9}$$

However, the pressure dilatation model should possess wave-like behavior to accommodate the two-way energy exchange between kinetic and internal modes. If only the overall effect is important, $\langle pd \rangle$ can be modeled to yield monotonic evolution toward equipartition:

$$\langle pd \rangle \sim -\left(k_d - \overline{p'^2}\right) . \tag{8.10}$$

The dependence of small-scale structure on the turbulent Mach number is moderate or weak, and the dilatation level is found to be an important parameter to characterize the compressibility effects in turbulence. Thus, the slow pressure-strain correlation can be more accurately described as

$$R^s_{ij} = f(b_{ij}, Re, d)\,, \tag{8.11}$$

where d is the normalized dilatation level.

REFERENCES

[1] Anderson, J. D., *Hypersonic and high temperature gas dynamics*, McGraw-Hill, Inc., New York, New York, 1989.

[2] Lele, S. K., "Compressibility effects on turbulence," *Annual Review of Fluid Mechanics*, Vol. 26, 1994, pp. 211–254.

[3] Tennekes, H. and Lumley, J. L., *A first course in turbulence*, The MIT Press, Cambridge, Massachusetts, 1972.

[4] Pope, S. B., *Turbulent flows*, Cambridge University Press, Cambridge, United Kingdom, 2000.

[5] Batchelor, G. K. and Proudman, I., "The effect of rapid distortion of a fluid in turbulent motion," *Q. J. Mech. Appl. Math.*, Vol. 7, 1954, pp. 121–152.

[6] Savill, A. M., "Recent developments in rapid distortion theory," *Ann. Rev. Fluid Mech.*, Vol. 19, 1987, pp. 531–573.

[7] Yu, H. and Girimaji, S. S., "Extension of compressible ideal-gas RDT to general mean velocity gradients," *Phys. Fluids*, Vol. 19, 2007, pp. 041702.

[8] Lavin, T., *Rapid distortion theory for compressible turbulence*, Master's thesis, Texas A&M University, College Station, Texas, May 2007.

[9] Cantwell, B. J., "Exact solution of a restricted Euler equation for the velocity gradient tensor," *Physics of Fluids*, Vol. A 4, 1992, pp. 782–793.

[10] Girimaji, S. S. and Speziale, C. G., "A modified restricted Euler equation for turbulent flows with mean velocity gradients," *Physics of Fluids*, Vol. 7, 1995, pp. 1438–1446.

[11] Jeong, E. and Girimaji, S. S., "Velocity-gradient dynamics in turbulence: Effect of viscosity and forcing," *Theoret. Comput. Fluid Dynamics*, Vol. 16, 2003, pp. 421–432.

[12] Suman, S. and Girimaji, S. S., "The non-linear dynamics and small scale topology in compressible turbulence," presented at 44th Annual Technical Meeting, Society of Engineering Science, College Station, Texas.

[13] Kraichnan, R. H., "On the statistical mechanics of an adiabatically compressible fluid," *The Journal of the Acoustical Society of America*, Vol. 27, 1955, pp. 438–441.

[14] Livescu, D. and Madnia, C. K., "Small scale structure of homogeneous turbulent shear flow," *Physics of Fluids*, Vol. 16, 2004, pp. 2864–2876.

[15] Kida, S. and Orszag, S. A., "Enstrophy budget in decaying compressible turbulence," *Journal of Scientific Computing*, Vol. 5, 1990, pp. 1–34.

[16] Kida, S. and Orszag, S. A., "Energy and spectral dynamics in forced compressible turbulence," *Journal of Scientific Computing*, Vol. 5, 1990, pp. 85–125.

[17] Kida, S. and Orszag, S. A., "Energy and spectral dynamics in decaying compressible turbulence," *Journal of Scientific Computing*, Vol. 7, 1992, pp. 1–34.

[18] Sarkar, S., Erlebacher, G., Hussaini, M. Y., and Kreiss, H. O., "The analysis and modelling of dilatational terms in compressible turbulence," *Journal of Fluid Mechanics*, Vol. 227, 1991, pp. 473–493.

[19] Erlebacher, G., Hussaini, M. Y., Kreiss, H. O., and Sarkar, S., "The analysis and simulation of compressible turbulence," *Theoretical and Computational Fluid Dynamics*, Vol. 2, 1990, pp. 73–95.

[20] Erlebacher, G. and Sarkar, S., “Statistical analysis of the rate of strain tensor in compressible homogeneous turbulence,” *Physics of Fluids*, Vol. A 5, 1993, pp. 3240–3254.

[21] Crespo, M., Jamme, S., and Chassaing, P., “On the return to isotropy of compressible anisotropic turbulence,” *35th AIAA Fluid Dynamics Conference and Exhibit*, AIAA-2005-5026, AIAA, Toronto, Ontario Canada, June 2005.

[22] Pantano, C. and Sarkar, S., “A study of compressibility effects in the high-speed turbulence shear layer using direct simulation,” *Journal of Fluid Mechanics*, Vol. 451, 2002, pp. 329–371.

[23] Sarkar, S., “The pressure-dilatation correlation in compressible flows,” *Physics of Fluids*, Vol. A 4, 1992, pp. 2674–2682.

[24] Hamba, F., “Effects of pressure fluctuations on turbulence growth in compressible homogeneous shear flow,” *Physics of Fluids*, Vol. 11, 1999, pp. 1623–1635.

[25] Adumitroaie, V., Ristorcelli, J. R., and Taulbee, D. B., “Progress in Favre-Reynolds stress closures for compressible flows,” *Physics of Fluids*, Vol. 11, 1999, pp. 2696–2719.

[26] Park, C. H. and Park, S. O., “A compressible turbulence model for the pressure-strain correlation,” *Journal of Turbulence*, Vol. 6, No. 2, 2005, pp. 1–25.

[27] Marzougui, H., Khlifi, H., and Lili, T., “Extension of the Launder, Reece and Rodi model on compressible homogeneous shear flow,” *The European Physical Journal B*, Vol. 45, 2005, pp. 147–154.

[28] Jaberi, F. A., Livescu, D., and Madnia, C. K., “Characteristics of chemically reacting compressible homogeneous turbulence,” *Physics of Fluids*, Vol. 12, 2000,

pp. 1189–1209.

[29] Livescu, D., Jaberi, F. A., and Madnia, C. K., “The effects of heat release on the energy exchange in reacting turbulent shear flow,” *Journal of Fluid Mechanics*, Vol. 450, 2002, pp. 35–66.

[30] Lee, K., Yu, D., and Girimaji, S. S., “Lattice Boltzmann DNS of decaying compressible isotropic turbulence with temperature fluctuations,” *International Journal of Computational Fluid Dynamics*, Vol. 20, 2006, pp. 401–413.

[31] Andreopoulos, Y., Agui, J. H., and Briassulis, G., “Shock wave - turbulence interactions,” *Annual Review of Fluid Mechanics*, Vol. 32, 2000, pp. 309–345.

[32] Currie, I. G., *Fundamental mechanics of fluids*, McGraw-Hill, Inc., New York, New York, 1974.

[33] Muralidhar, K. and Biswas, G., *Advanced engineering fluid mechanics*, Alpha Science Int’l Ltd., Oxford, United Kingdom, 2005.

[34] Vincenti, W. G. and Kruger, Jr., C. H., *Introduction to physical gas dynamics*, John Wiley & Sons, Inc., New York, New York, 1965.

[35] Harris, S., *An introduction to the theory of the Boltzmann equation*, Dover Publications, Inc., Mineola, New York, 1971.

[36] He, X. and Luo, L.-S., “Theory of the lattice Boltzmann method: From the Boltzmann equation to the lattice Boltzmann equation,” *Physical Review E*, Vol. 56, No. 6, 1997.

[37] Yu, D., *Viscous flow computations with the lattice Boltzmann equation method*, Ph.D. thesis, University of Florida, Gainsville, Florida, August 2002.

[38] Yu, H., *Lattice Boltzmann equation simulations of turbulence, mixing, and combustion*, Ph.D. thesis, Texas A&M University, College Station, Texas, December 2004.

[39] Lallemand, P. and Luo, L.-S., "Theory of the lattice Boltzmann method: acoustic and thermal properties in two and three dimensions," *Physical Review E*, Vol. 68, 2003, pp. 036706.

[40] d'Humieres, D., Ginzburg, I., Krafczyk, M., Lallemand, P., and Luo, L.-S., "Multiple-relaxation-time lattice Boltzmann models in three dimensions," *Phil. Trans. R. Soc. Lond. A*, Vol. 360, 2002, pp. 437–451.

[41] Xu, K., "Gas-Kinetic schemes for unsteady compressible flow simulations," Lecture series 29th Computational Fluid Dynamics, von Karman Institute for Fluid Dynamics, Belgium, February 1988.

[42] Xu, K., "A gas-kinetic BGK scheme for the Navier-Stokes equation and its connection with artificial dissipation and Godunov method," *Journal of Computational Physics*, Vol. 171, 2001, pp. 289.

[43] Kerimo, J. and Girimaji, S. S., "Boltzmann-BGK approach to simulating weakly compressible 3D turbulence: comparison between lattice Boltzmann and gas kinetic methods," *Journal of Turbulence*, Vol. 8, No. 46, 2007, pp. 1–16.

[44] Mathieu, J. and Scott, J., *An Introduction to Turbulent Flow*, Cambridge University Press, Cambridge, United Kingdom, 2000.

[45] Yu, H., Girimaji, S. S., and Luo, L.-S., "DNS and LES of decaying isotropic turbulence with and without frame rotation using lattice Boltzmann method," *Journal of Computational Physics*, Vol. 209, 2005, pp. 599–616.

[46] Yu, H., Girimaji, S. S., and Luo, L.-S., "Lattice Boltzmann simulations of decaying homogeneous isotropic turbulence," *Physical Review E*, Vol. 71, 2005, pp. 016708.

[47] Yu, D. and Girimaji, S. S., "DNS of homogeneous shear turbulence revisited with the lattice Boltzmann method," *Journal of Turbulence*, Vol. 6, No. 6, 2005, pp. 1–17.

[48] Yu, D. and Girimaji, S. S., "Direct numerical simulations of homogeneous turbulence subject to periodic shear," *Journal of Fluid Mechanics*, Vol. 566, 2006, pp. 117–151.

[49] Yu, H. and Girimaji, S. S., "Lattice Boltzmann equation simulation of rectangular jet (AR = 1.5) instability and axis-switching," *Physica A*, Vol. 362, 2006, pp. 151–157.

[50] Filippova, O. and Hänel, D., "A novel lattice BGK approach for low Mach number combustion," *Journal of Computational Physics*, Vol. 128, 2000, pp. 139–160.

[51] Chang, Q. and Alexander, J. I. D., "Application of the lattice Boltzmann method to two-phase Rayleigh-Benard convection with a deformable interface," *Journal of Computational Physics*, Vol. 212, 2006, pp. 473–489.

[52] Lumley, J. L. and Newman, G. R., "The return to isotropy of homogeneous turbulence," *Journal of Fluid Mechanics*, Vol. 82, 1977, pp. 161–178.

[53] Gence, J. N. and Mathieu, J., "The return to isotropy of an homogeneous turbulence having been submitted to two successive plane strains," *Journal of Fluid Mechanics*, Vol. 101, 1980, pp. 555–566.

[54] Choi, K.-S. and Lumley, J. L., "Return to isotropy of homogeneous turbulence revisited," *Turbulence and Chaotic Phenomena in Fluids*, edited by T. Tatsumi, Elsevier Science Publishers B.V., 1984, pp. 267–272.

[55] Le Penven, L., Gence, J. N., and Comte-Bellot, G., "On the approach to isotropy of homogeneous turbulence: Effect of partition of kinetic energy among the velocity component," *Frontiers in Fluid Mechanics*, edited by J. L. Davis, S. H. & Lumley, Springer, 1985, pp. 1–21.

[56] Chung, K. C. and Kim, S. K., "A nonlinear return-to-isotropy model with Reynolds number and anisotropy dependency," *Physics of Fluids*, Vol. 7, 1995, pp. 1425–1437.

[57] Choi, K.-S. and Lumley, J. L., "The return to isotropy of an homogeneous turbulence," *Journal of Fluid Mechanics*, Vol. 436, 2001, pp. 59–84.

[58] Ristorcelli, J. R. and Blaisdell, G. A., "Consistent initial conditions for the DNS of compressible turbulence," *Physics of Fluids*, Vol. 9, 1997, pp. 4–6.

[59] Ashurst, W. T., Kerstein, A. R., Kerr, R. M., and Gibson, C. H., "Alignment of vorticity and scalar gradient with strain rate in simulated Navier-Stokes turbulence," *Physics of Fluids*, Vol. 30, 1987, pp. 2343–2353.

[60] She, Z.-S., Jackson, E., and Orszag, S. A., "Intermittent vortex structures in homogeneous isotropic turbulence," *Nature*, Vol. 344, 1990, pp. 226–228.

[61] Kalelkar, C., "Statistics of pressure fluctuations in decaying isotropic turbulence," *Physical Review E*, Vol. 73, 2006, pp. 046301.

[62] Kosovic, B., Pullin, D. I., and Samtaney, R., "Subgrid-scale modelling for large-eddy simulations of compressible turbulence," *Physics of Fluids*, Vol. 14, 2002,

pp. 1511–1522.

[63] Bikkani, R. and Girimaji, S. S., “Role of pressure in nonlinear velocity gradient dynamics in turbulence,” *Physical Review E*, Vol. 75, 2007, pp. 036307.

[64] Frisch, U., *Turbulence: The legacy of A. N. Kolmogorov*, Cambridge University Press, Cambridge, United Kingdom, 1995.

[65] Davidson, P. A., *Turbulence: An introduction for scientists and engineers*, Cambridge University Press, Cambridge, United Kingdom, 2004.

[66] Taylor, G. I., “Statistical theory of turbulence,” *Proceedings of the Royal Society of London, Series A*, Vol. 151, 1935, pp. 421–444.

[67] Kolmogorov, A. N., “The local structure of turbulence in incompressible viscous fluid for very large Reynolds number,” *Dokl. Akad. Nauk SSSR*, Vol. 30, 1941, pp. 301–305; English translation in Proc. R. Soc. London, Ser. A 434, 9–13 (1991).

[68] Kolmogorov, A. N., “Dissipation of energy in locally isotropic turbulence,” *Dokl. Akad. Nauk SSSR*, Vol. 32, 1941, pp. 19–21; English translation in Proc. R. Soc. London, Ser. A 434, 15–17 (1991).

[69] Sreenivasan, K. R., “On the scaling of the turbulence energy dissipation rate,” *Physics of Fluids*, Vol. 27, 1984, pp. 1048–1051.

[70] Brachet, M., Meiron, D. I., Orszag, S. A., Nickel, B. G., Morf, R. H., and Frisch, U., “Small-scale structure of the Taylor-Green vortex,” *Journal of Fluid Mechanics*, Vol. 130, 1983, pp. 411–452.

VITA

Kurn Chul Lee received his B.S. degree in Naval Architecture from Seoul National University, Korea in 1992 and his M.S. degree in Ocean Engineering from the same institution in 1994. Following that, he was a researcher and senior researcher in the Agency for Defense Development of Korea. His duty was to design propulsors for underwater and surface vehicles. In 2003, he joined Texas A&M University to study turbulence theory and modeling. His research interests include the turbulence processes and modeling, computational fluid dynamics (DNS, LES, PANS, RANS), kinetic Boltzmann method (LBM, GKM) and flow induced noise. He can be reached through Dr. Sharath S. Girimaji in the Aerospace Engineering Department at Texas A&M University, College Station, TX 77843-3141.